TRIBOLOGICAL PROPERTIES AND WEAR MECHANISM OF HARD COATINGS
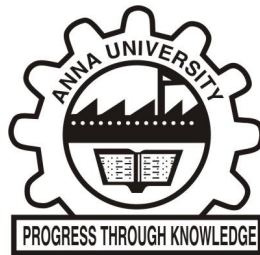
A THESIS

Submitted by

RADHIKA R

in partial fulfilment for the requirement of award of the degree of

DOCTOR OF PHILOSOPHY

FACULTY OF SCIENCE AND HUMANITIES

ANNA UNIVERSITY

CHENNAI 600 025

NOVEMBER 2013

CERTIFICATE

This is to certify that all the corrections / suggestions pointed out by the Indian / Foreign Examiners were carried out in the Thesis titled **"TRIBOLOGICAL PROPERTIES AND WAER MECHANISM OF HARD COATINGS"** submitted by **Ms. R .RADHIKA,** Ph.D Scholar (Reg.No. 2006719156)

Place: Chennai
Date : 2⊘1|3

Dr. D.ARIVUOLI
(SUPERVISOR)
Professor
Crystal Growth Centre
Anna University
Chennai- 600 025

CENTRE FOR RESEARCH

ANNA UNIVERSITY, CHENNAI 600025

PROCEEDINGS OF THE Ph.D VIVA-VOCE EXAMINATION OF Ms. R. RADHIKA HELD AT 04.00 P.M ON 20.11.2013 IN RAMANUJAM COMPUTING CENTRE, ANNA UNIVERSITY, CHENNAI-25

The Ph.D. Viva-Voce Examination of **Ms. R. RADHIKA** (Reg. No. 2006719156) on his Ph.D. Thesis Entitled "**TRIBOLOGICAL PROPERTES AND WEAR MECHANISM OF HARD COATINGS**" was conducted on 20-11-2013 at 04.00 P.M in Ramanujam Computing Centre, Anna University, Chennai-25.

The following Members of the Oral Examination Board were present:

1. **Dr. D. Mangalaraj**   **Indian Examiner**
   Professor and Head,
   Department of Nanoscience and Technology
   Bharathiar University,
   Coimbatore- 641 046

2. **Dr. M. Kamaraj**   **Subject Expert**
   Professor and Head,
   Metallurgical and Materials Engineering
   Indian Institute of Technology, Madras
   Chennai – 600 036

3. **Dr. D. Arivuoli**   **Supervisor &Convener**
   Professor
   Crystal Growth Centre
   Anna University, Chennai – 600025

The research scholar **Ms. R. Radhika** presented the salient features of his Ph.D. work. This was followed by questions from the board members. The questions raised by the Foreign and Indian Examiners were also put to the scholar. The scholar answered the questions to the full satisfaction of the board members.

The corrections suggested by the Indian/Foreign examiner have been carried out and incorporated in the Thesis before the Oral examination.

Based on the scholar's research work, his presentation and also the clarifications and answers by the scholar to the questions, the board recommends that **Ms. R. Radhika** be awarded Ph.D. degree in the Faculty of **Science and Humanities.**

1.   **Dr. D. Mangalaraj**   _(signature)_ 20/11/13   **Indian Examiner**

2.   **Dr. M. Kamaraj**   _(signature)_ 20/11/2013   **Subject Expert**

3.   **Dr. D. Arivuoli**   _(signature)_ 20/11/13   **Supervisor & Convener**

ANNA UNIVERSITY
CHENNAI 600 025

BONA FIDE CERTIFICATE

Certified that this Thesis titled **"TRIBOLOGICAL PROPERTIES AND WEAR MECHANISM OF HARD COATINGS"** is the bona fide work of **Ms. RADHIKA, R**. who carried out the research under my supervision. Certified further, that to the best of my knowledge the work reported herein does not form part of any other thesis or dissertation on the basis of which a degree or award was conferred on an earlier occasion on this or any other scholar.

Place : Chennai

Date :

Dr. D. ARIVUOLI

SUPERVISOR

Professor

Crystal Growth Centre

Anna University

Chennai – 600 025

ABSTRACT

In the modern technology, tribologically suitable components and devices are important to increase the energy efficiency. It is possible when one can reduce the friction coefficient and wear of sliding components. The economic effectiveness can be achieved by better tribological system and therefore research in tribology is aimed at minimizing the energy losses resulting from friction and wear. In this view, hard coatings deposited by physical vapor deposition (PVD) are adequate solutions for increasing the work efficiency, lifetime of tools and components.

The present thesis deals with hard tribological materials γ-TiAl and coatings such as TiAlN, CrN/NbN superlattice, diamond like carbon (DLC) and nanocrystalline diamond nanowire (DNW) films. Various characterization techniques were used to study morphology, microstructure and chemical state of the materials. The thesis describes tribological properties of above mentioned hard coatings sliding against 100Cr6 steel, Al_2O_3 and SiC balls. It also describes friction and wear based on classified mechanisms and outlines material properties that influence the performance of sliding surfaces. Traditionally wear is associated with friction and wear mechanisms are classified as adhesion, abrasion, erosion, fatigue and oxidational.

Mechanical and tribological properties of γ-TiAl alloy, TiAlN, CrN, carbon based coatings of DLC and nanocrystalline DNW were reviewed. The importance of such hard coatings and critical application in machine and industries are highlighted. Moreover, tribological properties and evaluation of wear mechanism is introduced in the respect of microstructure and chemical behavior of the sliding interfaces. Various wear mechanism with different combination of sliding surfaces such as hard coating/soft ball and soft ball/hard coating is reviewed in order to understand the wear mechanism. The fundamentals of some of the characterization techniques used to study the mechanical, tribological, morphological, structural, and chemical properties of the coating and wear track is introduced.

Instrumented micro-indentation technique have been used to characterize the mechanical properties namely hardness and elastic modulus of γ-TiAl alloy. The recorded indentation curves and the related energetic properties were analysed in order to compare the Attaf energetic approach and Oliver-Pharr method. Moreover, tribological behavior of γ-TiAl alloy was studied by sliding against 100Cr6 steel, SiC and Al_2O_3 balls as counterbodies for friction pairs. The friction coefficient and wear rate was found to high when γ-TiAl alloy slides against Al_2O_3 and SiC balls. However, these values were less while sliding against steel ball. The wear mechanism is explained by the sliding combination of harder/harder system such as SiC/γ-TiAl, and Al_2O_3/γ-TiAl alloy. However, steel/γ-TiAl alloy acts as softer/harder sliding combination.

Tribological behavior of TiAlN coating were studied by sliding against 100Cr6 steel, SiC and Al_2O_3 as counterbodies for friction pairs. Two distinct types of wear modes such as oxidational and plastic deformation are investigated. It is shown that wear of metal debris tribochemically reacted with moisture available in ambient atmosphere and metal oxide formation which leads oxidational wear in TiAlN/steel sliding pair. In TiAlN/SiC sliding pair, low friction coefficient is measured and this is attributed to the formation of lubricious composite tribofilm. In contrast, TiAlN/Al_2O_3 pair shows high friction coefficient and wear mechanism is governed by plastic deformation.

CrN/NbN superlattice coating sliding against 100Cr6 steel, SiC and Al_2O_3 ball as counterbodies for friction pairs was investigated. The value of friction coefficient and wear rate was lowest ~0.01 and 2.6×10^{-7} mm^3/Nm, respectively, when coating slides against Al_2O_3 ball. In contrast, friction coefficient and wear rate is increased while sliding with steel and SiC balls. It is observed that the deviation in friction coefficient is described by mechanical and chemical properties of these balls. In this respect, hardness of Al_2O_3 and SiC ball is comparable but significant deviation in friction coefficient is observed. This is related to oxidation resistance of balls which is high for Al_2O_3 compared to SiC as evident by Raman analysis of the wear track. However, steel ball shows oxidational wear mechanism against CrN/NbN superlattice coating.

The tribological properties of DLC and nanocrystalline DNW films were investigated. A friction mechanism based on surface chemistry and

mechanical properties of sliding interfaces such as DLC/100Cr6 steel, DLC/SiC and DLC/Al$_2$O$_3$ is studied. In DLC film, the high friction coefficient is governed by surface roughness of the sliding interfaces during initial sliding passes. However, for longer sliding cycles, the sliding interfaces get smoothened and magnitude of friction coefficient is reduced. Under these experimental conditions, carbonaceous transferlayer forms on the ball sliding surface.

Nanocrystalline DNW films was deposited in N$_2$ enriched microwave plasma enhanced chemical vapor deposition (MPECVD) system. As-deposited DNW film was treated in O$_2$ plasma which resulted in chemical and microstructural modification. The sheath of the nanocrystalline DNW is chemically constituted by amorphous carbon (a-C) and graphite (sp^{2}C-C) like bondings. However, nanowires transformed into ultra- small spherical grains after the O$_2$ plasma treatments. In this condition, a-C and sp^{2}C-C fraction get significantly reduced due to plasma etching. Oxidation and formation of functional groups increases on the surface and inside the wear track. The friction coefficient of O$_2$ plasma treated film showed super low value of ~0.002 with exceeding high wear resistance of 2×10^{-12}mm^3/Nm. Such an advance tribological properties is explained by passivation of covalent carbon bonding and transformation of sliding surfaces by van der Waals and hydrogen bondings. High surface energy and the consequent superhydrophilic behavior of film attributed to the formation of an adsorbate layer of above mentioned functional groups which acts as a lubricant.

ACKNOWLEDGEMENT

TABLE OF CONTENTS

LIST OF TABLES

LIST OF FIGURES

FIGURE NO. **TITLE** **PAGE NO.**

FIGURE NO.	TITLE	PAGE NO.

FIGURE NO.   **TITLE**   **PAGE NO.**

LIST OF SYMBOLS AND ABBREVIATIONS

Symbols

Å	-	Angstrom
Θ_B	-	Bragg angle
°	-	Degree
Δ	-	Superlattice period
d	-	Distance
E	-	Energy
E_0	-	Incident wave
P	-	Load
µm	-	Micrometer
nm	-	Nanometer
n		Order of the wavelength
F	-	Normal force
%	-	Percentage
h	-	Planck's constant
S	-	Sliding distance
δ	-	Spectrometer work function
E_h	-	Specular diffracted wave
c	-	Speed of light
sccm	-	Standard cubic centimeters per minute
λ	-	Wavelength
μ	-	Friction Coefficient
k	-	Wear rate
r	-	Radius of ball
V	-	Wear volume
Φ_0, Φ_h	-	X-ray angle

Abbreviations

a-C	-	Amorphous Carbon
a-C:H	-	Hydrogenated Amorphous Carbon
AEBM	-	Arcam Electron Beam Melting
AEM	-	Analytical electron microscope
AES	-	Auger Electron Spectroscopy
AFM	-	Atomic Force Microscopy
CA	-	Contact Angle
CMA	-	Cylindrical Mirror Analyzer
CVD	-	Chemical Vapor Deposition
DC	-	Direct Current
DLC	-	Diamond Like Carbon
DNW	-	Diamond Nanowires
ECM	-	Expanding Cavity Model
EDS	-	Energy Dispersive Spectroscopy
FCC	-	Face Centered Cubic
FESEM	-	Field Emission Scanning Electron Microscope
FTIR	-	Fourier Transform Infrared Spectroscopy
FWHM	-	Full Width of the Half Maximum
GID	-	Grazing-Incidence Diffraction
GIXRD	-	Grazing-Incidence X-ray Diffraction
HIP	-	Hot Isostatic Pressing
HRXRD	-	High Resolution X-ray Diffraction
IC	-	Indentation Curve
IIT	-	Instrumented Indentation Tester
ISE	-	Indentation Size Effect
LA XRD	-	Low Angle XRD
LVDT	-	Linear Variable Differential Transformer
MCD	-	Microcrystalline Diamond

MEMS	-	Micro-Electro-Mechanical System
MPECVD	-	Microwave Plasma Enhanced Chemical Vapor Deposition
NCD	-	Nanocrystalline Diamond
OEM	-	Optical Emission Monitor
PVD	-	Physical Vapour Deposition
RMS		Root Mean Square
RF	-	Radio Frequency
SEM	-	Scanning Electron Microscope
SPM	-	Scanning Probe Microscopy
ta-C		Tetrahedral Amorphous Carbon
ta-C:H		Tetrahedral Hydrogenated Amorphous Carbon
TEM	-	Transmission Electron Microscope
UNCD	-	Ultrananocrystalline Diamond
XPS	-	X-ray Photoelectron Spectroscopy
XRD	-	X-ray Diffraction

CHAPTER 1

INTRODUCTION

1.1 CLASSIFICATION OF HARD COATINGS

Hard materials for coatings can be divided in three groups depending on the chemical bonding character. All the compounds stand out for their high hardness and high melting points. The modulus of elasticity is lowest for the ionic hard materials. The linear thermal expansion coefficient increases in general from covalent to metallic and hard materials. Comparing these and other coatings relevant properties of the hard materials group one can make the following statements:

(1)   Each of the different groups of hard materials show advantages and disadvantages in respect of an application as hard coatings.

(2)   The metallic hard coatings seem to be the most suitable and versatile layer substances.

(3)   Ionic (ceramic) hard coatings are suitable, in particular for the surface because of high stability and low interaction tendency.

(4)   Optimum wear resistance can only be achieved by multiphase or multilayer coatings.

1.1.1 Metal Nanocomposite Coatings

Longer service life, ability to tolerate higher loads, low cost of maintenance, environmental friendly, improved kinematics, low energy consumption, resistance to corrosion, low friction and high wear resistance are technologically important reasons to coat the machine parts. Several industrial devices like gears, bearings and cutting tools can be coated with hard TiAl, TiAlN, CrN, DLC and crystalline diamond coatings to gain the energy efficiency. In this regard, tribological properties of several hard composite and ceramic coatings are well investigated for the application of machine tools. However, there are several problems related to tribological mechanism which is not properly understood.

The wear mechanisms at macro scale are understood and this scale cannot fully describe the wear mechanism in micro and nano scales. Differences in scale proportions enhance some forces at smaller scales that play a minor role at macro scale tribological performance. Many small scale technical devices like Micro Electro-Mechanical System (MEMS) are hindered because of high adhesive force rather than high friction force. Contact surface may stick to each other due to high adhesion and the device stops to function properly. Such a problem of high adhesion force might be solved using thin coating having low surface potential.

In this respect, TiAl based intermetallics have shown importance and possess a remarkable combination of light-weight, high strength-to-density ratio, high strength at elevated temperature and good corrosion and oxidation resistance (Mattox 2003, Burakowski and Wierzchon 1999, Carvalho 2001, Kessler et al 1998). As a potential new structural material used as aerospace and automotive parts for turbine blades, divergent flap, turbocharger/nozzles, and exhaust valves. These applications are related to friction and wear of the components. However, several investigations show that titanium aluminides have poor wear resistance which would limit their

applications (Barei et al 2006, Holmberg and Matthews 1994, Bushan 2001). Tribological properties of γ-TiAl alloy under high temperature and liquid paraffin lubrication are studied (Matossian et al 1997, Mitterer et al 2006). In order to enhance the wear resistance of TiAl based intermetallics, surface treatment technologies such as plasma carburization (Rastkar and Shokri 2008), laser treatment (Das et al 2004), gas nitridation (Das et al 1999), microarc oxidation (Tetsui and Ono 1999), and thermal oxidation (Rastkar et al 2000) have been performed.

However, there are few studies reported on the dry sliding tribological properties on the TiAl based composites sliding against metallic and ceramic balls. Although, it is known that the incorporation of ceramic leads to a good effect on enhancing the wear resistance and mechanical properties of intermetallics and alloys (Li et al 2006, Miyoshi et al 2003, Cheng et al 2012 a, Cheng et al 2012 b). The disadvantages of TiN include easy oxidation at higher temperatures which decrease the wear resistance (Liu et al 2007, Liu and Wang 2006). To solve this problem, TiAlN coatings is suitable candidate by adding aluminum atoms to TiN structures by keeping the same fcc crystallographic structure (Sopunna et al 2006). It must be considered that the hardness of TiAlN coatings depends on the Ti/Al ratio. It has been revealed that the hardness increases with increasing Al atoms until a certain point. It relies on smaller ionic radius of Al which substitutes Ti atoms in TiN by keeping the NaCl structure. It has been shown that by depositing multilayers, toughness and crack resistance can be considerably increased (Li et al 2008). Crack propagation restricts the adhesive, abrasive and fatigue failure of the coatings (Rastkar and Bell 2005).

Materials such as TiN and TiAlN has high wear resistance against metallic and cermic balls but it shows high friction coefficient. This factor limits to the application of these materials where low friction coefficient is

required for the purpose of energy efficiency. To solve this problem CrN/NbN superlattice structured coatings is deposited (Zhang et al 2011, Niu et al 2012, La et al 2000). The properties of this coating depend on the period of the individual layers in the structure. The layer thickness is less enough such that the coatings form a superlattice structure. In some cases, coating shows the specific characteristics which vary strongly with superlattice periods, e.g. TiN/NbN (Manohara et al 2012), TiN/AlN (Zhou et al 2004) and Ti/TiN (Donohue et al 1997). It is shown that hardness reaches maximum with narrow range of multilayer periods. Superlattice coatings of CrN/NbN deposited by a combined cathodic arc /unbalanced magnetron sputtering process have been proposed as corrosion and wear resistance coatings. These superlattice coatings functions well at limited tribological condition. At extreme tribological conditions these coatings deform significantly and fail.

1.1.2   Carbon Based Advanced Coatings

Carbon is one of the most abundant elements in our planet. It is the sixth most common element and exists in 94% of all known substances. The vast field of organic chemistry is mainly based on carbon. Undoubtedly, it is one of the most important building blocks for many chemicals, drugs and nutritional products on which our well-being and modern life style depend. Carbon is also the essential ingredient of numerous key engineering materials possessing exceptional properties. While some of these are very soft (graphite, polymers, plastics, etc), others are extremely hard and resilient (such as natural and synthetic diamonds and various carbides). Most of the recently discovered nanomaterials (fullerenes, nanotubes, nano-onions, nanofibres, etc) are also carbon based, and they are currently being used in the fabrication of a myriad of nano-to-micro-scale devices. Carbon is also used in the synthesis of numerous hard coatings including diamond, DLC, carbon nitride, transition metal carbides and boron carbide. DLC can be categorized

into different forms based on the content of hydrogen as shown in the ternary phase in Figure 1.1. Films having a high sp^3 content are called tetrahedral ta-C:H or ta-C depending on whether they contain hydrogen or not. Similarly, amorphous films are shown either as a-C:H or a-C.
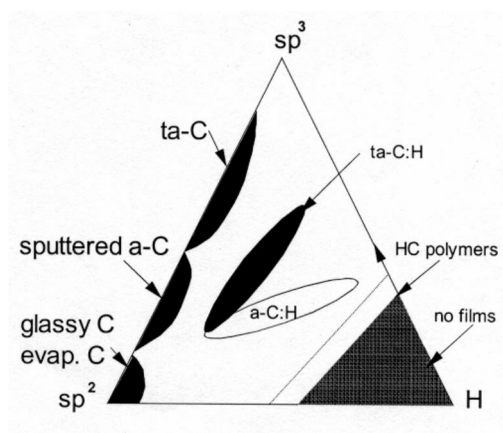
Figure 1.1 Ternary phase diagram showing the various forms of DLC

Because of their superhardness, superhigh thermal conductivity and superlow friction, some of these coatings have tremendous interest in recent years from both the industrial and scientific purposes. Therefore, friction and wear properties have in particular, subject of numerous scientific studies (Quesada et al 2006, Erdemir and Donnet 2000, Erdemir 2002, Erdemir et al 1987, Grill 1997, Kato et al 2003, Fusaro and Sliney 1970, Rabinowicz and Imai 1964, Savage 1948, Burton and Burton 1989). Among the many properties of an engineering material, hardness and stiffness may play the most important role in its ability to carry the load and hence it's wear resistant. In general, materials with high hardness and stiffness have high wear resistance. Diamond represents a prime example with its highest known hardness and extreme wear resistance. However, there is no universal correlation between hardness and friction coefficients of different materials and/or coatings (Erdemir and Donnet 2006a, Erdemir et al 2005).

In particular, DLC films appear to provide the broadest range of hardness and friction values, while some of the recently developed nanocomposite coatings are able to provide superhardness but lack of lubricity (Erdemir and Donnet 2006b). In brief, the field of carbon-based materials and coatings is growing interest from all kinds of scientific and commercial disciplines. In particular, diamond and DLC coatings have attracted the most attention in recent years, mainly because wide range of exceptional properties for demanding applications. In this respect, in this section, we attempt to highlight some of the most important developments in the field of DLC films in general and specifically in their tribology.
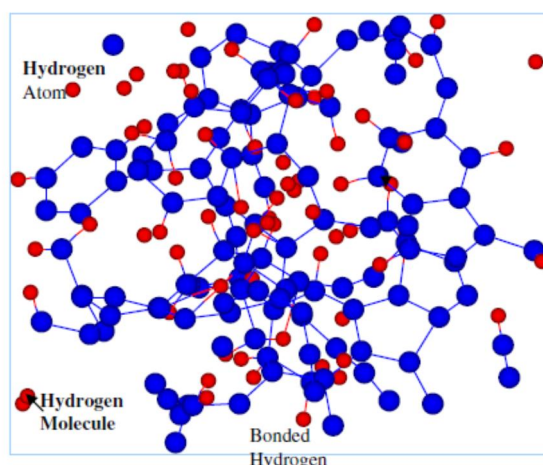
Figure 1.2   **Chemical structure of diamond like carbon (Erdemir et al 2006a)**

The present state of the art in scientific research and industrial practices that involve DLC films is also surveyed. The topic of DLC and tribological properties is vast field. Hence, we will focus our attention mainly on the most important developments. We will also summarize the recent research on their friction and wear mechanisms. In the gas discharge plasmas of the PVD and Chemical Vapour Deposition (CVD) processes, hydrocarbon gas such as methane or acetylene is used as the precursor for carbon. Films derived from such hydrocarbon gases contain not only carbon but also considerable amount of hydrogen in their microstructures, and they are often

referred to as hydrogenated DLC films (Erdemir and Donnet 2006 b). It is schematically shown in Figure 1.2.

Using the same deposition processes, one can also deposit super-hydrogenated DLC films by establishing higher than normal hydrogen-to-carbon ratios. For example, introduction of more hydrogen gas into discharge plasmas during film growth can lead to the formation of highly hydrogenated DLC films that contain more than 40 at.% hydrogen (Erdemir and Donnet 2006b). Compared with hydrogen-free DLCs, these films are relatively soft but exhibit some of the lowest friction and wear coefficients. This topic will be discussed later.

Figure 1.2 shows a molecular dynamic simulation of the atomic structure of a typical hydrogenated DLC film having a network of carbon atoms with three and four-fold atomic co-ordination and different forms of hydrogen within their structure. Similarly, diamonds that are synthesized by means of chemical vapor deposition has many unique and outstanding properties that make it an ideal material for a broad range of scientific and technological applications (Sumant et al 2007). A number of methods for chemical vapor deposition of diamond based on varied gas mixtures and energy sources for dissociating the gas mixture have been reported (Popov et al 2006). These techniques include the use of high-temperature electrons in various kinds of plasmas, high-temperature surfaces of hot filaments, and high-temperature gases in combustion flames to dissociate molecular hydrogen, oxygen, halogen, hydrocarbon, and many other gases containing carbon. The substrate is usually maintained at a temperature much lower than that of electrons in plasma.

Atomic hydrogen is believed to be crucial in the diamond CVD process because of its effectiveness of stabilizing the growing surface of

diamond at the CVD temperature and pressure that is thermodynamically in favor of the growth of graphite instead of diamond. In chemical vapor deposition process, involves the use of hydrogen gas or hydrogen containing molecules. The most typical diamond CVD process uses methane gas diluted by 94-99.9% hydrogen. The super equilibrium of atomic hydrogen can be achieved in a gas mixture with varied percentage of molecular hydrogen. It depends on the balance between the effectiveness of the dissociation process in generating atomic hydrogen and the loss processes for atomic hydrogen to recombine or react with other radicals. By the use of high-power-density microwave plasma, atomic hydrogen is very effectively generated from molecular hydrogen and diamond can be deposited in a mixture of methane diluted by less than 50% hydrogen (Askari et al 2008). Growth of diamond from oxy-acetylene flame uses acetylene and oxygen with the ratio of acetylene to oxygen slightly greater than 1 without molecular hydrogen. Diamond is deposited in the reducing "inner flame" where atomic hydrogen is produced by the high temperature flame as one of the burn products. In addition to atomic hydrogen, there is plenty of OH radicals present near the diamond growing surface inside the flame.

1.2   DEPOSITION OF HARD COATINGS

PVD is widely used technique to deposit hard coatings to enhance surface properties with high wear resistance, low friction and oxidation resistance. The deposition of the thin film takes place in a vacuum chamber. Normally the substrate is cleaned and dried with N_2 gas before entering the vacuum chamber. After the substrate is inserted into chamber, vacuum is increased (10^{-2}–10^{-3} Torr) and the surface is de-gased by a high current density plasma by sputtering at elevated temperature (150-500°C) (Mattox 2003). During the process, a material is evaporated and deposited and forms a thin film on a substrate material. The temperature during deposition of PVD is

low when compared with other methods like CVD. One advantage of deposition at lower temperatures is that unwanted softening and geometrical changes of the substrate do not occur and subsequent heat treatment steps are not needed (Burakowski and Wierzchon 1999, Carvalho 2001). Even though there exist several PVD methods which can be divided into two major parts (Kessler et al 1998), evaporation PVD and sputtering PVD.

The sputtering mechanism involves glowing discharge and momentum transfer process to produce a thin film on a substrate. High-energy particles cause atom or cluster of atoms to be knocked free from the surface of a target, which contain the coating material. The coated film on the substrate contains condensed atoms from ejected target material and particles that have reacted with gas which is contained by PVD vaccum chamber. The process starts with a glowing discharge that forms a flux of ions pointed to the target material and the ions start to sputter atoms from the target in dependence on surface. Via momentum transfer, the atoms are transferred and condensed on the substrate. As the process continues, a thin film is formed. Sputtering PVD can be subdivided to diode, magnetron, ion beam and triode sputtering. In PVD by evaporation, the target coating material is placed in a crucible that is heated to sublimation point in high vacuum environment. There are four main methods for evaporation: induction heating, resistance heating, arc and electron beam gun. By heating the crucible, the coating material is vaporized and condensed on the substrate forming a thin film.

1.2.1 Properties of Hard Coatings

Properties of thin coatings can be arranged into tree different sets:

- ✓ Structural and micro structural properties (thickness, crystal structure, chemical composition, micro structure and texture, surface topography, roughness).

✓ Physical and chemical properties (density, electrical properties, magnetic properties, thermal properties, optical properties, corrosion and oxidation resistance).

✓ Mechanical properties (hardness, adhesion, mechanical stresses, fracture strength, wear, friction).

However, from tribological point of view, properties of hard coatings are thickness, Young's modulus, microstructure, roughness, corrosion resistance, hardness, adhesion, fracture strength and internal stresses. Hardness is the resistance of a material to permanent penetration by another harder material. It cannot be stressed enough that, for tribological applications, the substrate hardness is of prime importance. If the thin fragile coating is not sufficiently supported, it will fail at relatively low contact stresses because it cannot follow deformation of the substrate. Hardness measurements are often used by coating to assess coating quality, and to predict coating performance in various tribological applications. However, the importance of a high, intrinsic coating hardness should not be exaggerated. Chemical stability, fatigue resistance, or other properties, usually have higher influence on the wear resistance than the hardness. The term adhesion refers to the interaction between the closely contiguous surfaces of adjacent bodies, i.e., a film and substrate. Adhesion is defined as the condition in which two surfaces are held together by valence forces or by mechanical anchoring or by both together. Young's modulus, also known as the modulus of elasticity, is difficult to determine due to the low thickness of the coatings. On the other hand, its value has a strong influence on the contact stress field, coating delamination and detachment, coating fracture, residual stress state within the coating, etc. Usually, thin hard coatings have a Young's modulus higher than the substrate, and also often a lower coefficient of thermal expansion. As a

result, an increase of the surface temperature may thus cause the introduction of tensile stresses in the coating.

PVD coatings are widely used in machine parts and tools. Requirements of the coated parts are pushed forward as the development of new hard coatings continues. Mainly the requirements of coating material properties are following (Barei et al 2006):

- low heat transfer coefficient

- low friction coefficient

- high wear resistance

- high hardness

- high toughness

- fine-grain, crystalline microstructure

- chemical inertness

- smooth surface morphology

- good adhesion to substrate

Bulk materials cannot fulfill all these above mentioned requirements. Therefore, PVD coatings have gained popularity in application, mainly in tools and machine's sliding components. The properties of PVD coatings can often be explained by their prominent microstructure during growth. During deposition the coating gets high density of non-equilibrium built-in structural defects during the bombardment of particles against the substrate in the growth process. Since the sputtering process takes place with reactive gas like Ar^+ or N^+ the particles consists of back-scattered inert gas neutrals or ions accelerated towards the substrate via negative substrate bias

potential (Holmberg and Matthews 1994). In the arc evaporation the particles consists of metal ions of multiple ionization states. The defects created during deposition, act as obstacles for dislocation movement. This is one of the important strengthening mechanism of PVD coatings. Other mechanisms are second phase particles, solutes, internal boundaries (column, grain and phase boundaries), high density of point and line defects etc (Bushan 2001). Typical microstructure for PVD coatings are the columnar structure. This columnar structure is formed during deposition, when a flow of atoms reaching the substrate with a limited range of directions.

1.3   CHARACTERIZATION TECHNIQUES

1.3.1   Principle of Microscopic Studies of Thin Films

A finely focused electron beam scanned across the surface of the sample generates secondary electrons, backscattered electrons, and characteristic X-rays. These signals are collected by detectors to form images of the sample displayed on a cathode ray tube screen. Features seen in the Scanning Electron Microscope (SEM) image may then be analyzed for elemental composition using Energy Dispersive Spectroscopy (EDS) (Goldstein et al 2003). EDS identifies the elemental composition of materials imaged in a SEM for all elements with an atomic number greater than boron. Most elements are detected at concentrations on the order of 0.1%. As the electron beam of the SEM is scanned across the sample surface, it generates X-ray fluorescence from the atoms in its path. The energy of each X-ray photon is characteristic of the element. The EDS microanalysis system collects the X-rays, sorts and plots them by energy, and automatically identifies and labels the elements responsible for the peaks in this energy distribution.

The EDS data are typically compared with either known or computer-generated standards to produce a full quantitative analysis showing the sample composition. X-ray intensities are measured by counting photons and the precision obtainable is limited by statistical error. For major elements it is usually not difficult to obtain a precision (defined as 2σ) of better than $\pm$ 1% (relative), but the overall analytical accuracy is commonly nearer $\pm$ 2%, owing to other factors such as uncertainties in the compositions of the standards and errors in the various corrections which need to be applied to the raw data. As well as producing characteristic X-ray lines, the bombarding electrons also give rise to a continuous X-ray spectrum, which limits the detachability of small peaks, owing to the presence of 'background'. Using routine procedures, detection limits are typically about 1000 ppm (by weight). This can be reduced by using long counting times. Spatial resolution is governed by the penetration and spreading of the electron beam in the specimen. Since the electrons penetrate an approximately constant mass, spatial resolution is a function of density. In the case of diamond (density about 3.5 g/cm^3), the nominal resolution is about 2 μm under typical conditions, but for quantitative analysis a minimum grain size of several micrometers is desirable.

Better spatial resolution is obtainable with ultra-thin (~100 nm) specimens, in which the beam does not spread out much. Such specimens can be analyzed in a transmission electron microscope (TEM) with an X-ray spectrometer known as an analytical electron microscope (AEM). Energy resolution is defined as the Full Width at Half Maximum height (FWHM). Conventionally, this is specified for the Mn $K\alpha$ peak at 5.89 keV. For Si (Li) and SDD detectors, values of 130–150 eV are typical (Ge detectors can achieve 115 eV). The resolution of an EDS is about an order of magnitude lower than that of a WDS. It is good enough to separate the K lines of neighbouring elements. The ED spectrometer is especially useful for

qualitative analysis because a complete spectrum can be obtained quickly. Aids to identification are provided, such as facilities for superimposing the positions of the lines of a given element for comparison with the recorded spectrum.

Secondary electron imaging shows the topography of surface features a few nm across. Films as thin as 20 nm produce adequate-contrast images. Materials are viewed at useful magnifications up to 100,000X without the need for extensive sample preparation and without damaging the sample (Brady and Boardman 1995). Even higher magnifications and resolution are routinely obtained by field emission scanning electron microscope (FESEM). A field-emission cathode in the electron gun of a scanning electron microscope provides narrower probing beams at low as well as high electron energy, resulting in both improved spatial resolution and minimized sample charging and damage.

1.3.2   X-ray Diffraction Studies of Thin Films

X-rays are electromagnetic radiation with typical photon energies in the range of 100 eV–100 keV. For diffraction applications, only short wavelength X-rays (hard X-rays) in the range of a few angstroms to 0.1 angstrom (1 keV–120 keV) are used. Because the wavelength of X-rays is comparable to the size of atoms, they are ideally suited for probing the structural arrangement of atoms and molecules in a wide range of materials. The energetic X-rays can penetrate deep into the materials and provide information about the bulk structure (Giacovazzo 1992). X-rays are produced generally by either X-ray tubes or synchrotron radiation. In a X-ray tube, which is the primary X-ray source used in laboratory X-ray instruments, X-ray are generated when a focused electron beam accelerated across a high voltage field bombards a stationary or rotating solid target. As electrons

collide with atoms in the target and slow down, a continuous spectrum of X-ray are emitted, which are termed Bremsstrahlung radiation (Giacovazzo 1992, Mittemeijer and Scardi 2004).

The high energy electrons also eject inner shell electrons in atoms through the ionization process. When a free electron fills the shell, a X-ray photon with energy characteristic of the target material is emitted. Common targets used in X-ray tubes include Cu and Mo, which emits 8 keV and 14 keV X-ray with corresponding wavelengths of 1.54 Å and 0.8 Å, respectively. The energy E of X-ray photon and its wavelength are related by the equation $E = hc/\lambda$, where h is Planck's constant and c the speed of light. X-ray Diffraction (XRD) is a versatile, non-destructive technique that reveals detailed information about the chemical composition and crystallographic structure of natural and synthesized materials. A crystal lattice is a regular three-dimensional distribution (cubic, rhombic, etc.) of atoms in space. These are arranged so that they form a series of parallel planes separated from one another by a distance d, which varies according to the nature of the material (Golovin et al 1984). For any crystal, planes exist in a number of different orientations - each with its own specific d-spacing.

When a monochromatic X-ray beam with wavelength λ is projected onto a crystalline material at an angle θ, diffraction occurs only when the distance traveled by the rays reflected from successive planes differs by a complete number n of wavelengths. By varying the angle θ, the Bragg's Law conditions are satisfied by different d- spacing's in polycrystalline materials. Plotting the angular positions and intensities of the resultant diffracted peaks of radiation produces a pattern, which is characteristic of the sample. Where a mixture of different phases is present, the resultant diffractogram is formed by addition of the individual patterns. Based on the principle of X-ray diffraction, a wealth of structural, physical and chemical information about

the material investigated can be obtained. A host of application techniques for various material classes is available, each revealing its own specific details of the sample studied.

Grazing-Incidence X-ray Diffraction (GIXRD) is a scattering geometry combining the Bragg condition with the conditions for X-ray total external reflection from crystal surfaces. This provides superior characteristics of Grazing-Incidence Diffraction (GID) as compared to the other diffraction schemes in the studies of thin surface layers, since the penetration depth of X-rays inside the slab is reduced by three orders of magnitude typically from 1–10 µm to 1–10 nm as shown in Figure 1.4. X-ray setup for usual X-ray reflectivity is shown in Figure 1.5(a). The wave E_0 incident on the surface at a small angle Φ_0 produces specularly reflected wave E_s. Now, let us rotate the sample round its surface normal, thus preserving the small angle Φ_0. At this rotation, the wave E_0 can make the Bragg angle Θ_B with some atomic planes perpendicular to the surface and originate the diffracted wave. This diffracted wave will be directed at a small angle inwards the sample, because there is no momentum transfer pushing it outwards. It means that the reciprocal lattice vector is parallel to the surface.

However, in spite of the generation inside crystal, it occurs that the diffracted wave can experience the same specular reflection effect as for the incidence wave (Bernhard et al 1987). This gives rise to specular diffracted wave E_h that takes off the crystal at a small angle Φ_h. The value of Φ_h can differ from Φ_0. One can also consider that the wave E_h is generated by the Bragg diffraction of specularly reflected wave E_s. Both the presentations are simplified because in reality the processes of Bragg diffraction and specular reflection interact with each other and cannot be separated out. The most important fact is that E_h principally contains information on the structure of thin surface layer.
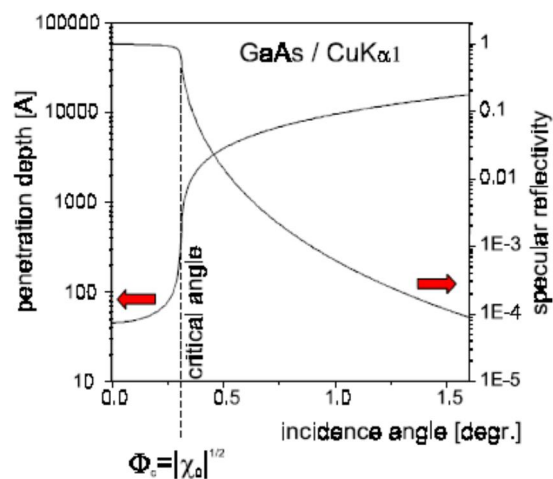
Figure 1.3 Penetration depth and reflectivity of x- ray at grazing angles

GID can also be viewed as a specific case of symmetric Laue diffraction as shown schematically in Figure 1.5(b). When sample set in the conditions for Laue diffraction is rotated by 90º round the reciprocal lattice vector, the Bragg angle is preserved and it end up with GID. This approach is often helpful for understanding some effects in GID. For example, like in usual Laue diffraction, in GID there are Borrmann and anti- Borrmann wavefields with weaker and stronger interaction with crystal, respectively. Let us discuss the angles where GID is characterized by the maximum sensitivity to thin layers.
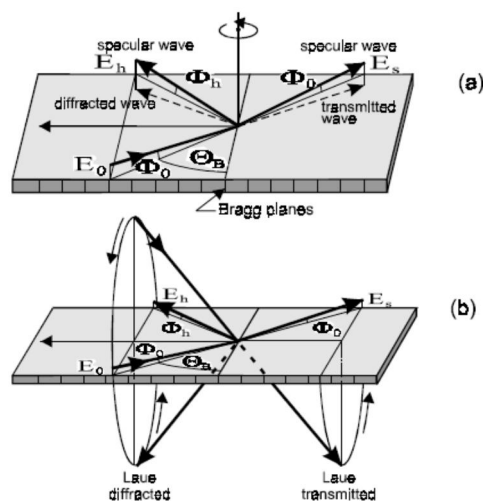
Figure 1.4 Geometry of grazing- incidence x- ray diffraction

The intuitive estimate is that either Φ_0 or Φ_h should be less than the critical angle $\Phi_c = |\chi_0|^{1/2}$ for total external reflection (Figure 1.5). Then, either the illuminated depth should be as small as a few nanometers, or the diffracted intensity would yield from this small depth. Such an estimate is correct for kinematic GID from highly disordered crystals. For dynamical GID the total reflection conditions differ for the Borrmann and anti-Borrmann fields.

1.3.3   X-ray Photoelectron Spectroscopy

The principle of X-ray Photoelectron Spectroscopy (XPS) is based on the photoelectric effect outlined by Einstein in 1905 where the concept of the photon was used to describe the ejection of electrons from a surface when photons impinge upon it. This process can be expressed by Equation (1.1).

$$BE = h\tilde{v}\,K\tilde{E}\delta \tag{1.1}$$

where BE is the binding energy of the electron in the atom (a function of the type of atom and its environment), *hv* is the photon energy of X-ray source, *KE* is the kinetic energy of the emitted electron that is measured in the XPS spectrometer and *δ* is the spectrometer work function. For XPS, Al *Kα* (1486.6eV) or Mg K*α* (1253.6eV) is often the photon energies of choice. Other X-ray lines can also be chosen such as Ti K*α* (2040eV).

The XPS technique is highly surface specific due to the short range of the photoelectrons that are excited from the solid. The energy of the photoelectrons leaving the sample is determined using an analyzer and this gives a spectrum with a series of photoelectron peaks. The binding energy of the peaks is characteristic of each element. The peak areas can be used (with appropriate sensitivity factors) to determine the composition of the materials

surface. The shape of each peak and the binding energy can be slightly altered by the chemical state of the emitting atom. Hence XPS can provide chemical bonding information as well. XPS is not sensitive to hydrogen or helium, but can detect all other elements. Normally, in the outmost 10 nm of thin films surface XPS can identify all elements (present at concentration >0.1 atomic %) except H and He. The analysis of composition has been widely applied in the thin film research fields. The information of all elements in thin film can be gained from the survey scan spectrum of XPS. The detailed information of each element in the thin film can be obtained from the narrow scan spectrum of XPS.

1.3.4   Auger Electron Spectroscopy

Auger Electron Spectroscopy (AES) provides information about the chemical composition of the outermost material comprising a solid surface or interface. The principal advantages of AES over other surface analysis methods are excellent spatial resolution (<1 µm), surface sensitivity (~20 Å), and detection of light elements. Detection limits for most elements range from about 0.01 to 0.1 at%. AES uses a primary electron beam to excite the sample surface. When an inner-shell electron is ejected from a sample atom by the interaction with a primary electron, an electron from an outer shell fills the vacancy. To compensate for the energy change from this transition, an Auger electron or an X-ray is emitted. For light elements, the probability is greatest for the emission of an Auger electron, which accounts for the light-element sensitivity for this technique. The energy of the emitted Auger electron is characteristic of the element from which it was emitted. Detection and energy analysis of the emitted Auger electrons produces a spectrum of Auger electron energy versus the relative abundance of electrons. Peaks in the spectrum identify the elemental composition of the sample surface.

In some cases, the chemical state of the surface atoms can also be determined from energy shifts and peak shapes. Auger electrons have relatively low kinetic energy, which limits their escape depth. Any Auger electrons emitted from an interaction below the surface will lose energy through additional scattering reactions along its path to the surface. Auger electrons emitted at a depth greater than about 2-3 nm will not have sufficient energy to escape the surface and reach the detector. Thus, the analysis volume for AES extends only to a depth of about 2 nm. Analysis depth is not affected by the energy of the primary electron energy. The AES instrumentation can include a tungsten filament or field emission electron gun for the primary electron beam. The instruments are equipped for secondary electron imaging (SEM) to facilitate location of selected analysis areas, and micrographs of the sample surface can be obtained. The sample chamber is maintained at ultrahigh vacuum to minimize interception of the Auger electrons by gas molecules between the sample and the detector. Some instruments include special stages for fracturing samples to examine interfaces that have been freshly exposed within the vacuum chamber. A computer is used for acquisition, analysis, and display of the AES data.

1.3.5   Raman Spectroscopy

Raman spectroscopy provides information about molecular vibrations that can be used for sample identification and quantification. Raman spectroscopy is based on inelastic scattering of monochromatic light, usually from a laser source. Inelastic scattering means that the frequency of photons in monochromatic light changes upon interaction with a sample. Photons of the laser light are absorbed by the sample and then reemitted. Frequency of the reemitted photons is shifted up or down in comparison with original monochromatic frequency, which is called the Raman Effect. This shift provides information about vibrational, rotational and other low frequency transitions in molecules. Raman spectroscopy can be used to study solid, liquid and gaseous samples.

The Raman effect is based on molecular deformations in electric field E determined by molecular polarizability α. The laser beam can be considered as an oscillating electromagnetic wave with electrical vector *E*. Upon interaction with the sample it induces electric dipole moment *P = αE* which deforms molecules. Because of periodical deformation, molecules start vibrating with characteristic frequency v_m. Amplitude of vibration is called a nuclear displacement. In other words, monochromatic laser light with frequency v_0 excites molecules and transforms them into oscillating dipoles. Such oscillating dipoles emit light of three different frequencies when:

- A molecule with no Raman-active modes absorbs a photon with the frequency v_0. The excited molecule returns back to the same basic vibrational state and emits light with the same frequency v_0 as an excitation source. This type of interaction is called an elastic Rayleigh scattering.

- A photon with frequency v_0 is absorbed by Raman-active molecule which at the time of interaction is in the basic vibrational state. Part of the photon's energy is transferred to the Raman-active mode with frequency v_m and the resulting frequency of scattered light is reduced to $v_0 - v_m$. This Raman frequency is called Stokes frequency, or just "Stokes".

- A photon with frequency v_0 is absorbed by a Raman-active molecule, which, at the time of interaction, is already in the excited vibrational state. Excessive energy of excited Raman active mode is released, molecule returns to the basic vibrational state and the resulting frequency of scattered light goes up to $v_0 + v_m$. This Raman frequency is called Anti-Stokes frequency, or just "Anti-Stokes".

1.3.6   Fourier Transform Infrared Spectroscopy

In infrared spectroscopy, IR radiation is passed through a sample. Some of the infrared radiation is absorbed by the sample and some of it is passed through (transmitted). The resulting spectrum represents the molecular absorption and transmission, creating a molecular fingerprint of the sample. Like a fingerprint no two unique molecular structures produce the same infrared spectrum. This makes infrared spectroscopy useful for several types of analysis.

Fourier Transform Infrared Spectroscopy (FTIR) is most useful for identifying chemicals that are either organic or inorganic. It can be utilized to quantities some components of an unknown mixture. It can be applied to the analysis of solids, liquids, and gasses. The term FTIR refers to a fairly recent development in the manner in which the data is collected and converted from an interference pattern to a spectrum. Today's FTIR instruments are computerized which makes them faster and more sensitive than the older dispersive instruments. Because the strength of the absorption is proportional to the concentration, FTIR can be used for some quantitative analyses. Usually these are rather simple types of tests in the concentration range of a few ppm up to the percent level. For example, EPA test methods measure the C-H absorption for either petroleum or total hydrocarbons.

Molecular bonds vibrate at various frequencies depending on the elements and the type of bonds. For any given bond, there are several specific frequencies at which it can vibrate. According to quantum mechanics, these frequencies correspond to the ground state (lowest frequency) and several excited states (higher frequencies). One way to cause the frequency of a molecular vibration to increase is to excite the bond by having it absorb light energy. For any given transition between two states the light energy (determined by the wavelength) must exactly equal the difference in the

energy between the two states [usually ground state (E_0) and the first excited state (E_1)]. The energy corresponding to these transitions between molecular vibrational states is generally 1-10 kilocalories/mole which corresponds to the infrared portion of the electromagnetic spectrum.

1.3.7 Atomic Force Microscopy

The particular instrument is used to study the surface topography as well as measuring three dimensional images of surface of the sample. Atomic Force Microscopy (AFM) is a form of scanning probe microscopy (SPM) where a small probe is scanned across the sample to obtain information about the sample's surface. This is schematically shown in Figure 1.3. The information gathered from the probe's interaction with the surface can be as simple as physical topography or as diverse as measurements of the material's physical, magnetic, or chemical properties. These data are collected as the probe is scanned in a raster pattern across the sample to form a map of the measured property relative to the X-Y position.
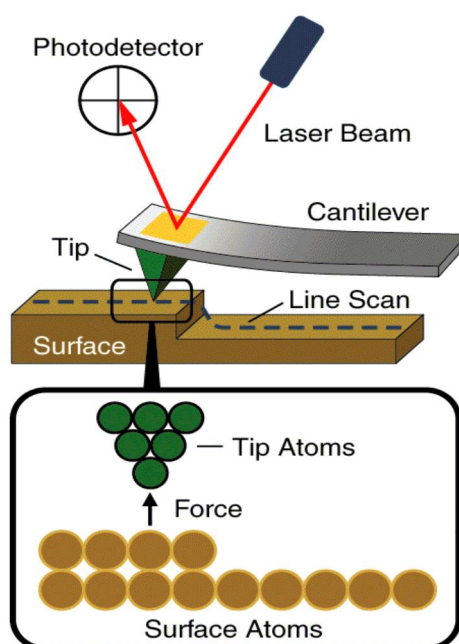
Figure 1.5 Schematic diagram of atomic force microscope

The AFM probe has a very sharp tip, often less than 100 Å diameter, at the end of a small cantilever beam. The probe is attached to a piezoelectric scanner tube, which scans the probe across a selected area of the sample surface. Interatomic forces between the probe tip and the sample surface cause the cantilever to deflect as the sample's surface topography (or other properties) changes. A laser light reflected from the back of the cantilever measures the deflection of the cantilever. This information is fed back to a computer, which generates a map of topography and/or other properties of interest.

1.3.7.1   Operation of AFM

In the so-called contact-AFM mode, the tip makes soft "physical contact" with the surface of the sample. The deflection of the cantilever Dx is proportional to the force acting on the tip, via Hook's law, $F=-kx$, where k is the spring constant of the cantilever. In contact-mode the tip either scans at a constant small height above the surface or under the conditions of a constant force. In the constant height mode the height of the tip is fixed, whereas in the constant-force mode the deflection of the cantilever is fixed and the motion of the scanner in z-direction is recorded. By using contact-mode AFM, even "atomic resolution" images are obtained.

For contact mode AFM imaging, it is necessary to have a cantilever which is soft enough to be deflected by very small forces and has a high enough resonant frequency to not be susceptible to vibrational instabilities. Silicon nitride tips are basically used for contact mode. In the non-contact mode, the probe operates in the attractive force region and the tip-sample interaction is minimized. The use of non-contact mode allowed scanning without influencing the shape of the sample by the tip-sample forces. In most

cases, the cantilever of choice for this mode is the one having high spring constant of 20-100 N/m so that it does not stick to the sample surface at small amplitudes. The tips mainly used for this mode are silicon probes.

In tapping mode-AFM the cantilever is oscillating close to its resonance frequency. An electronic feedback loop ensures that the oscillation amplitude remains constant, such that a constant tip-sample interaction is maintained during scanning. Forces that act between the sample and the tip will not only cause a change in the oscillation amplitude, but also change in the resonant frequency and phase of the cantilever. The amplitude is used for the feedback and the vertical adjustments of the piezoscanner are recorded as a height image. Simultaneously, the phase changes are presented in the phase image (topography).

1.3.8   Contact Profilometer

Profilometer is a measuring instrument used to measure a surface's profile, in order to quantify its roughness. A diamond stylus is moved vertically in contact with a sample and then moved laterally across the sample for a specified distance and specified contact force. A profilometer can measure small surface variations in vertical stylus displacement as a function of position. A typical profilometer can measure small vertical features ranging in height from 10 nm to 1 mm. The height position of the diamond stylus generates an analog signal which is converted into a digital signal stored, analyzed and displayed. The radius of diamond stylus ranges from 20 nanometres to 50 μm, and the horizontal resolution is controlled by the scan speed and data signal sampling rate. The stylus tracking force can range from less than 1 to 50 milligrams.

1.3.8.1   Advantages of contact profilometer

- Acceptance: Most of the world's surface finish standards are written for contact profilometer. To follow the prescribed methodology, this type of profilometer is often required.

- Surface Independence: Contacting the surface is often an advantage in dirty environments where non-contact methods can end up measuring surface contaminants instead of the surface itself. However, because the stylus is in contact with the surface, this method is not sensitive to surface reflectance or color.

- Resolution: The stylus tip radius can be as small as 20 nm, significantly better than white-light optical profiling. Vertical resolution is typically sub-nanometer as well.

- Direct Technique: No modeling required.

1.3.9   Principle of Nanoindentation

Instrumented indentation testing has emerged as an important method for the evaluation of a material's mechanical response to applied load. The technique is based on the continuous recording of applied force and resulting depth of penetration of an indenter throughout the whole loading and unloading cycle, when applied force is controlled. The two mechanical properties measured most frequently using indentation techniques are the hardness, H, and the elastic modulus, E. As the indenter is pressed into the sample, both elastic and plastic deformation occurs, which results in the formation of a hardness impression conforming to the shape of the indenter. During indenter withdrawal, only the elastic portion of the displacement is recovered, which facilitates the use of an elastic solution in modeling the contact process (Pharr 1998, Sneddon 1965).

Figure 1.6 shows a typical load–displacement curve and the deformation pattern of an elastic–plastic sample during and after indentation. In this figure, h_{max} represents the displacement at the peak load, $P_{max} \times h_c$ is the contact depth and is defined as the depth of the indenter in contact with the sample under load h_f is the final displacement after complete unloading. S is the initial unloading contact stiffness. Nanoindentation hardness is defined as the indentation load divided by the projected contact area of the indentation. It is the mean pressure that a material can support under load. From the load–displacement curve, hardness can be obtained at the peak loads as described in Equation (1.2).

$$H = P_{max}/A \tag{1.2}$$

where A is the projected contact area. Measurement of the projected contact area from a load–displacement curve requires the contact depth, h_c.
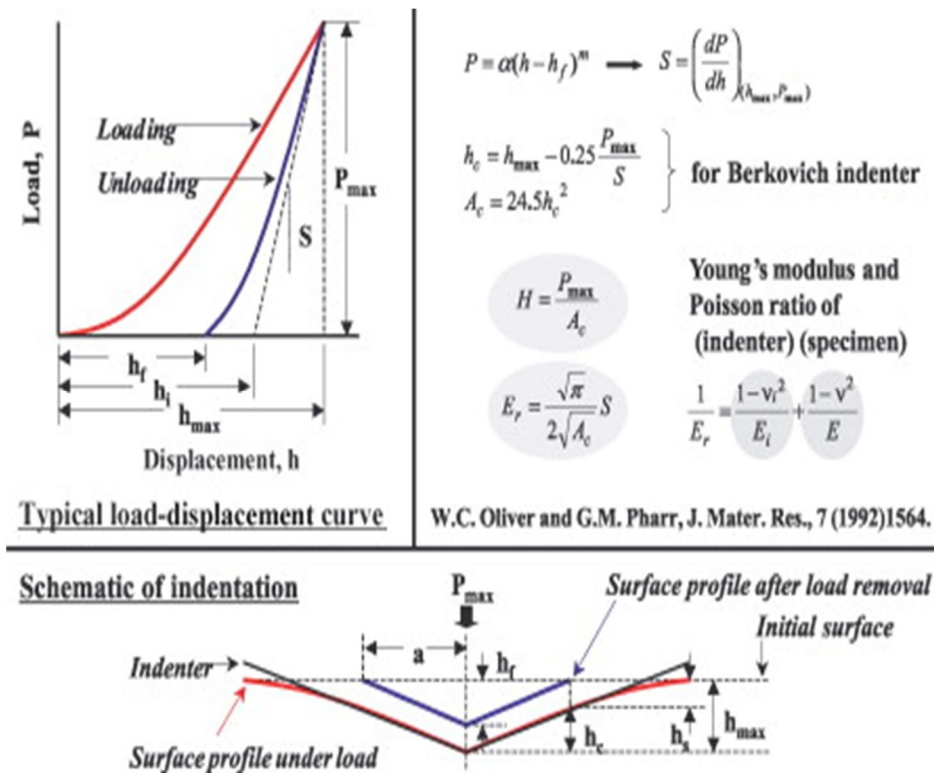
Figure 1.6   **Schematic representation and formulation of anoindentation (Pharr 1998)**

The elastic modulus of the indented sample can be inferred from the initial unloading contact stiffness, $S=dP/dh$, i.e., the slope of the initial portion of the unloading curve. Based on relationships developed by Sneddon (Tabor 1951) for the indentation of an elastic half space by any punch is described as a solid of revolution as a smooth function of A. This is geometry-independent relation involving contact stiffness, contact area, and elastic modulus can be derived by Equation (1.3).

$$S = 2\beta\sqrt{\frac{A}{\pi}}E_r \qquad (1.3)$$

where β is a constant that depends on the geometry of the indenter (β=1.034 for a Berkovich indenter) (Pharr 1998) and E_r is the reduced elastic modulus, which account for the fact that elastic deformation occurs in both the sample and the indenter and it is given in Equation (1.4).

$$E_r = \frac{1-v^2}{E} + \frac{1-v_i^2}{E_i} \qquad (1.4)$$

where E and v are the elastic modulus and Poisson's ratio for the sample, respectively, and E_i and v_i are the same quantities for the indenter. For diamond, E_i =1141 GPa and $v_i = 0.07$ ((Pharr 1998, Tabor 1951). To calculate the elastic modulus E, from Equations (1.3) and (1.4), the contact stiffness and the projected contact area need to be determined from the load–displacement curve. Oliver and Pharr found that the unloading curve is usually not linear as suggested by Doerner and Nix (1986), but it is better described by a power law function as given in Equation (1.5).

$$P = a\left(h - h_f\right)^m \qquad (1.5)$$

where *a* and *m* are empirically determined by fitting parameters. The unloading stiffness, *S* is then established by differentiating Equation (1.5) at the maximum depth of penetration, $h= h_{max}$ expressed in Equation (1.6)

$$S = \frac{dp}{dh}\bigg|_{\text{max}} \quad am\left(h_{\text{max}} - h_f\right)^{m-1}$$

(1.6)

For an indenter with a known geometry, the projected contact area is a function of the contact depth. The area function for a perfect Berkovich indenter is given in Equation (1.7).

$$A_c = 24.56h_c^2$$

(1.7)

Indenters used in practical nanoindentation testing are not ideally sharp. Therefore, tip geometry calibration or area function calibration is needed. The contact depth can be estimated from the load–displacement data using Equation (1.8)

$$h_c = h_{\text{max}} - \varepsilon \frac{P_{\text{max}}}{S}$$

(1.8)

where ε is a constant that depends on the indenter geometry ($\varepsilon= 0.75$ for a Berkovich indenter) (Pharr 1998). The above analysis is based on an elastic solution and works well for hard ceramics and diamond films when sink-in predominates (i.e., the indented material around the indenter is moved below the original surface plane).

1.3.10 Friction and Wear Screening Test Methods

In the tribometer measurement, the load shell is applied by *Fn* sensor. Against the load shell, the friction force is measured by tangential *Ft* sensor. Motor rotates against the ball and substrate is under the sliding

contact. The schematic diagram and real photographic view of CSM standard microtribometer is shown in Figure 1.7.
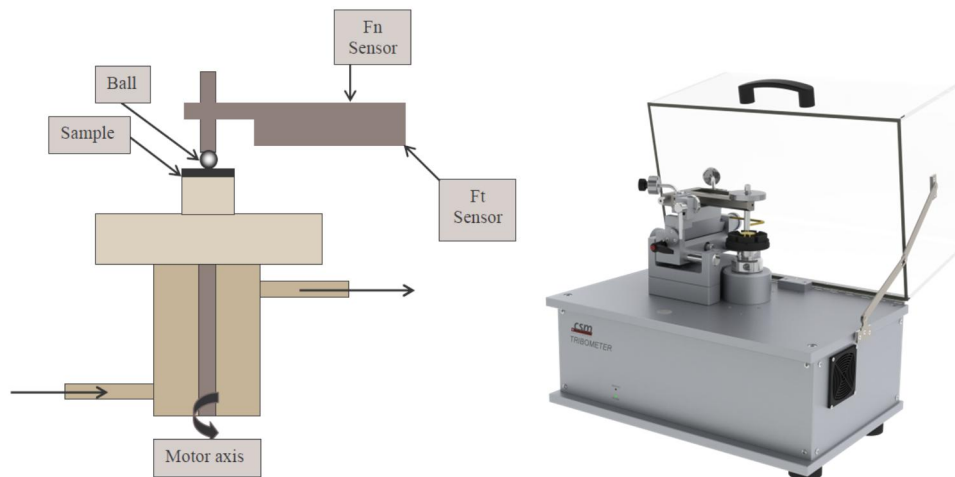
Figure 1.7 Schematic diagram and real view of CSM microtribometer

There are a number of classifications of friction and wear mechanisms. Two basic friction mechanisms are common such as adhesive and mechanical deformation. In the early days wear was typically classified based on its appearance on the surface after the contact. This is schematically shown in Figure 1.8. Examples of such appearance are based on scoring, scuffing, pitting, gouging, spalling, fretting and galling. Some of these classes are more or less related to certain applications, such as gear contacts. The classifications used have recently been based more on the fundamental mechanisms of material removal due to the increased knowledge of the fundamental wear processes. The most widely used classifications are: adhesive, abrasive, fatigue and tribochemical wear (Holmberg and Matthews 1994, Kato et al 2001). The classification of basic friction and wear mechanisms can be developed as suggested in Figure 1.8. Friction is resisting force between the two surfaces in contact or sliding. This is due to following reasons:

1) **Adhesion:** breaking the adhesive bonds between the two surfaces,

2) **Ploughing:** resistance originating from elastic and plastic deformation when a harder counter surface moves through a softer or more elastic surface.

3) **Hysteresis:** resistance originating from continuous elastic deformation within one of the surfaces in motion.
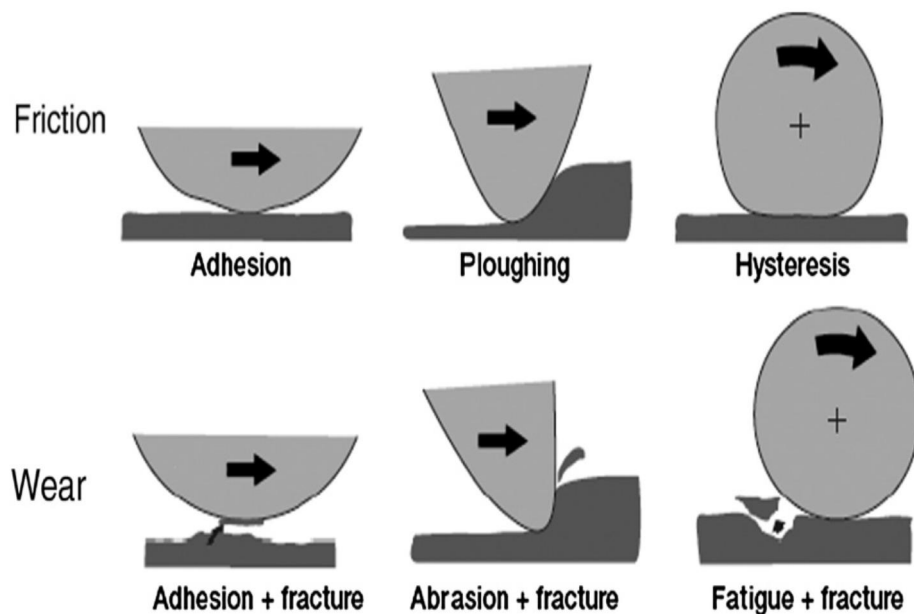
Figure 1.8   The basic friction and wear mechanisms i.e., adhesion, ploughing and hysteresis, (Holmberg et al 1998).

In the basic friction mechanisms no material removal is involved. Debris in the contact zone would make the contact mechanisms more complicated. The wear is process of detachment of material from one surface. It is different from friction in the sense that it is not taking place at a certain moment but during a time period when the surfaces are in moving contact. The detachment of material may be due to:

1) ***adhesion + fracture:*** adhesive lifting or shearing force is causing such a high tension and shear stresses in the surface that exceed the material strength and a crack is formed, resulting in crack growth and material detachment – a wear debris is formed.

2) **abrasion + fracture**: hard counter surface moves through a softer surface and deform by shear stresses. This result in crack formation, crack growth, fracture and material detachment. These process causes to generate wear debris (Holmberg and Matthews 1994, Kato et al 2001).

3) ***fatigue + fracture:*** surface deforms due to the compressive loading that leads to crack nucleation and growth, resulting in material detachment. The crack growth process may take place during a number of loading cycles. Finally wear debris is generated.

The above classification of the basic wear mechanisms are focusing on how the material removal takes place. For this reason tribochemical wear is not included. However, the chemical processes that take place on a surface are certainly important but they are not mechanisms that cause material removal. They are chemical reactions that cause surface material modification, either improvement or degradation, and changes, e.g., the plastic and elastic properties and fracture resistance of the interfaces (Kato et al 2001, Holmberg 1992, Fouvry et al 1994, Oliveira and Bower 1996, Burnett and Rickerby 1987). The changed surface properties will either increase or decrease the strength of the material and its resistance to cracking and material removal. Further, fatigue wear as it is normally considered in multicycling sliding can be divided into two phases. In the first phase the

material modification takes place in the absence of material removal. During continuous loading of the surface the material properties are gradually changed.

The second phase that is known as wear or material removal, appears when new surface does not resist loading and causes to generate crack. Such a crack grows, material is removed and debris is formed. The friction hysteresis mechanism is based on elastic deformation and thus, it is similar to the ploughing. However, the geometry is different (Guu et al 1996, Bhushan and Gupta 1991). Similarly, fatigue and fracture wear mechanism is based on material deformation by compression and shear and it is similar to the abrasion mechanism. Therefore, it considers only two basic friction and wear mechanisms. For friction, it would be adhesive and controlled by elastic/plastic deformation. For wear, it would be adhesive wear exhibited by plastic deformation which is controlled by fracture. However, the surface material modification processes, surface chemistry and fatigue is considered as non wear processes (Holmberg Mathews 1994, Finkin 1969).

It is important to understand the basic mechanisms especially when one can model friction and wear in different contact condition. Normally, the basic mechanisms are combined in a complex way due to more complicated contact geometry, involving roughness and debris, due to inhomogeneous surface with changing properties due to variations in loading and sliding conditions. The main parameters influencing the tribological process are illustrated in Figure 1.9. During the sliding contact some of the parameters changes, surface layers are formed, strain hardening develops, local temperature raises causing softening, etc. After completing one sliding event

new set of parameters control the friction and wear. Therefore, it is often useful to study the tribological phenomena on different size levels.
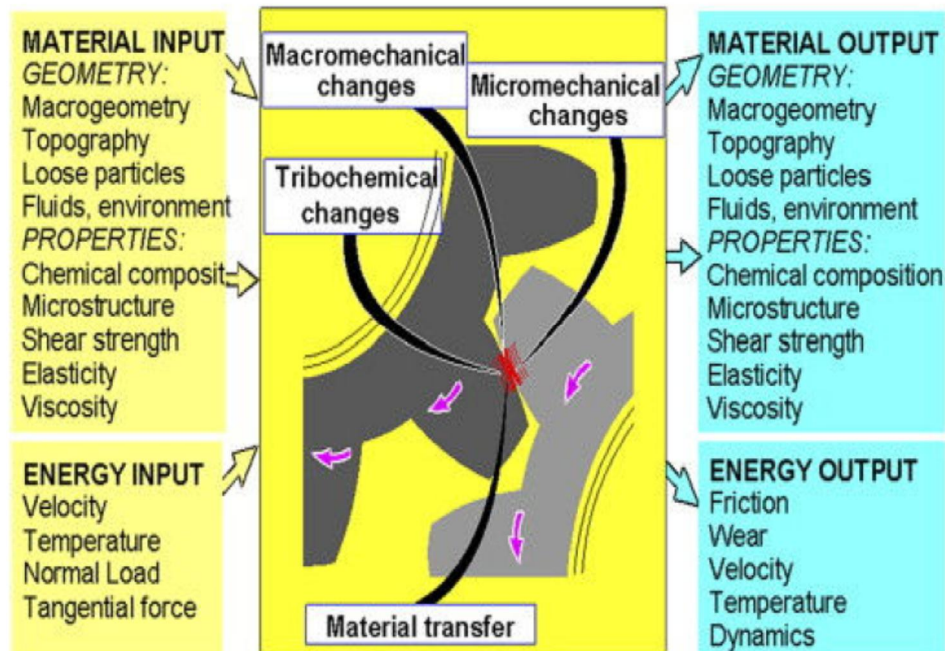
Figure 1.9   The tribological contact process is determined by a number of geometry, material and energy related parameters, (Holmberg et al 1998).

Figure 1.10 shows typical contact conditions that occur on a macro level when a hard sphere is sliding on a flat surface deposited with a thin coating (Singer 1991, Holmberg et al 1998, Holmberg et al 2007). In each contact condition there are typically a limited number of parameters that dominate the friction and wear behavior. If one can identify them and understand their interactions then it is useful to predict friction and wear. Dominating parameters in the contact condition shown in Figure 1.10 are the coating/substrate hardness relationship, coating thickness, surface roughness and debris in the contact.

COATED CONTACT — HARD SLIDER

HARDNESS OF COATING — SOFT / HARD / HARD / SOFT

THICKNESS OF COATING
- a) PLOUGHING
- b) SHEARING
- c) LOAD SUPPORT FROM COATING
- d) SUBSTRATE DEFORMATION

SURFACE ROUGHNESS
- e) SCRATCHING
- f) PENETRATION
- g) REDUCED CONTACT AREA & INTERLOCKING
- h) ASPERITY FATIGUE

DEBRIS
- i) PARTICLE EMBEDDING
- j) PARTICLE ENTRAPPING
- k) PARTICLE HIDING
- l) PARTICLE CRUSHING
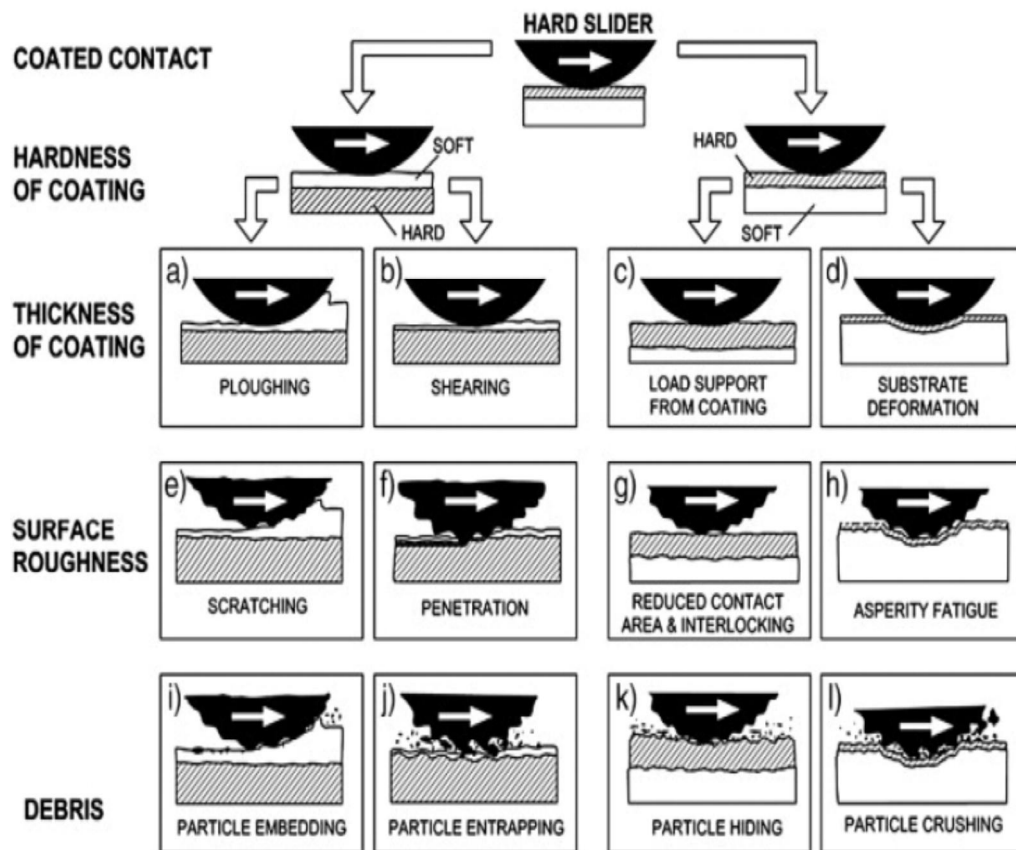
Figure 1.10   Main parameters influencing the friction in a macro-contact with thin coated surfaces are the hardness of the coating and the substrate, the coating thickness, the surface roughness and debris in the contact zone (Holmberg et al 1998).

1.3.10.1   Surfaces in a Sliding Contact

The friction and wear is governed by the shear taking place at the surface and in the deformed sub-surface layer. Consequently, elastic, plastic and fracture behavior both at the surface and in the deformed sub-surface layer appears. A thin coating typically consists of a part of deformed surface layer. In addition, surface degradation may take place due to tribochemical and fatigue processes that influence on the surface strength to loaded conditions. Thus the crucial material parameters are elastic modulus, hardness, shear strength and the fracture toughness on the surface, in the coating, at the coating/ substrate interface and in the substrate under the

coating. This is schematically shown in Figure 1.11. In this figure hardness, *H*, is used as a symbol representing the resistance to plastic deformation. The conditions of a sphere sliding over a flat coated surface, ideally smooth surfaces, homogenous materials and no contamination or wear debris involved. The influence of these parameters in a coated contact has been discussed elsewhere (Doerner and Nix 1986, Finkin 1969, Holmberg et al 2007).

E = elastic modulus
H = hardness or shear strenth
K = fracture toughness
T = shear strength
u = upper surface
c = coating
i = interface coating/substrate
s = substrate
h = coating thickness
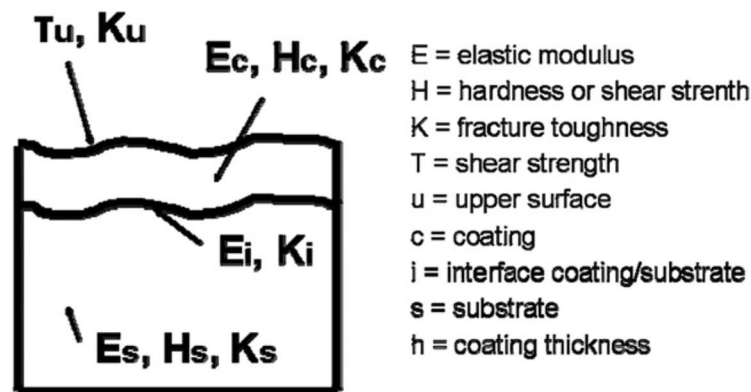
Figure 1.11 Symbols used for material parameters in a coated surface

Adhesive friction is dominated by the shear taking place in the top layer of surface or shear force acting between the two interacting surfaces. Surface chemistry, reactive transfer layers and structural parameters, like hydrogen content in DLC coatings are important to investigate the friction behavior as described in Equation (1.9).

$$\mu_a = f(\tau_u) \tag{1.9}$$

Ploughing friction is dominated by the elastic and plastic behavior of the coating and the substrate. Structural properties, multilayer, gradient, modified and doped structures and structural parameters such as sp^2/sp^3 ratio for DLC coatings are internal factor which influence friction and wear. The capacity of the coating/substrate system to resist deformation is frequently

called load carrying capacity. In this condition, the coefficient of friction can be described by Equation (1.10).

$$\mu_{p=}f\,(E_c, H_c, E_s, H_s, h) \tag{1.10}$$

Hysteresis friction is mainly dominated by the elastic properties of the substrate but also to some extent by the elastic properties of the coating. In this condition, the coefficient of friction is derived by Equation (1.11).

$$\mu_h = f\,(E_{\underline{s}}, E_{\underline{c}}, h) \tag{1.11}$$

Adhesive wear is dominated by the fracture behavior acting on the surface, subsurface, coating/substrate interface and in the substrate. Fracture describes property of the material to resist cracking, intrinsic detachment and breaking. The adhesive force, F_a, from the counter face acts to tear off part of the surface material over the contact area A (Figure 1.12a). When surface roughness is included, the adhesive wear typically decreases. In this condition, the wear rate is described by the Equation (1.12).

$$k = v_{adh}/\,w.s = f\,(K_u, K_c, K_i, K_s) \tag{1.12}$$

where v_{adh} is the volume of adhesive wear, w is the load and s is the sliding distance. The breaking of the material may take place at different locations in the surface depending on the material strength at each location as shown in Figure 1.12b–e. Due to the depth of the debris detachment the result is:

- Top layer fragments K_u (Figure 1.12b),

- Coating fragments K_c (Figure 1.12c),

- Coating delamination K_i (Figure 1.12d) or

- Substrate and coating debris K_s (Figure 1.12e).
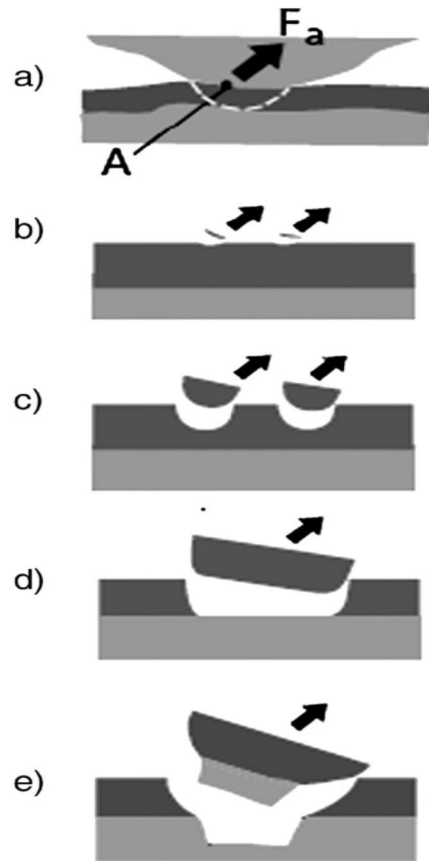
Figure 1.12 **Two surfaces attach to each other by adhesion (a) and the movement of the top surface results in an adhesive force, *Fa*, that tries to detach material over an area, *A*, from one of the surfaces. The detachment may take place (b) at the top surface (c) within the coating, (d) at the coating/substrate interface and (e) in the substrate.**

Abrasive wear is dominated by geometrical collision of the two moving surfaces resulting in high stresses, material shear and fracture results to debris formation. Collisions goverened by the hard asperities, debris ploughing and asperity collision. This is shown in Figure 1.13. In this condition, the wear rate is expressed by Equation (1.13).

$$k = v_{abr} = w.\ s = f\ (K_c,\ K_i,\ K_s,\ H_c,\ H_i,\ H_s,\ h) \tag{1.13}$$

Due to the depth of the debris detachment the result is:

- Coating fragments K_c,

- Coating delamination K_i or

- Substrate and coating debris K_s.
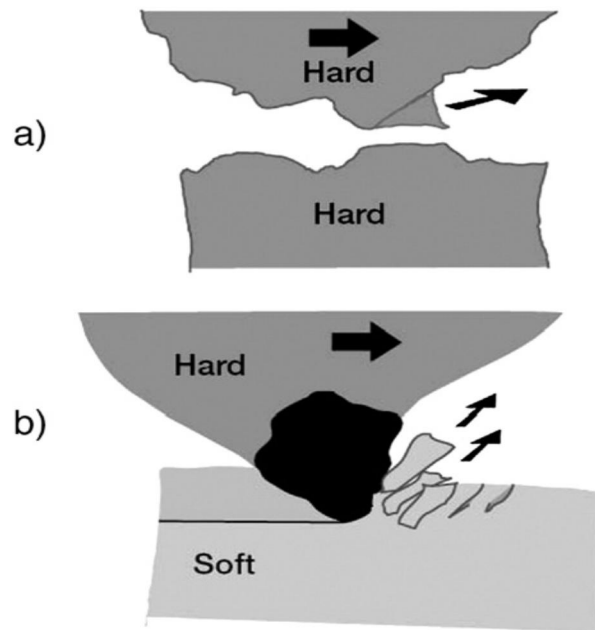
Figure 1.13 Abrasive wear is characterized by a hard asperity (a) or debris (b) that deforms the counter surface in a ductile or brittle way resulting in fracture, cracking and debris generation

1.4   SCOPE OF THE THESIS AND ORGANIZATION

When two surfaces slide against each other, several contact mechanical and chemical changes occur. In this process, energy dissipates in several forms. One of them is friction force which resists the motion during the sliding of two surfaces in contact. Depending on the nature of friction force of sliding bodies, the wear resistance is described. In this thesis, tribological investigation of selected hard coatings such as TiAl, TiAlN, CrN/NbN, DLC and nanocrystalline DNW films is studied. Wear tests were carried out by using pin-on-disc tribo-tester with constant load using three

different balls counterbodies such as 100Cr6 steel, Al_2O_3 and SiC. The loading conditions were based on a model of Hertz contact pressure theory. Wear tests were performed at macro/ engineering level and the wear tracks was investigated by micro Raman spectroscopy, energy dispersive X-ray and scanning electron microscope.

The physical properties of these materials are interesting and there is need to study the tribological properties and wear mechanism for various applications. In this respect, the present thesis develops fundamental understanding and relationship of microstructure and chemical behavior of sliding surfaces with deformation and wear mechanism. The evaluation of friction coefficient and wear resistance of these coatings is studied. The present study reviews the former approach and attempts to understand the wear mechanism in hard coatings. The samples were also subjected to other characterization techniques such as nanoindentation, SEM, XRD, AFM, XPS, AES, Raman spectroscopy, FTIR, contact angle and contact profilometer. The thesis broadly comprises the following:

i)   Mechanical and tribological properties of

γ -Ti-48Al-2Cr-2Nb alloy

ii) Tribological properties and wear mechanism of

TiAlN coating

iii) Tribological properties and wear mechanism of

CrN/NbN superlattice coating

iv) Tribological properties of diamond like carbon and nanocrystalline diamond nanowire films

v)   Summary and suggestions for future work

CHAPTER 2

INDENTATION AND TRIBOLOGICAL STUDIES OF γ -Ti-48Al-2Cr-2Nb SLIDING AGAINST Al₂O₃, SiC AND STEEL BALLS

2.1   INTRODUCTION

Gamma titanium aluminide (γ –TiAl) based alloys containing 45– 48 at.% of Al and in general small amounts of elements such as vanadium, chromium, manganese, and niobium have emerged as potential engineering structural materials for high temperature applications in aerospace as well as in automotive industries (Bonacchi et al 2003, Kestler et al 2003, Moser et al 2008) because of their low density, attractive mechanical and tribological properties, corrosion and creep resistance (Wang et al 1997, Li et al 2008, Varlese et al 2013). Therefore, great attention is paid in the scientific literature to investigate and improve the mechanical and tribological properties of this alloy. In particular, Ti-48Al-2Cr-2Nb has a two-phase structure, consisting of the major γ-TiAl phase and minor α_2Ti$_3$Al phase that can co-exist in a fully lamellar or nearly lamellar microstructure (Yamaguchi et al 1999, Chraponski et al 2003, Biamino et al 2011, Xinhua et al 2009).

Instrumented micro-indentation or depth sensing indentation have been widely used to characterize the mechanical properties namely hardness, elastic modulus from the force-displacement curve data. Different procedures have been proposed to extract these quantities. Oliver- Pharr method (Oliver and Pharr 2004) is commonly used to calculate hardness and elastic modulus

due to simple power law procedure based on linear regression analysis. Also additional, approaches based on the work of indentation (Attaf 2003) are also considered to avoid the overestimation of properties and to minimize the errors arising from uncertainty in the measurement of the characteristic depths of penetration. All the energetic approaches based on the work of indentation were originated from Stillwell and Tabor (1961). Later, Sakai (1993) put forth a relationship between the energy of the hysteresis indentation loop and the hardness. Bull (2006) has used the energy concept to construct a hardness model for bulk materials and graded films and also to predict the erosion nature in bulk materials as well as in coatings. Work of indentation approach in addition with the sink in and pile- up behaviour were studied by various authors (Tuck et al 2001, Beegan et al 2005, Zhou and Yao 2007, Ozun et al 2008, Xiang et al 2011). Feng et al (2011) was used the approach to determine the fracture toughness for a Vickers indentation. Attaf (2003) has also extended the energetic approach measuring all the 15 possible energies from the ICs to reach better understanding of mechanical phenomenon in materials.

In this work, an attempt to improve the effectiveness of the results by comparing the indentation properties of Ti-48Al-2Cr-2Nb by two different methods (the Oliver-Pharr method and the work of indentation approach) has been carried out. Figure 2.1 shows the typical indentation loading-holding-unloading ICs. The Oliver-Pharr data analysis is used for fitting the unloading portion of the ICs to an empirical power-law relationship as given in Equation (2.1).

$$P = a\left(h - h_f\right)^m \tag{2.1}$$

where P = load, h = penetration depth, a and m are fitting parameters, h_f is the final displacement after complete unloading and directly determined by the experimental ICs. Then the contact stiffness S, defined as the derivative at peak load which is evaluated by Equation (2.2).

$$S = \left. \frac{dp}{dh} \right|_{\max} = am\left(h_{\max} - h_f\right)^{m-1} \qquad (2.2)$$

The so called contact depth h_c is also calculated by the Equation (2.3).

$$h_c = h_{\max} - \varepsilon \frac{P_{\max}}{S} \qquad (2.3)$$

where ε is tip-dependent geometry factor which is equal to 0.75 for Vickers indenters (Attaf 2003). The contact area A_c is estimated using an appropriate area function given in Equation (2.4).

$$A_c = F\left(h_c\right) = 24.h_c^2 + C_1 h_c^1 + C_2 h_c^{1/2} + C_3 h_c^{1/4} + ...$$
$$+ C_8 h_c^{1/128} \qquad (2.4)$$

where C_1 through C_8 are constants. The reduced modulus E_r, which combines elastic properties of both the indenter and the sample (Oilver and Pharr 2004), is given in Equation (2.5).

$$E_r = \frac{\sqrt{\pi}}{2} \frac{S}{\sqrt{A_c}} \qquad (2.5)$$

And it is related to elastic properties given in Equation (2.6).

$$\frac{1}{E_r} = \left[\frac{\left(1 - v_s^2\right)}{E_s} \right] + \left[\frac{\left(1 - v_i^2\right)}{E_i} \right] \qquad (2.6)$$

where v and E are poisson's ratio and the elastic modulus with the subscripts s and i indicating sample and indenter respectively. Further, indentation hardness H_{IT} of the specimen can be expressed by Equation (2.7).

$$H_{IT} = \frac{P_{max}}{A_c} \tag{2.7}$$

Oliver and Pharr method (Oilver and Pharr 2004) assumes that the unloading behavior of the material after indentation is purely elastic. If $h_f/h_m > 0.7$ the Oliver-Pharr method overestimates the hardness by as much as 100% because of the effect of pile-up (Cheng and Cheng, 1998, Giannakopolus and Suresh 1999). To avoid such overestimation the Attaf energetic approach (Attaf 2003) at various load conditions is analyzed to evaluate the indentation properties. In this method unified correlations and proportionality constants are derived to define a constant β inherent to the material. The three widely used energetic terms are namely presented in Figure 2.1 (Attaf 2003): (i) the total energy, W_T, located under the loading curve, (ii) the elastic energy W_E, represents the area under the unloading curve, (iii) the plastic energy W_P, which corresponds to the area enclosed by the two curves and is given by the difference between W_T and W_E.
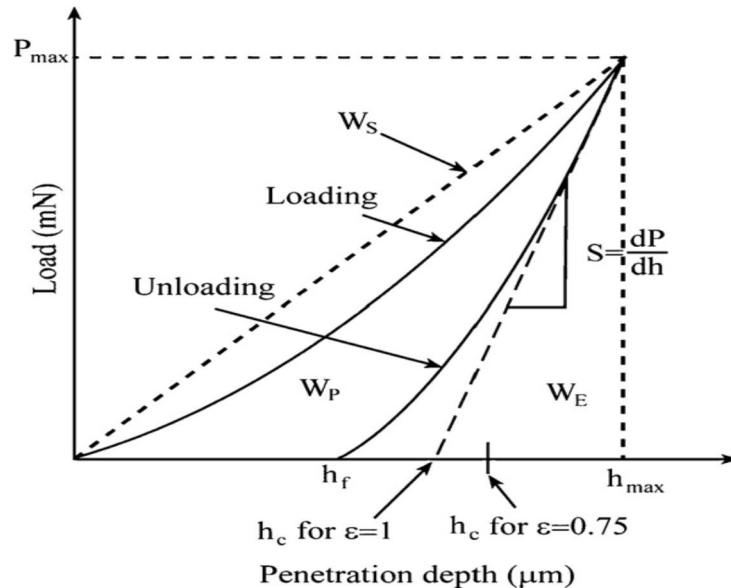
Figure 2.1 Typical indentation cycle showing load-unload curve

In addition, the absolute energy W_S and other eleven auxiliary characteristic energy have been taken into account by Attaf (2003) by considering specific correlations between these energies, such as the proportionality between the total energy and the indentation load or between elastic energy and contact depth of penetration (Attaf 2003, Venkatesh et al 2000, Dao et al 2009, Tabor 1995). The total energy constant v_T is a proportionality constant specific to the total energy W_T compared to the absolute energy W_S. In addition, correlation between total, plastic and elastic energies is defined by three constants (plastic-total (v_{PT}), elastic-total (v_{ET}), elastic-plastic (v_{EP}) are calculated along with the energy constants.

Energy ratios can be used to determine some constants estimating deformation behavior of materials (Sakai 1993, Bull 2006, Khan et al 2009). Ozun et al (2008) considered the ratio of W_P/W_T equivalent to that of h_f/h_{max}. Also, they discussed about another ratio namely W_T/W_E is proportional to relationship between elastic modulus (E/H), which is an important parameter to determine the degree of elastic recovery and fracture toughness of materials. Accurate determination of tensile properties from instrumented indentation tester (IIT) would have significant advantages over the traditional tensile test because, in the micro range, indentation testing measures a small volume of the material thus the tensile properties of surfaces and coatings could be obtained. Moreover the indentation testing is nearly non-destructive and a consistent technique to quantify the mechanical properties. It is well known that the yield strength (σ_y) of a rigid, perfectly plastic material is correlated to the hardness (H) expressed in Equation (2.8) (Tabor 1951):

$$H = C\sigma_y \qquad (2.8)$$

In which C is the constraint factor, independent of the indenter angle and $C \approx 3$ for metals. It is also worth to note that C varies from 1.5 to 3

and is a material property-controlled factor, i.e., *C* is dependent on the extent of plasticity measures by E/σ_y (*E* is the elastic modulus of the material), strain hardening and other strengthening mechanisms, etc (Fischer-cripps 2004). The relationship, however, is not valid for hard or highly elastic materials such as glass and ceramic due to relatively larger elastic deformation. In this condition the indentation is analogous to the expansion of a spherical cavity by a uniformly distributed pressure, so that the analysis by Gao (2006), Expanding Cavity Models (ECM's) has been adopted. The theoretical framework to formulate the following hardness-yield strength relationship for conical/pyramidal indenters reported in (Brooks et al 2008). The expression is is given in Equation (2.9).

$$\frac{H}{\sigma_y} = \frac{2}{3}\left\{1 + \frac{3}{4}\left(\frac{1}{3}\frac{E}{\sigma_y}\cot\alpha\right)^n + \frac{1}{n}\left[\left(\frac{1}{3}\frac{E}{\sigma_y}\cot\alpha\right)^n - 1\right]\right\} \tag{2.9}$$

where α is indenter half-angle (68° for a Vickers diamond indenter)

The Indentation Size Effect (ISE) has been examined extensively for different kind of materials. Literature reviews (Blau and Lawn 1986) showed that, despite much interest, the cause of the ISE has never been satisfactorily determined. The most widely used empirical equation for describing the ISE is the Meyer's law which uses correlation technique between the test load and the resultant indentation size using a simple power law relationship given in Equation (2.10).

$$P_{max} = Ch_c^n \tag{2.10}$$

where *C* and *n* are constants derived directly from the curve fitting of the experimental points. The exponent n, sometimes referred to the Meyer index, is usually considered as a measure of ISE. For the normal ISE behavior, the

exponent $n < 2$. When $n > 2$, there is the reverse ISE behavior. When $n = 2$, no ISE would be observed. Due to the nature of intrinsic brittleness, Vickers indentation may result in micro fracture around the impression in the surface and/or subsurface of ceramics when the load applied is high enough (Lawn and Wilshaw 1981). Relation derived in (Attaf 2003) namely the indentation displacements $h_i = K_{hF}^i F_{max}^{Ehf}$ is the same law considered in its reverse form as it expresses the maximum depth variation versus the maximum load. The exponent E_{hF} corresponds to $1/n$.

2.2   EXPERIMENTAL TECHNIQUES

The titanium aluminide alloy used in this study has a nominal chemical composition of (at %) Ti-48Al-2Nb-2Cr. Rod samples of about 15 mm in diameter and 200 mm in length were sinter-melted by Arcam Electron Beam Melting (AEBM) process. The samples cut from the rods are mechanically grinded with SiC paper and finally polished with 1/4µm diamond paste. Surface roughness was measured using a Taylor Hobson profilometer. The microstructure were analysed by optical and scanning electron microscopy (Jeol JXA 8600) after etching with Kroll's reagent for 15 s. The instrumented indentation tests were carried out using a Fischerscope HM2000 Nanoindenter Tester with a Vickers indenter. ICs were recorded continuously under different maximum loads (300, 500, 1000, 1500 mN). The imposed indentation load-time profile has been always characterized by a loading and unloading rate of 1 and 4 mN/s, respectively and by 10 s of holding time. Indentations measurements were carried out at room environment and the average of the indentation trials are used.

Linear reciprocating mode of ball on the disk micro- tribometer (CSM Instruments, Switzerland) was used to carry out the friction and wear

measurements. In these measurements, the normal load and sliding speed were constant 5 N and 4 cm/s respectively. Three different kinds of balls counterbodies such as 100Cr6 steel, SiC and Al_2O_3 were used for sliding against γ-TiAl alloy. The diameter of the ball was 6 mm. Surface roughnesses of the balls were 0.04, 0.02, and 0.03 µm for 100Cr6 steel, SiC and Al_2O_3, respectively. Tribological experiments were conducted in ambient atmospheric condition at room temperature where the relative humidity was 75%. Insitu wear track depth was measured by Linear Variable Differential Transformer (LVDT) sensor coupled to the micro- tribometer.

2.3 RESULTS AND DISCUSSION

2.3.1 Scanning Electron Microscopy and Energy Dispersive X-ray Analysis

The microstructure and morphology of the alloy was investigated by optical microscope as well as SEM. Final microstructure of Ti-48Al-2Cr-2Nb is a duplex type and consists of equiaxed γ and lamellar colonies of γ and α_2–phases (Seetharaman and Semiatin 2001) as shown in Figure 2.2-2.4 at various magnifications.
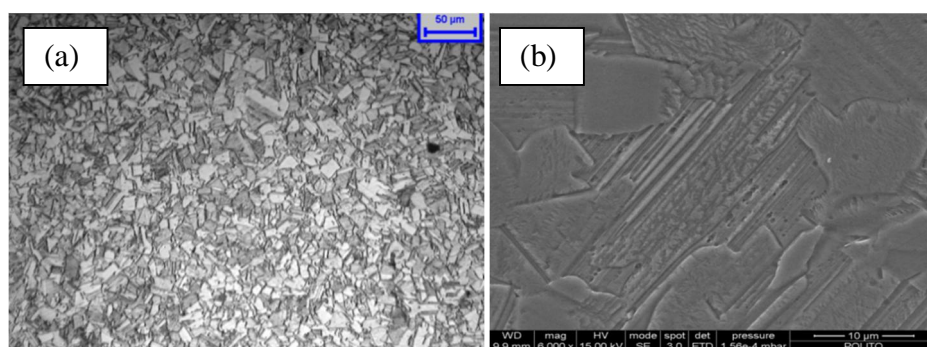
Figure 2.2   Final microstructure of Ti-48Al-2Cr-2Nb alloy after HIP heat treatment: (a) optical (200 X), and (b) SEM (6000 X)
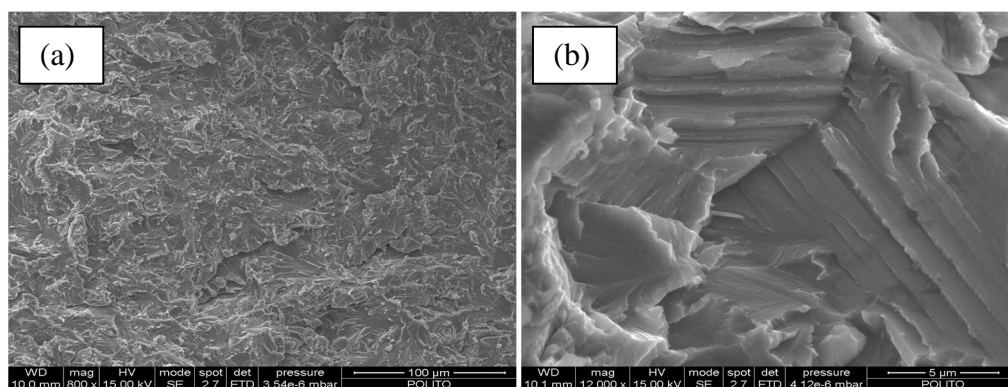
Figure 2.3   SEM fractographs of γ-TiAl based alloy at (a) 800 X and (b) 5000 X

The fractured surface morphology shown in Figure 2.4 are useful in elucidating effects of microstructure on the tensile ductility and fracture properties of γ–TiAl. A combination of interlamellar cracking and intragranular fracture leading to a brittle fracture at various temperatures has been reported by many authors. Soboyejo and Mercer (1994) discussed that the faster fatigue crack growth rates in gamma alloys can be attributed partly to the higher incidence of irreversible deformation-induced crack-tip twinning phenomena. Also the occurrence of the intergranular may therefore, be associated with segregation phenomena during processing or heat treatment (Soboyejo and Mercer 1994, Mercer and Soboyejo 1997).
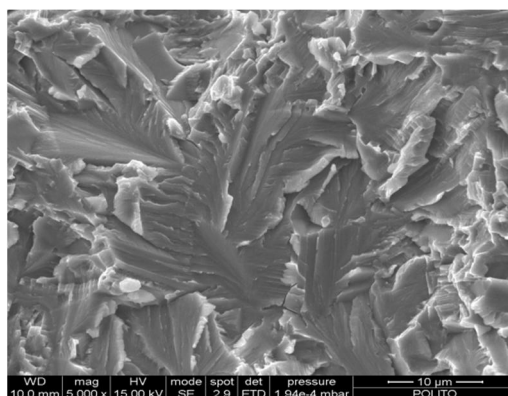
Figure 2.4   SEM fractographs of γ-TiAl based alloy at 5000 X (other place)

Figure 2.5 shows an indentation residual imprint in an etched sample. After the heat treatment (HIP ping), the porosity is minimized but still there exists some small voids that may affect the final over all mechanical properties.
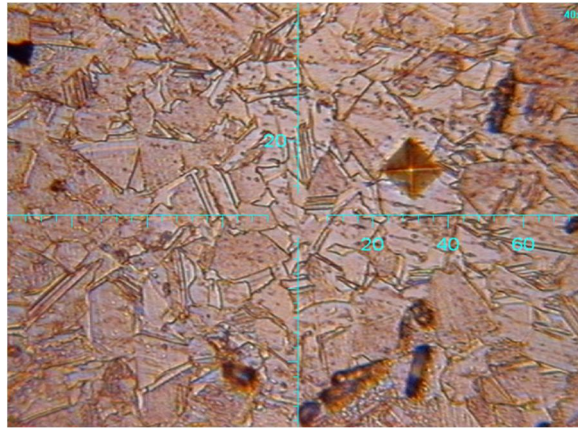
Figure 2.5 Residual imprint in an etched sample.

Note how the size of the residual imprints is the same of the main microstructural features. Hence indentation results are strongly related to the location in which the indentation test is carried out and a considerable spread of results is then expected with a low reproducibility. This may be due to the surface roughness which cause such deviations in the measured hardness value and also depends on the phase being indented. Deyneka et al (2010) carried out the indentation studies on TiAl alloys and concluded that the average hardness of the lamellar colonies is higher than that of the equiaxed grains considering the polishing effects.

The factors affecting the hardness and microstruture with respect to polishing is determined from the deformation and twinning during micro and nano indentation. However, at high strain rates the twinning becomes a self – stopping process that may restrict the plastic flow of the intermetallic (Imayev et al 1997). Lameller interfaces have effective glide obstacles for the twinning and ordinary dislocations. Kempf et al (2002) reported that no significant hardness difference could be deduced for the twinned and untwinned γTiAl

lamellae. In our studies many indentation tests have been performed imposing the same maximum load in order to assess the standard deviation of indentation hardness and modulus 223.9 MPa and 11.98 Gpa, respectively. In particular, considering a value of maximum depth of penetration equal to 0.5 mN, the range between the maximum/minimum values of the maximum depth of penetrations are 0.28 µm. This range is less in the case of lower value of the maximum imposed force (e.g. 0.24 µm).

Chemical composition was observed with respect to the sample after EBM process and HIP treatment. The presence of chemical constituents in the alloy were determined using EDS analysis as shown in Figure 2.6 and the and the related results are reported in Table 2.1. The content of oxygen and the other interstitial elements (C, N, and H) that can negatively affect the mechanical properties of the alloys is not reported due to the low EDS resolution in the case of low atomic weight elements.
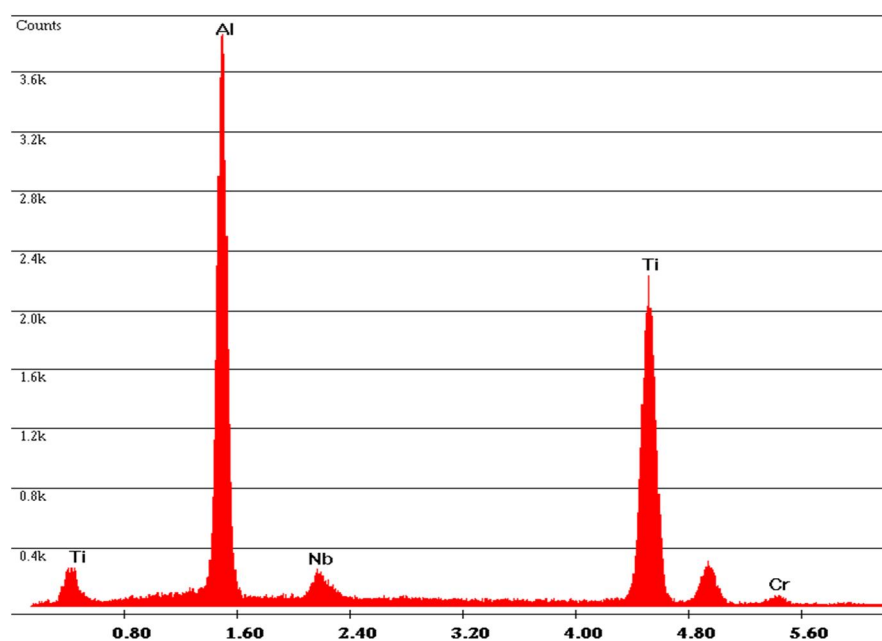
Figure 2.6 EDS chemical composition analysis of TiAl alloy

Table 2.1 Elemental chemical composition in atomic percentage (at%).

Ti	Al	Cr	Nb
49.3	47.12	1.80	2.05

2.3.2 Mechanical Properties of γ -Ti-48Al-2Cr-2Nb: Oliver Pharr and Attaf Method

Indentation tests were performed on sample with an average roughness Ra = 0.0128 µm. Table 2.2 reports the results of the indentation curves analysis performed accordingly to the Oliver-Pharr method after calibration of the instrument compliance and the contact area function. Power law fitting is done considering the (50% -90%)·F_{max} range of the unloading curves.

Table 2.2   Indentation curves analysis according to the Oliver-Pharr method

Samples	E_r(GPa)	E_r (GPa)	H_{op} (GPa)	H_V(MPa)	S(N/µm)	m	HM (MPa)	H_{IT} (MPa)	H/E_r
T(300mN)	149.39	160.06	4.32	368.98	1403.2	1.80	3442.34	3904.55	0.028
T(500mN)	149.74	159.99	4.32	371.90	1818.4	1.74	3395.75	3935.49	0.028
T(1000mN)	130.35	143.53	3.62	314.95	2443.8	1.86	2846.98	3332.81	0.027
T(1500mN)	125.37	136.28	3.53	313.60	2913	1.70	2787.1	3318.62	0.028

E_r- reduced elastic modulus, H_{op}- optimal hardness, H_v, Vickers hardness, S- stiffness, HM- , H_{IT}- ,

Figure 2.7 shows all the recorded ICs. The material reveals elasto-plastic deformation during Vickers indentation. When completing the indentation procedure, a load–unload curves are obtained. They describe the applied force variation F(µN) versus the associated tip displacement h(nm) into the tested material. The resulting hysteresis cycle divides the energy plane $F(h)$ into areas corresponding to different fractions of the involved work-of-indentation. Among these separated energies, the known and commonly used ones are:

i.   The total energy of indentation W_T, located under the loading curve.

ii.   The elastic energy W_E located under the unloading curve and equivalent to the work restored by the material during the tip withdrawal.

iii. The plastic energy W_P causing the permanent deformation of the material and given by the difference W_T-W_E. The corresponding area is enclosed by the two curves.

Till now, use of the energetic aspect remained restricted to W_T, W_E and W_P widely studied and modelled in the literature and often involved in simple analytical or empirical expressions for mechanical properties. To reach a better understanding of mechanical phenomenology in materials, we undertake a wider investigation of this energetic aspect in the case of indentation with Berkovich diamond.
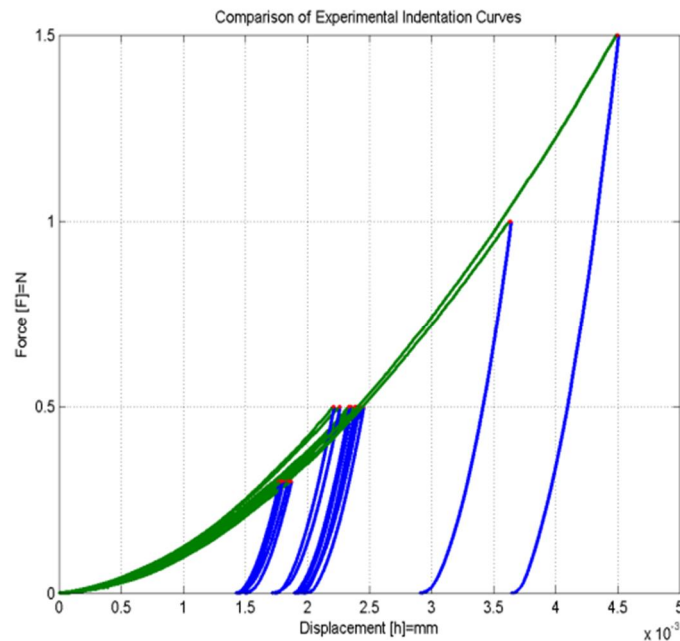
Figure 2.7   **ICs of γ-TiAl at various maximum loads (300mN, 500mN, 1000mN, 1500mN)**

An experimentally measurable parameter to predict the elasto-plastic behavior is the ratio of the final indentation depth h_f to the maximum depth h_{max} which does not depend on the indentation depth. According to the contact mechanics materials can either sink-in or pile-up for an elasto-plastic contact. Giannakopoulos and Suresh (1999) reported that (a) pile-up occurs when $0.875 < (h_r/h_{max}) \leq 1$. (b) No sink-in occurs when $0 \leq (h_r/h_{max}) < 0.875$. (c) No pile-up or sink-in exist when $(h_r/h_{max}) = 0.875$, where the true contact area A and the apparent contact area are equal. This ratio has been used by Cheng and Cheng (1998) to develop a relationship which takes into account also the ratio W_P/W_T for materials characterization. Similarly the same authors developed a relationship also for W_E/W_T which is proportional to the measured H_{IT}/E_{IT} due to the fact that the energetic approach can be extended in understanding the pile-up and sink-in behavior. Table 2.3 and 2.4 reports the values of h_f/h_{max} and $W_E/W_T, W_P/W_T$, respectively. Following the finite element analysis of elastic-plastic deformation during indentation (Oilver and Pharr 2004) one can determine the proportion of elastic and plastic work from the indentation geometry using the expression given in Equation (2.11).

$$\frac{W_E}{W_T} = 1 - \frac{h_r}{h_t} = 5\left(\frac{H}{E^*}\right) \tag{2.11}$$

Table 2.3   Experimental data of the final depth, contact depth, contact area and the ratio of h_f/h_{max}

Force (mN)	h_f (µm)	h_{max} (µm)	h_c (µm)	$h_f/h_{max}A_c$ (µm^2)
300	1.4	1.7	1.6	0.826
500	1.8	2.3	2.1	0.811
1000	2.9	3.6	3.3	0.802
1500	3.6	4.5	4.1	0.804

Even though the prediction shows the pile-up behavior the experimental measurement neither show pile-up nor sink-in which is contradicting to the above quantification represented in the Figure 2.8. Estimated work hardening coefficients is also reported and the average value is equal to 1.67. In our sample the ratio of h_f/h_{max} ranges from 0.80 to 0.82 at various loading conditions showing the pile-up nature but disagrees experimentally. Specific material constants describing the properties of materials proposed by Attaf (2003) were also calculated as total energy, plastic energy, elastic energy, elastic-total energy, plastic-total energy and elastic-plastic energy constants and shown in the Figure 2.9-2.15. It is shown that the absolute deformation energy is increases with given energy factors (Figure 2.9). The relationship of total energy with elasto/plastic energy is given in Figure 2.10. This shown increasing the v_{PT} value ~5.14 compares to v_{ET} ~1.42. This result determines linear correlation of elastic-plastic energy (Figure 2.11). On the basis of elastic-plastic energy diagram, the correlation of deformation energy at maximium load is given (Figure 2.11-2.15). Such correlation clearly shows that deformation energy is depending on the mode of loading energy.
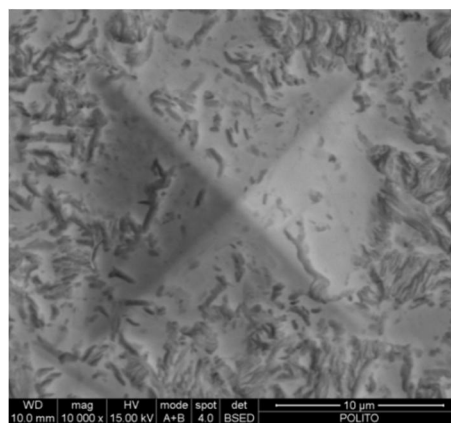
Figure 2.8   **Experimental indentation imprint showing neither pile-up nor sink-in behavior at 10,000X**
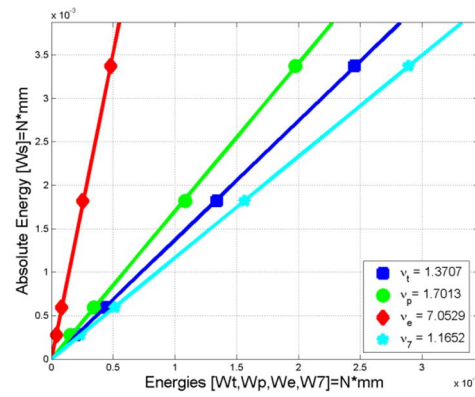
Figure 2.9 Correlation between the absolute energy W_S and other energies (W_T, W_P, W_E, W_7)
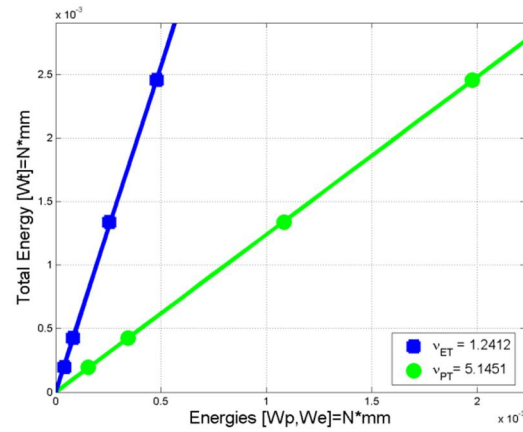
Figure 2.10 Correlation between the total energy W_T and other energies (W_P and W_E)
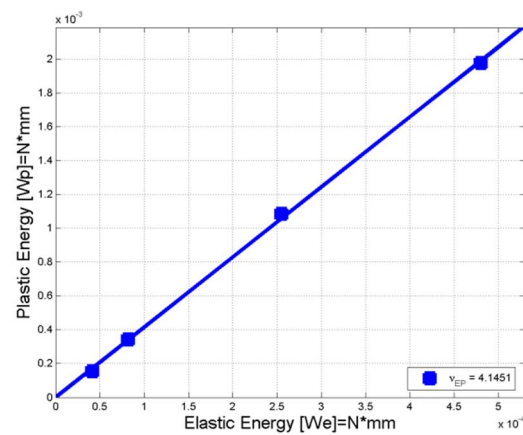
Figure 2.11 Correlation between the plastic energy W_P and the elastic energy W_E
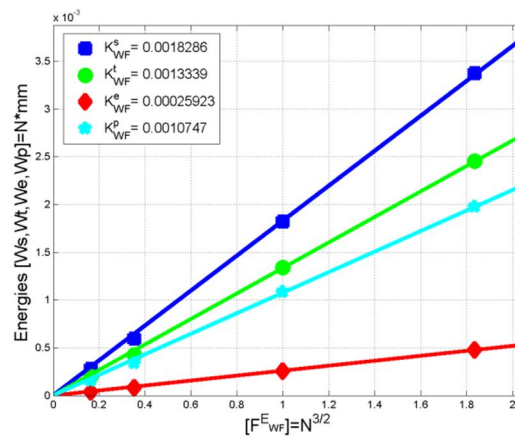
Figure 2.12 **Correlation between energies (W_S, W_T, W_E, W_P) and the maximum load F. E_{WF} is equal to 3/2**
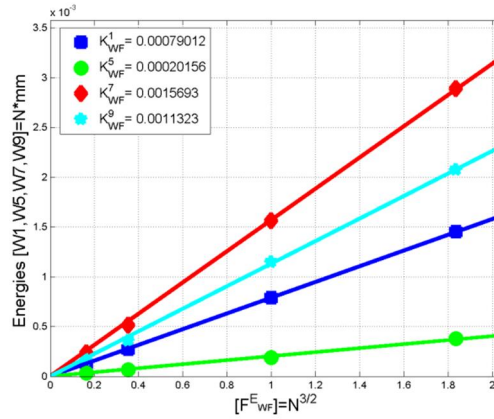
Figure 2.13 **Correlation between energies (W_1, W_5, W_7, W_9) and the maximum load F. E_{WF} is equal to 3/2**
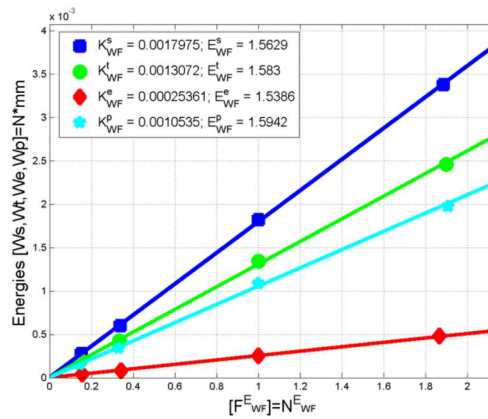
Figure 2.14 **Correlation between energies (W_S, W_T, W_E, W_P) and the maximum load F. $E_{WF} \neq$ 3/2**
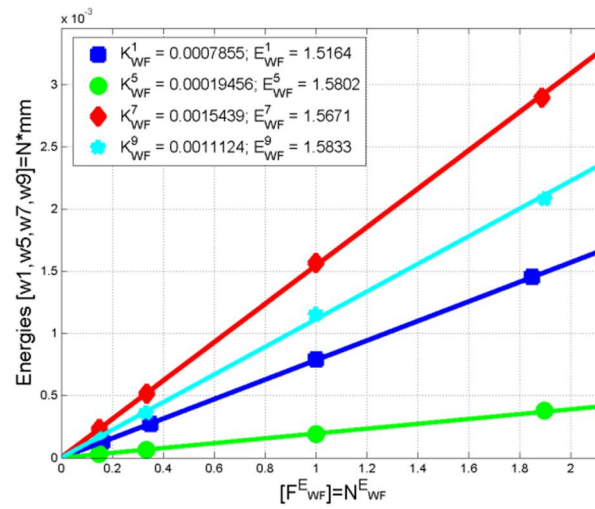
Figure 2.15 Correlation between energies (W_1, W_5, W_7, W_9) and the maximum load F. $E_{WF} \neq 3/2$.

Table 2.4 Proportionality energy constants with the coefficients R^2

Sample	v_T (W_S/W_T)	v_P (W_S/W_P)	v_E (W_S/W_E)	v_{PT} (W_T/W_P)	v_{ET} (W_T/W_E)	v_{EP} (W_P/W_E)
TiAl	1.3757	1.6525	8.1994	5.9586	1.2013	4.9586
R^2	0.999	0.999	0.998	0.997	0.999	0.996

The resulting parameters such as indentation modulus (E_{IT}), reduced modulus (E_r), contact depth (h_c) and the indentation hardness (H_{IT}) are compared with the Oliver-Pharr as shown in the Figure 2.16. Correlation between the displacements and the maximum load is shown in Figure 2.17. There is a good agreement between the two methods hence reliable results can be obtained from the energetic approach as work of indentation is involved and errors related to the measurements may be less.
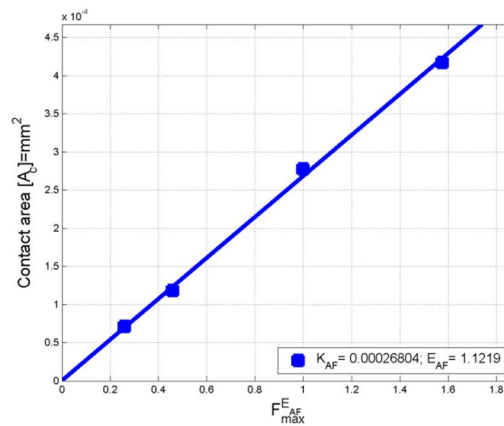
Figure 2.16 Correlation between the contact area A_c and the maximum load F_{max}

The tensile properties of the Ti-48Al-2Cr-2Nb alloy, in the hipped condition are shown in the Table 2.5 which is the average values of tests. The stress vs. strain curves and the final fitting between Hollomon's law and experimental data is shown the Figure 2.18(a-d) for TiAl measured at room temperature. The Young's modulus, yield strength, ultimate tensile strength and elongation at the rupture were provided considering the Hollomon's parameters. The yield strength was determined by identifying the stress at a point on the corresponding stress vs. strain curve where a straight line drawn parallel to the elastic portion of the stress vs. strain at 0.2% offset intersects the curve and the poisson's ratio is 0.263.
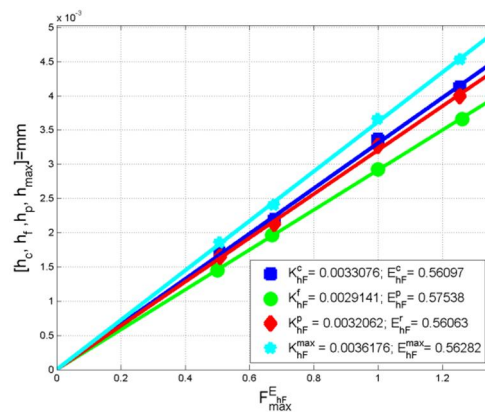
Figure 2.17 Correlation between the displacements (h_c, h_f, h_p and h_{max}) and the maximum load F_{max}
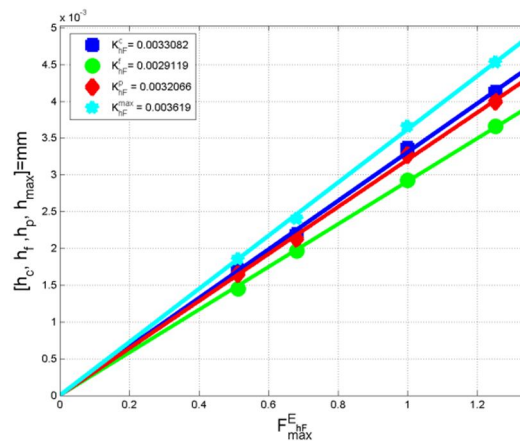
Figure 2.18 **Correlation between the displacements (h_c, h_f, h_p and h_{max}) and the maximum load F_{max}. E_{hF} is equal to the inverse of the mean value of the meyer's index (i.e. $E_{hF} = 0.5549$)**

The yield strength of the intermetallic is 430 MPa taken from the uniaxial tensile tests and the elastic modulus is 174 GPa. The ultimate tensile strength 625 MPa of the γ -TiAl is also marginally higher than the yield strength, indicating that the work-hardening rate past yielding is low. To derive the interpolation parameters of the Hollomon's law, we consider only the experimental points obtained with the strain-gauge between the end of the elastic limit and the point of maximum force. The true values have been calculated. According to the Hollomon's power law equation, the strength index $K = 2377$ MPa, and the strain hardening exponent n is equal to 0.31. Room temperature tensile properties of the titanium aluminide intermetallic are shown in Table 2.5.

Table 2.5 **Tensile properties of the Ti-48Al-2Cr-2Nb alloy, in the hipped condition**

Property	Young's modulusE (MPa)	Yield strength (MPa)	Ultimate tensile strength (MPa)	K (MPa)	n	Elongation at rupture (%)
γ -TiAl	174	430	625	2377	0.31	1.5

Correlation between the displacements and contact area A_c is shown in Figure 2.19 and 2.20. Relation between displacement and maximum displacement is shown in Figure 2.21. Similarly correlation between energies and contact area is shown in Figure 2.22-2.24. Further correlation between energies and maximum depth, final depth and tangent depth is shown in Figure 2.25-2.36. It is clearly seen from the results that with increasing the energy factor the maximum depth, contact depth, final depth and tangent depth is increases. Such approach describes energy released from the deformation is equivalent to the various type of displacement in elasto-plastic regime. This method does not account the energy when materials fracture.
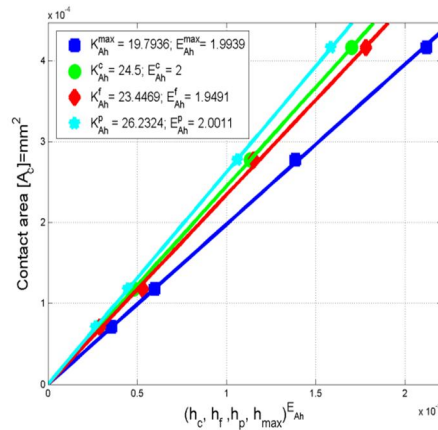
Figure 2.19 Correlation between the displacements (h_c, h_f, h_p and h_{max}) and the contact area A_c
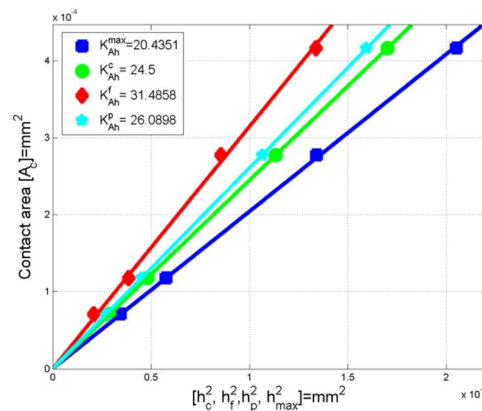
Figure 2.20 Correlation between the displacements (h_c, h_f, h_p and h_{max}) and the contact area A_c. E_{Ah} is equal to 2.
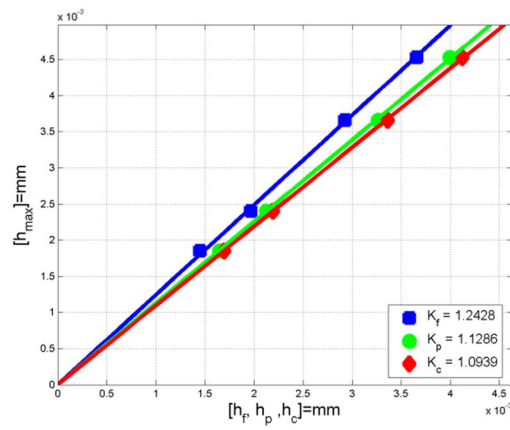
Figure 2.21 Correlation between the displacements (h_f, h_p, and h_c) and the maximum displacement h_{max}
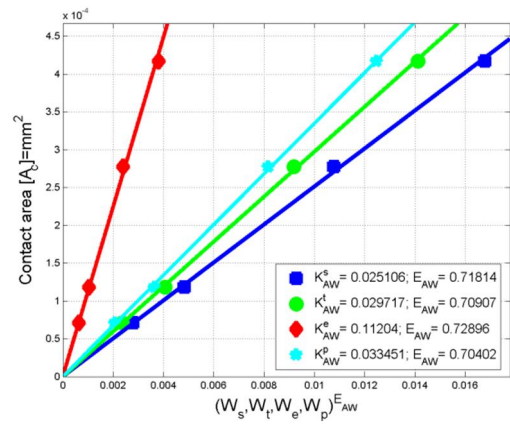
Figure 2.22 Correlation between energies (W_S, W_T, W_E, W_P) and the contact area A_c considering $E_{AW} \neq 2/3 \cdot E_{AF}$
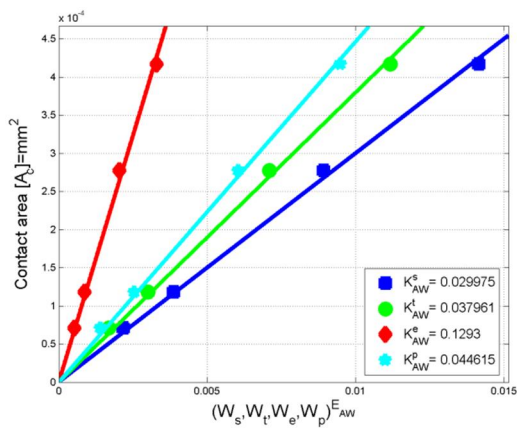
Figure 2.23 Correlation between energies (W_S, W_T, W_E, W_P) and the contact area A_c considering $E_{AW} = 2/3 \cdot E_{AF}$
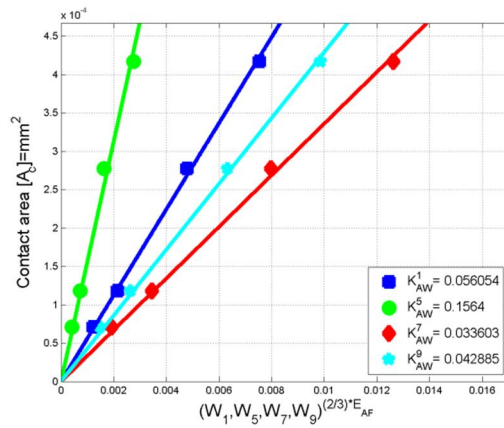
Figure 2.24 Correlation between energies (W_1, W_5, W_7, W_9) and the contact area A_c considering $E_{AW}= 2/3{\cdot}E_{AF}$
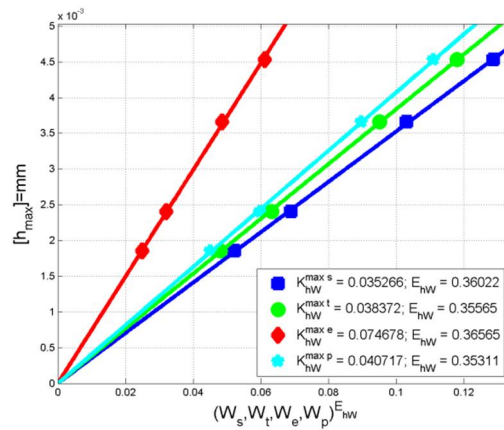
Figure 2.25 Correlation between energies (W_S, W_T, W_E, W_P) and the maximum depth h_{max} for $E_{AW} \neq 2/3{\cdot}E_{AF}$
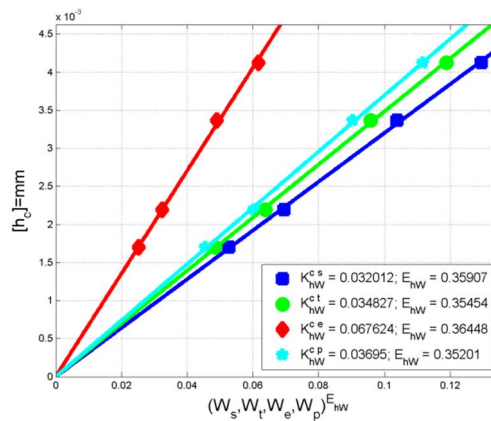
Figure 2.26 Correlation between energies (W_S, W_T, W_E, W_P) and the contact depth h_c for $E_{AW} \neq 2/3{\cdot}E_{AF}$
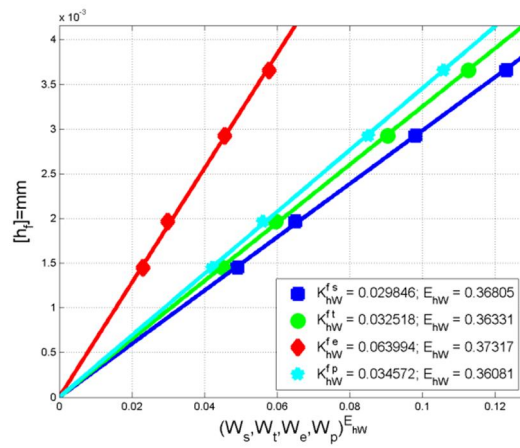
Figure 2.27 **Correlation between energies (W_S, W_T, W_E, W_P) and the final depth h_f for $E_{AW} \neq 2/3 \cdot E_{AF}$**
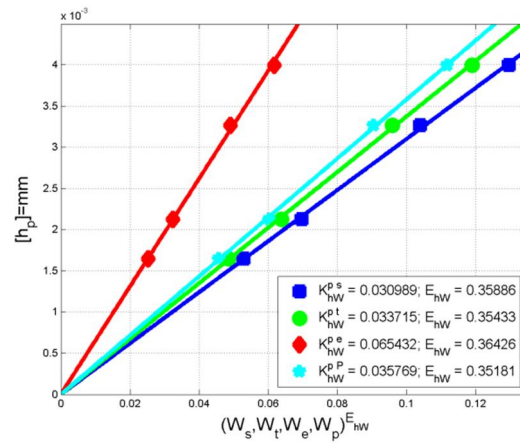
Figure 2.28 **Correlation between energies (W_S, W_T, W_E, W_P) and the tangent depth h_p for $E_{AW} \neq 2/3 \cdot E_{AF}$**
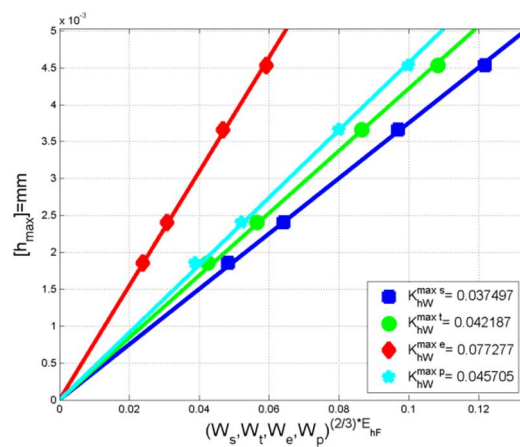
Figure 2.29 **Correlation between energies (W_S, W_T, W_E, W_P) and the maximum depth h_{max} for $E_{AW} = 2/3 \cdot E_{AF}$**
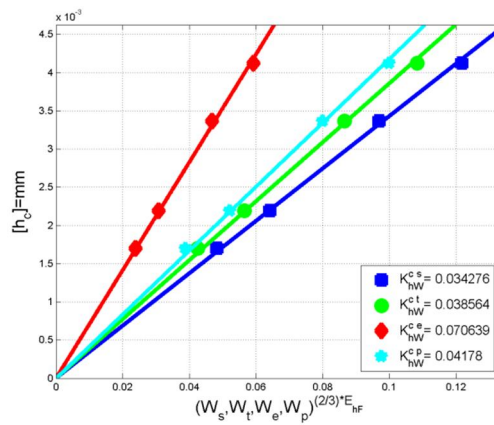
Figure 2.30 Correlation between energies (W_S, W_T, W_E, W_P) and the contact depth h_c for $E_{AW} = 2/3 \cdot E_{AF}$
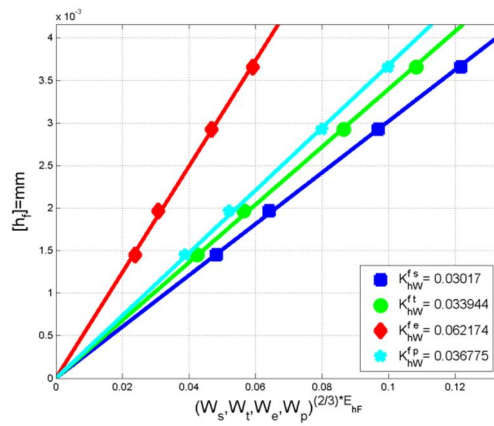
Figure 2.31 Correlation between energies (W_S, W_T, W_E, W_P) and the final depth h_f for $E_{AW} = 2/3 \cdot E_{AF}$
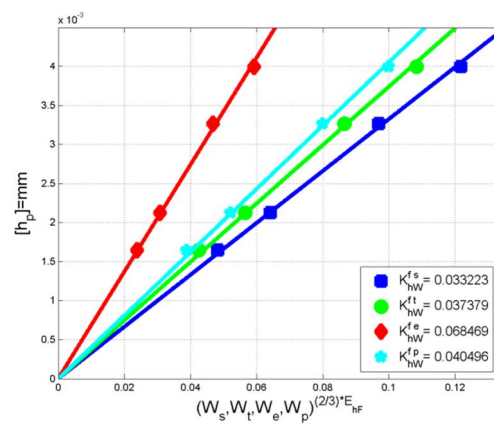
Figure 2.32 Correlation between energies (W_S, W_T, W_E, W_P) and the tangent depth h_p for $E_{AW} = 2/3 \cdot E_{AF}$
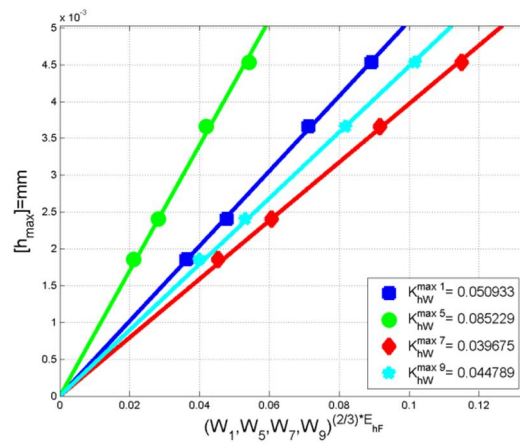
Figure 2.33 **Correlation between energies (W_1, W_5, W_7, W_9) and the maximum depth h_{max} for $E_{AW}= 2/3 \cdot E_{AF}$**
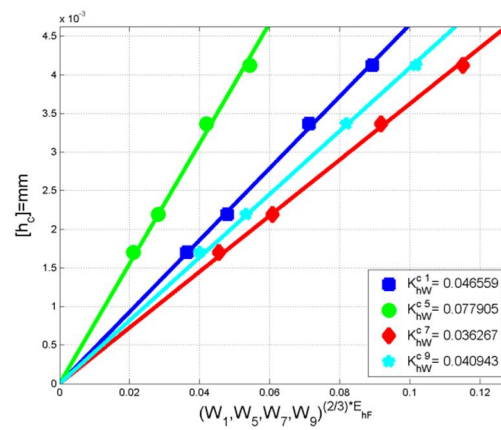
Figure 2.34 **Correlation between energies (W_1, W_5, W_7, W_9) and the contact depth h_c for $E_{AW}= 2/3 \cdot E_{AF}$.**
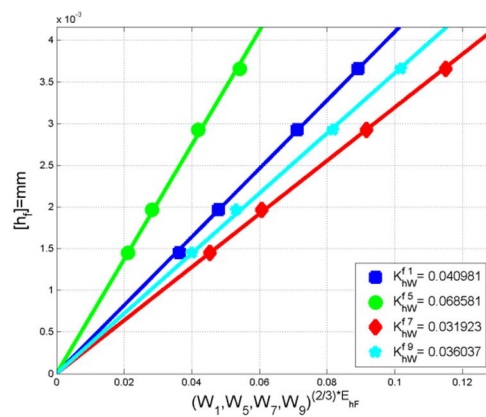
Figure 2.35 **Correlation between energies (W_1, W_5, W_7, W_9) and the final depth h_f for $E_{AW}= 2/3 \cdot E_{AF}$**
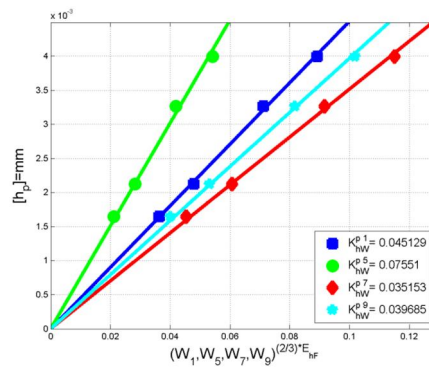
Figure 2.36 **Correlation between energies (W_1, W_5, W_7, W_9) and the tangent depth h_p for $E_{AW}= 2/3 \cdot E_{AF}$.**

2.3.3 Indentation Modulus and Hardness Relationships

Correlation between W_S/E_r and W_S/E_{IT} with energies (W_T, W_E, W_P, W_4, W_6, W_7) is shown in Figure 2.37 and Figure 2.38, respectively. With factor of energy the curve becomes sharper which states high reduced elastic modulus due to energy loss. Figure 2.39 describes exponent m which is extent of deformation vs several energy factor. It is seen that deformation is exponentially increases with some energy. This explains highly developed plastic factor in materials. Figure 2.40 shows Comparison of Oliver-Pharr and Attaf approach. In Oliver-Pharr, the extent of plastic energy is less than the Attaf method. This is explaied that Attaf method does not consider yield plastic limit. In Figure 2.41 to 2.44, several fiting procedure is taken into account to produce the optimal data points.
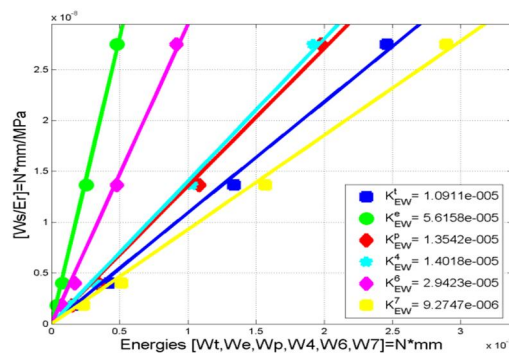
Figure 2.37 **Correlation between W_S/E_r and some energies (W_T, W_E, W_P, W_4, W_6, W_7)**
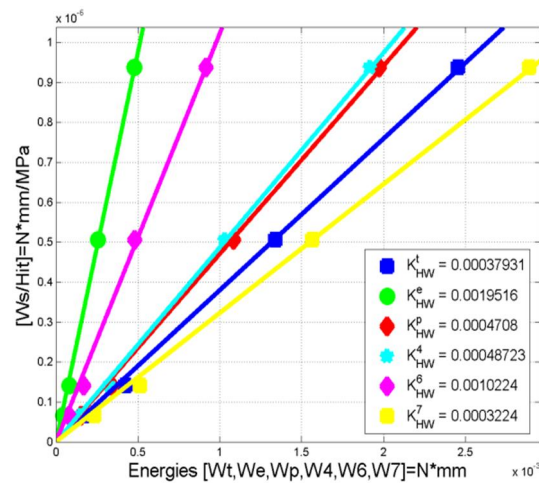
Figure 2.38   Correlation between W_S/H_{IT} and some energies (W_T, W_E, W_P, W_4, W_6, W_7)

2.3.4   Oliver and Pharr Model Relationships

Considering the constants m and A_0 of the Oliver and Pharr (2004) model for the unloading curve, $F=A_0(h-hf)^m$ we found that m is proportional to the energy values in the same way that H and E_r is reduced.
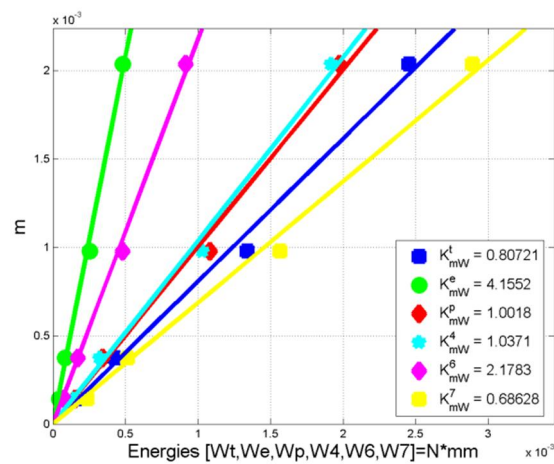
Figure 2.39   Correlation between the exponent m and some energies (W_T, W_E, W_P, W_4, W_6, W_7)
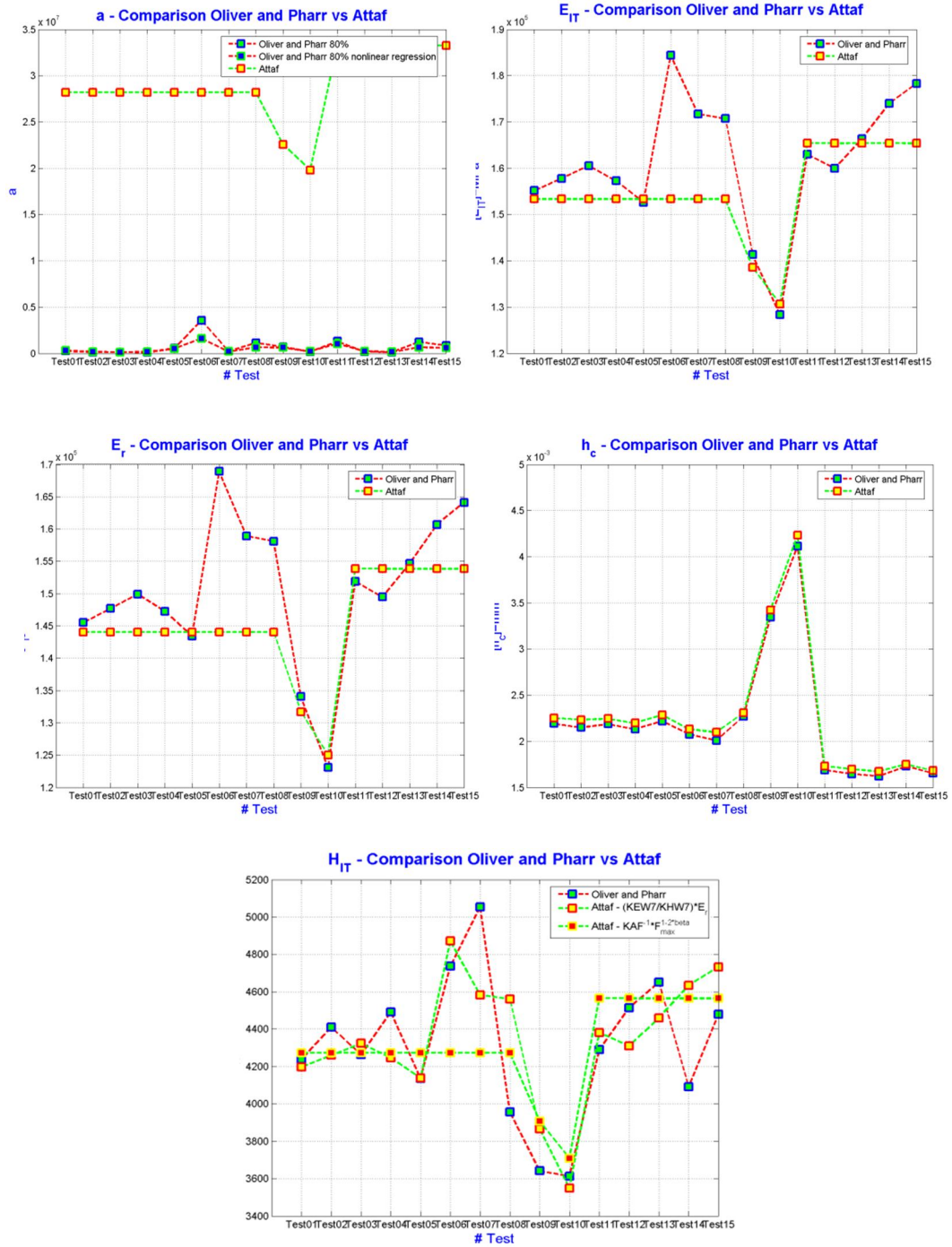
Figure 2.40 Comparison of Oliver-Pharr and Attaf approach for
(a, E_{IT}, E_r, h_c, $H_{IT)}$ parameters)
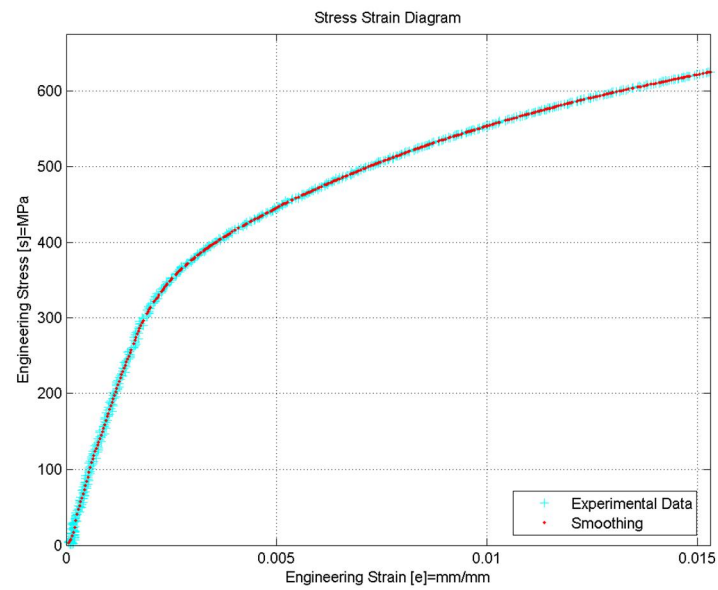
Figure 2.41 Experimental true stress-strain curve before and after numerical smoothing
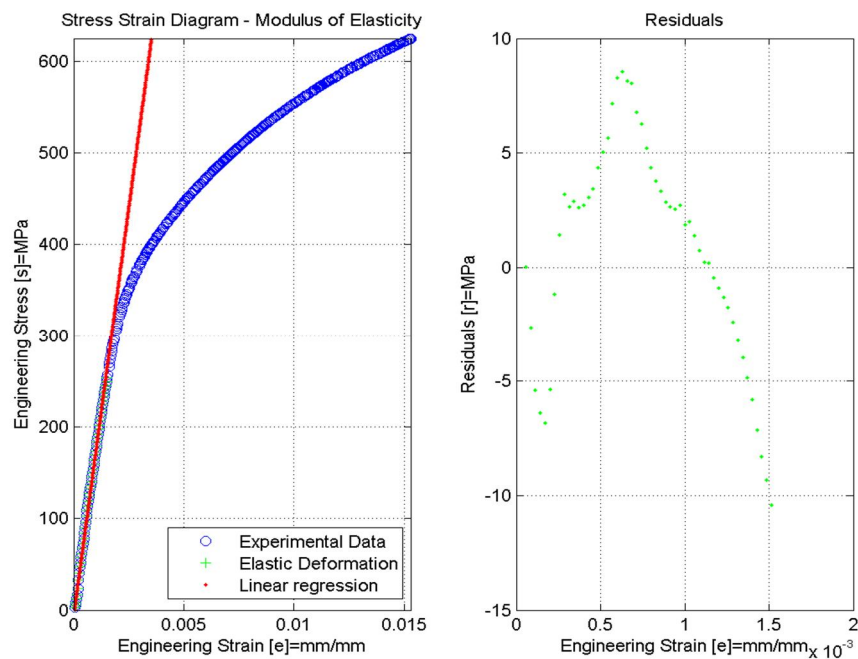
Figure 2.42 Best-fitting for Young's modulus estimation
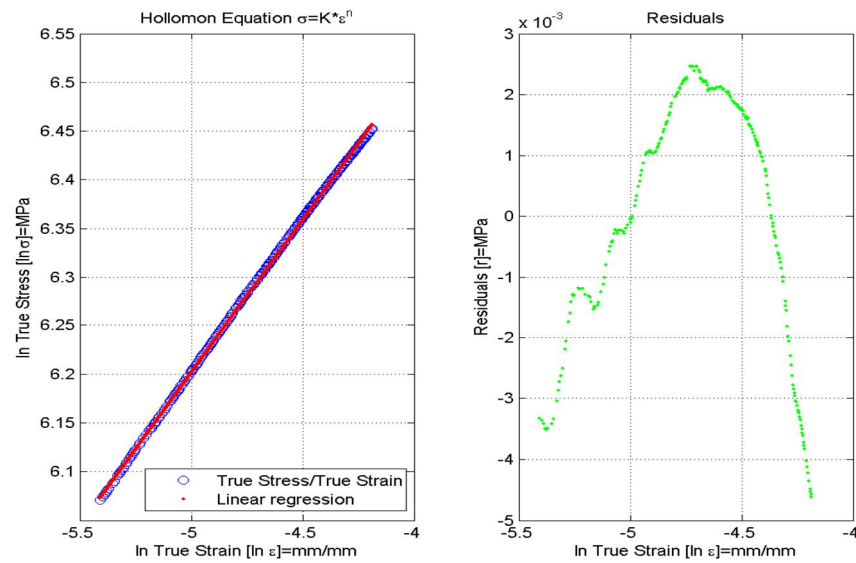
Figure 2.43   **Non linear regression for the estimation of the Hollomon's power law parameters**
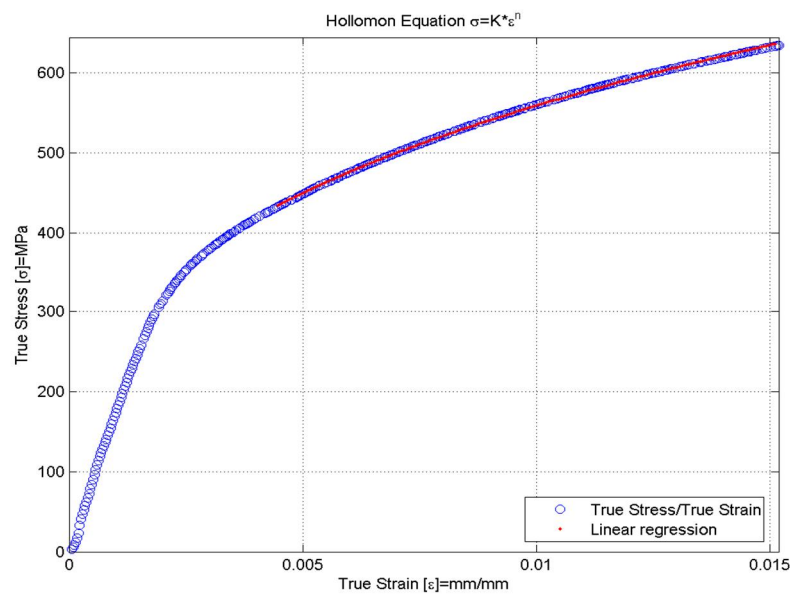
Figure 2.44   **Final best fitting between Hollomon's law and experimental data for the entire tensile test curve.**

2.4   TRIBOLOGICAL PROPERTIES

Friction coefficient of γ-TiAl alloy was measured against three different kinds of balls such as Al_2O_3, SiC and Cr6 steel as shown in Figure

2.45. Same size of the ball (6 mm in diameter) was used for this measurement. Heartzian contact pressure was 0.6, 1.2 and 1.8 GPa in Cr6 steel, SiC and Al_2O_3 balls, respectively. The magnitude of this value is high when it slides against Al_2O_3 and SiC balls as shown in Figure 2.45(a) and (c). However, against steel ball it shows less value of friction coefficient as shown in Figure 2.45(b). As well penetration depth is more or less similar in all the cases as shown in Figure 2.46. However, deformation behavior of wear track is different while using these balls. It is shown in Figure 2.47. The wear track width is large when Al_2O_3 and SiC balls slides against γ-TiAl alloy as shown in Figure 2.47(a) and (c). However, against steel ball it shows narrow wear track as shown in Figure 2.47(b).
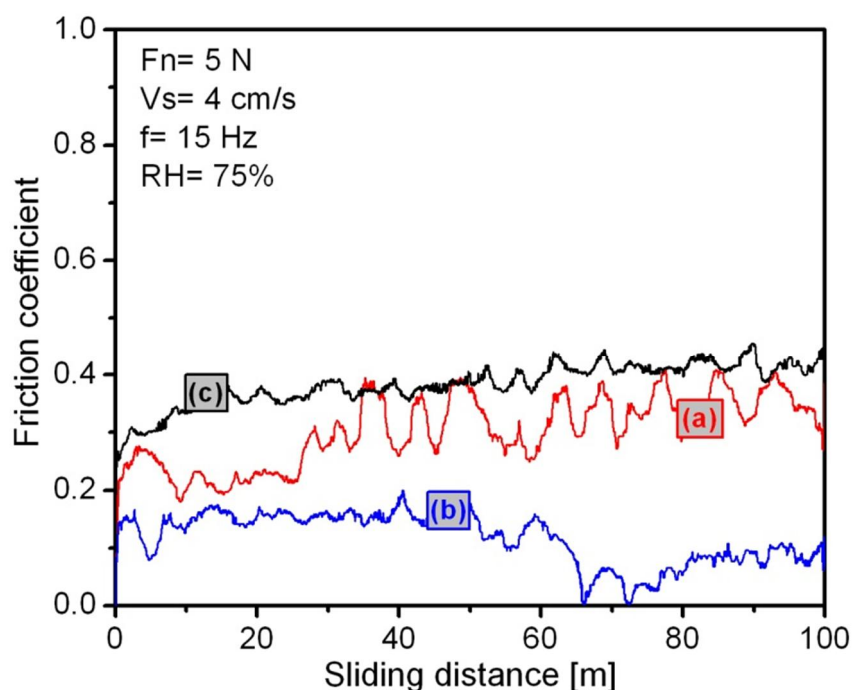
Figure 2.45 Friction behavior of γ-TiAl alloy sliding against (a) Al₂O₃ (b) SiC and (c) steel ball

In this accordance, the relationship of friction coefficient and deformation behavior of wear track is similar. The Al_2O_3 and SiC balls are harder which is more capable to deform the γ-TiAl alloy. The hardness and

elastic modulus values are shown in Table 2.6. In this case, both the sliding interfaces (coating and ball) are harder which acts to deform more. This is the basic reason that harder balls such as Al_2O_3 and SiC shows high friction coefficient. When harder interfaces slides, the wear mechanism is governed by abrasive wear (Wang et al 1997, Holmberg et al 1998). However, steel ball is less hard compared to other two balls. In this condition, deformation of γ-TiAl alloy is less. This explains less deformed and narrow wear track when steel ball slides against γ-TiAl alloy. In all the three cases, the wear rate k of the alloy is calculate considering wear volume V, normal force F and sliding distance S. The expression is given in Equation (2.12).

$$k = V/(F \times S) \tag{2.12}$$

This value is lowest 2.8×10^{-7} mm^3/Nm while γ-TiAl alloy slides against SiC ball. However, this value increases to 1.8×10^{-6} mm^3/Nm and 4.7×10^{-6} mm^3/Nm while sliding against Al_2O_3 and steel balls, respectively. The trend of wear rate follows the trend of friction coefficient. The wear rate is less where friction coefficient is lower.
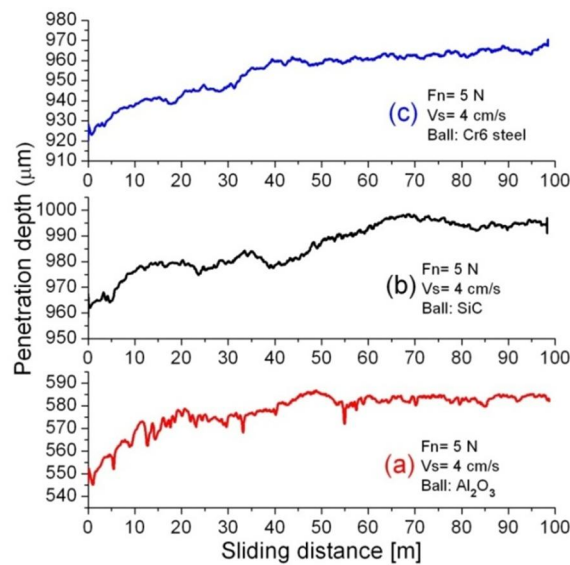
Figure 2.46 Insitu penetration depth of γ-TiAl alloy sliding against (a) Al$_2$O$_3$ (b) SiC and (c) steel ball
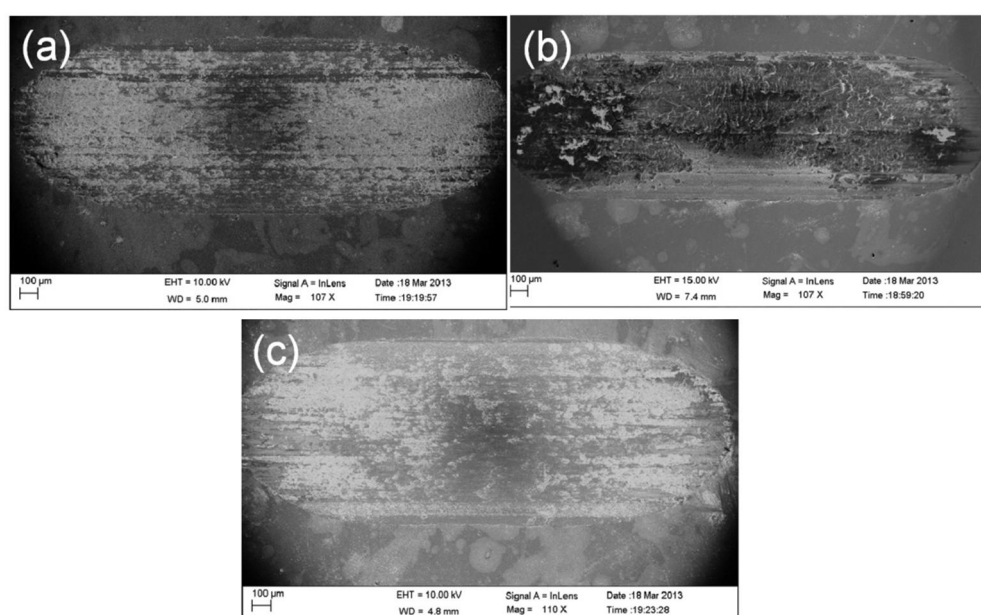
Figure 2.47 **Wear track deformation of γ-TiAl alloy sliding against (a) Al₂O₃ (b) SiC and (c) steel ball**

Table 2.6 **Hardness and elastic modulus of γ-TiAl alloy and counterbody balls**

	H (GPa)	E (GPa)
γ-TiAl alloy	0.22	11.98
100Cr6 steel	2.7±0.2	185±17
SiC	22±1.8	345±28
Al₂O₃	26±2.3	382±32

The origin of friction and wear mechanism observed in macroscopic level is related to microscopic one (Holmberg et al 1998). The micromechanical tribological mechanisms describe the stress and strain formation at an asperity-to-asperity level, the crack generation and propagation, material release and particle formation. Shear and fracture are two basic mechanisms for the first nucleation of a crack and for its propagation, until it results in material release and the formation of a wear scar and wear particle (Holmberg et al 1998). An important parameter is the

hardness of the sliding interfaces and its relationship. It is common to consider hard and soft materials. The advantages of soft materials is to reduce friction are well known. Soft materials have the function of reducing sliding originates from surface tensile stresses, which contribute to undesirable subsurface cracking and subsequently to severe wear. A hard material on a softer ball can decrease friction and wear by preventing ploughing both on a macro scale and a micro scale. These materials typically exhibit residual compressive stresses which can prevent the tensile forces.

2.5   CONCLUSION

Instrumented microindentation tests were performed on γ -Ti-48Al-2Cr-2Nb alloy after hipping at various loads using a Vickers indenter. Hardness and elastic modulus are calculated by the Oliver-Pharr method and the energetic approach by Attaf. The indentation hardness and elastic modulus calculated from the work of indentation approach seem to correlate very well with the Oliver-Pharr method at lower as well as higher loads. Deviations in the average hardness may be attributed to the fact of the surface roughness and the mechanical polishing effects. The ratio of h_f/h_{max} ranging from 0.80 to 0.82 at various loads indicates the pile-up effect theoretically, there is a disagreement experimentally. In addition some specific material constants describing the properties of materials such as (v_T, v_P, v_E, v_{ET}, v_{PT}, v_{EP}) are calculated. The processing route HIP and AEBM process which are successfully being used for the production of γ –TiAl alloys having exceptionally high strength index (K) and nominal yield strength after the Holloman's fitting.

Tribological behavior of γ-TiAl alloy is investigated while sliding against 100Cr6 steel, SiC and Al_2O_3 as counterbodies for friction pairs. The friction coefficient and wear rate was high when γ-TiAl alloy slides with

Al_2O_3 and SiC ball. However, these values were less while sliding against steel ball. The wear mechanism is explained by the sliding combination of harder/softer such as SiC/γ-TiAl and Al_2O_3/γ-TiAl alloy. However, less harder/softer sliding combination acts in steel/γ-TiAl alloy. Penetration depth during friction measurement shows more or less similar value. This means that the magnitude of composite wear is similar in all the three sliding combination. However, deformation of wear track follows the trend of friction coefficient. The wear track is wider in the sliding combination of SiC/γ-TiAl and Al_2O_3/γ-TiAl alloy. However, in steel/γ-TiAl alloy sliding combination the wear track was narrow.

CHAPTER 3

TRIBOLOGICAL PROPERTIES OF TiAlN COATING SLIDING AGAINST Al₂O₃, SiC AND STEEL BALLS

3.1   INTRODUCTION

TiAlN are ternary nitride system which is technologically important materials for various applications including wear resistant and oxidation resistance at high temperature. Oxidation resistance of TiAlN is governed by higher chemical stability, in comparison to binary nitrides like TiN and AlN coatings (Suresha et al 2006, Zhang et al 2006, Bressan et al 2001, Keunecke et al 2010, Torres et al 2010, Seog-Young et al 2010). In this material, TiN is constituted as rock salt structure with metallic conductivity at room temperature (Spengler et al 1978). However, AlN crystallizes in a wurtzite structure and it may form a metastable rocksalt structure at high pressure (Vashishta et al 2011). The incorporation of Al in the face centered cubic (fcc) TiN structure on Ti sites has led to the development of TiAlN. The structural refinement of TiAlN alloy improves its hardness, high temperature oxidation and wears resistance (Bressan et al 2001, Keunecke et al 2010). Thus, the TiAlN is considered as a multifunctional coating. The high hardness of the TiN acts to prevent the wear loss during the sliding. In contrast, soft phase like AlN is useful for low friction coefficient. Moreover, wear and friction behavior is complex phenomena when several composition and phases are get involved in the TiAlN film (Suresha et al 2006, Zhou et al 2010). Given the complexity of tribochemical interaction and multitude of

phases at the sliding interfaces, the plastically deforming wear mechanism becomes complex. Deformation is vastly associated to the combination of hard and soft sliding bodies. Moreover, wear behavior of any material depends on microstructure and chemical composition of sliding pairs. These pairs cause the formation of composite tribofilm during the sliding. Nature of such film is an important factor which attributes to the wear and friction mechanism. Therefore, it is important to understand friction mechanism of tribologically important TiAlN hard coating sliding with various counterbodies forming the tribofilms and their wear mechanism.

In this chapter, friction and deformation behavior of TiAlN coating sliding with metallic 100Cr6 steel, ceramic Al_2O_3 and SiC spherical counterbodies is studied. Deformation behavior of corresponding wear tracks are investigated by SEM. In addition, Raman spectroscopy is used to determine the chemical changes in the wear track corresponding to different sliding counterbodies. The correlation of friction and wear mechanism is drawn in the respect of chemical changes and deformation behavior. Moreover, mechanical properties such as hardness and elastic modulus are also investigated to explain the tribological mechanism.

3.2 EXPERIMENTAL METHODS

3.2.1 Film Deposition and Microstructure

The PVD technique based magnetron sputtering was used to deposit the coating. In this process, the co-sputtering of metallic titanium (99.99%) and aluminum (99.99%) targets was used. The Ti and the Al targets were powered by Direct Current (DC) and Radio Frequency (RF) magnetron sputtering, respectively. Both of DC and RF power were fixed at 200 W. In order to acquire well crystallized and uniform coatings, the substrate was preheated to a prescribed temperature of $450^{o}C$ and rotated with 30 rpm

during the deposition. The distance between the target and the substrate was about 22 cm. The base pressure of the sputtering chamber was evacuated below 4.5×10^{-4} Pa by a turbo molecular pump backed by a rotary pump. The flow rates of N_2 and Ar gases were controlled separately by mass flow controllers. The coatings were prepared at a nitrogen gas flow rate of 10 sccm. The 2 h deposition process was carried out at a fixed sputtering pressure of 0.5 Pa. The substrate material WC-12Co binder was mirror polished before the deposition. High roughness of the films supports in increasing the hardness value. Hardness evaluation of thin films is always a complicated task due to the uncertainty of the appropriate indentation load. Depending on the coating thickness and substrate material, the system involved (hard coating/soft substrate, soft coating/hard substrate) appropriate load to characterize the coating hardness. For a coating surface, the effective elastic modulus is a combination of the coating and the substrate. For hardness measurement, the indentation depth should be less than one-tenth of the coating thickness. Hence, the crucial problem is to investigate the film properties independent of the underlying substrate in the film microhardness testing (Manika and Maniks 2008). The morphologies of the film surface were examined using SEM. Nanoindentation measurements were carried out with Berkovich diamond indenter at a constant loading/unloading rate of 5 mN/min. The tests were conducted at a peak load of 10 mN. The formalism of Oliver and Phar (1992) was used to calculate the elastic modulus and hardness of all the specimens.

3.2.2   Tribology Test and Characterization Techniques

Linear reciprocating mode of ball on the disk micro- tribometer (CSM Instruments, Switzerland) was used to carry out the friction

measurements. In these measurements, the normal load and sliding speed were constant 5 N and 4 cm/s, respectively. Three different kinds of balls counterbodies such as 100Cr6 steel, SiC and Al_2O_3 were used for sliding against TiAlN coating. The diameter of the ball was 6 mm. Surface roughnesses of the balls were 0.04, 0.02, and 0.03 µm for 100Cr6 steel, SiC and Al_2O_3, respectively. Tribological experiments were conducted in ambient atmospheric condition at room temperature where the relative humidity was 75%. Insitu wear track depth was measured by LVDT sensor coupled to the micro- tribometer. In addition, wear profile after the test was measured by Dektak 6M–stylus profiler using 5 mg load with a scanning speed of 30 µm/s. In this method, tip of diamond stylus with a radius of curvature of 12.5 µm was scanned across the wear track. On each sample, wear profile was measured five times and it was found to be reproducible.

The surface morphology and microstructure of the coatings were analyzed using a FESEM (CARL ZEISS SUPRA 55). EDS was used for elemental analysis of wear tracks. High Resolution X-ray Diffraction (HRXRD) measurement was carried out to obtain the structural information of coating. The incident angle of the x-ray was 0.8^{o}. The Raman spectra on the surface and wear tracks were recorded in back scattering geometry with a Renishaw micro-Raman spectrometer (Model INVIA), equipped with Ar-ion laser, wavelength 514.5 nm. In these measurements, 100% laser beam was used for 60 minutes of spectra exposure time.

3.3   MORPHOLOGY AND MICROSTRUCTURE

Morphology and cross section of the TiAlN coatings were observed by SEM and these are shown in Figure 3.1.
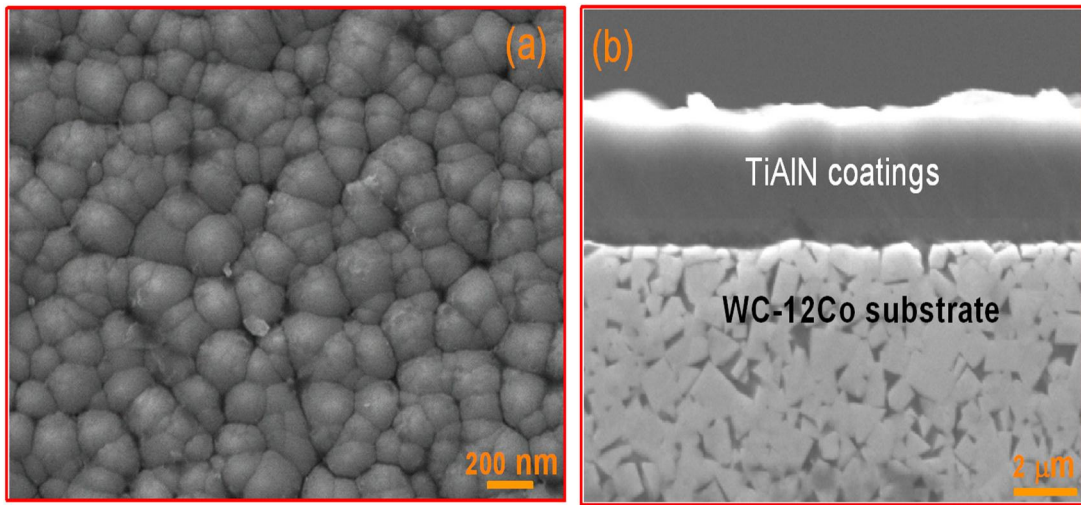
Figure 3.1   Morphology of the film surface observed by scanning electron microscope

Morphology of the coating is shown in Figure 3.1(a) represents densely packed well defined grains. Smaller grains are locally surrounded by bigger grains. These smaller grains are formed due to secondary nucleation that does not grow further due to high interface energy (Irudayaraj et al 2007, Beckers et al 2007). In addition, growth of these smaller grains is restricted by surrounding larger grains. The boundaries of the grains are sharp which consist of chemical defects. These defects influence on the microstructure of TiAlN coating. Hardness and elastic modulus of the film are 22 GPa and 380 GPa, respectively, as measured by nanoindentaion technique. The hardness and elastic modulus with H^3/E^2 factor for TiAlN coating and various balls were calculated and these are given in the Table 3.1. Cross section of the coating is shown in Figure 3.1(b) which represents coating thickness and sharp coating/substrate interface. In addition, cross section of WC-12Co substrate is also shown.

Table 3.1   **Microstructure and plastic index of TiAlN coating and counterbody balls**

	H (GPa)	E (GPa)	H^3/E^2
TiAlN film	28±2	380±20	0.0054
100Cr6 steel	2.7±0.2	185±17	0.00057
SiC	22±1.8	345±28	0.09
Al$_2$O$_3$	26±2.3	382±32	0.12

In Figure 3.2, the HRXRD pattern shows that the coating is polycrystalline in nature which consists of three phases such as TiAlN, AlN and TiN (Schuster and Bauer 1984, Wright and Nelson 1995).
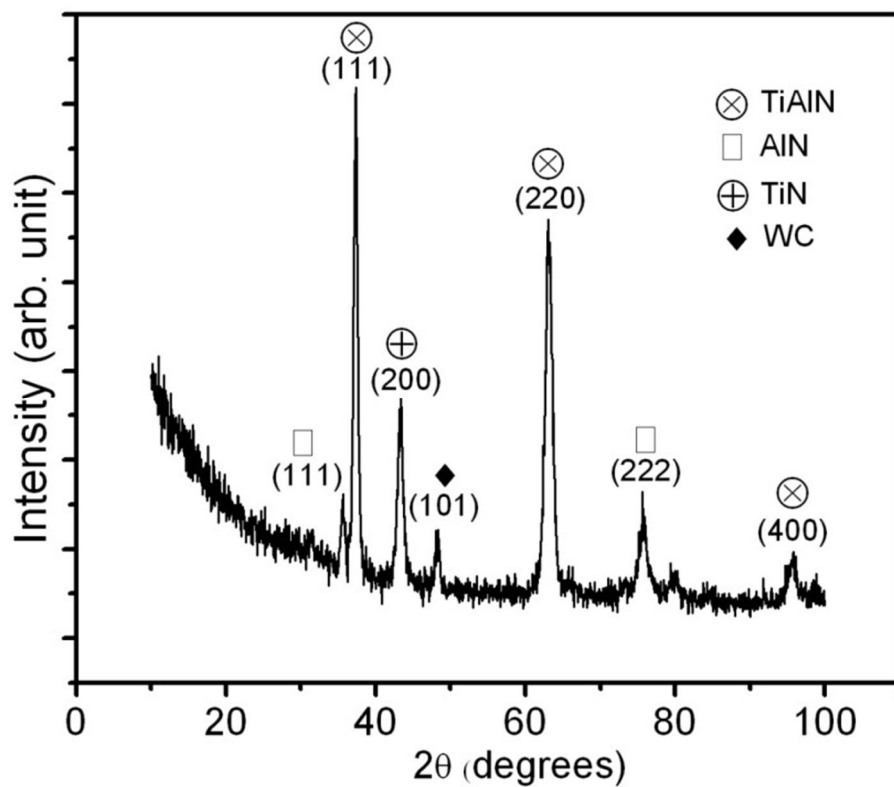
Figure 3.2 High resolution XRD of TiAlN coating

Cubic structure of TiAlN is predominant with the orientations of (111), (220) and (400). WC-12Co peak exists due to substrate. The shift of TiAlN phase to high 2θ angle corresponds to compressive stress which arises due to defect concentration.

3.4   WEAR MECHANISM

Tribological properties of this film are studied by steel, SiC and Al_2O_3 balls as shown in Figure 3.3. Friction coefficient of the sliding system TiAlN/steel is 0.3 which decreases to 0.17 in the TiAlN/SiC sliding system. However, friction coefficient of TiAlN/Al_2O_3 sliding system is significantly higher 0.6–1.0.
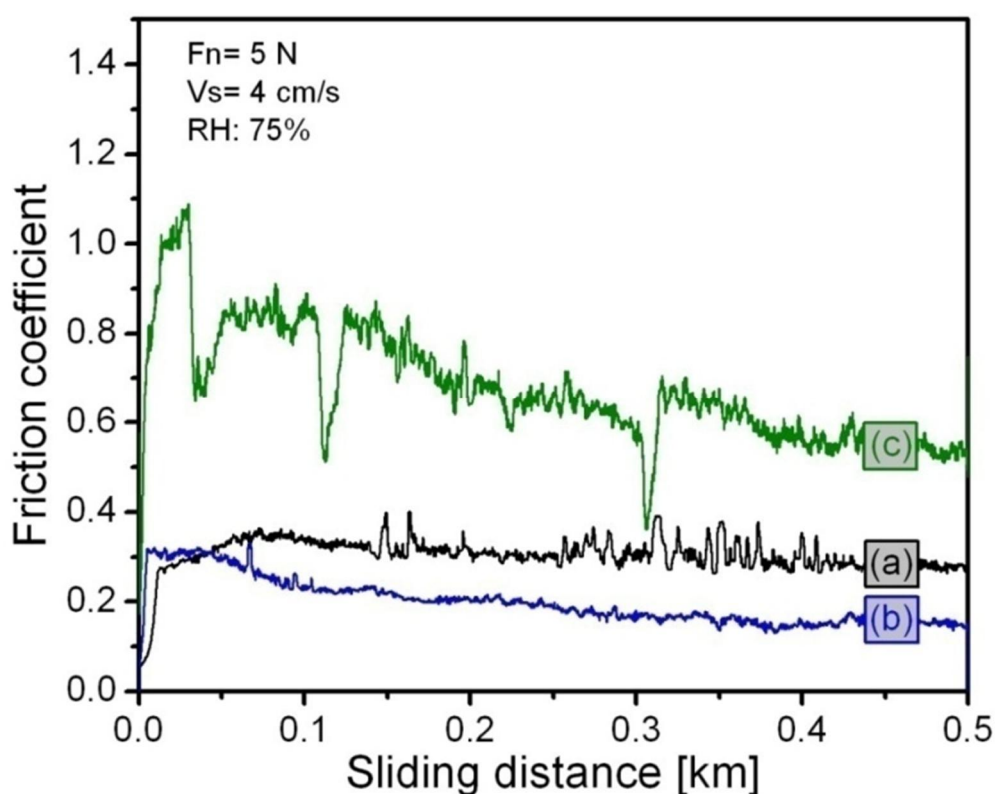
Figure 3.3   Friction coefficient of TiAlN film sliding with (a) Cr6 steel (b) SiC and (c) Al$_2$O$_3$ balls

The friction curve is unstable in the case of TiAlN/steel and TiAlN/Al$_2$O$_3$ sliding systems. This instability appears due to large scale deformation during the sliding. Nature of deformation behavior of sliding systems was studied by insitu wear depth measurement with LVDT sensor as shown in Figure 3.4. In the system of TiAlN/steel, the penetration depth consistently increases with sliding distance as shown in Figure 3.4(a). This behavior describes that wear loss from the ball is quite significant.
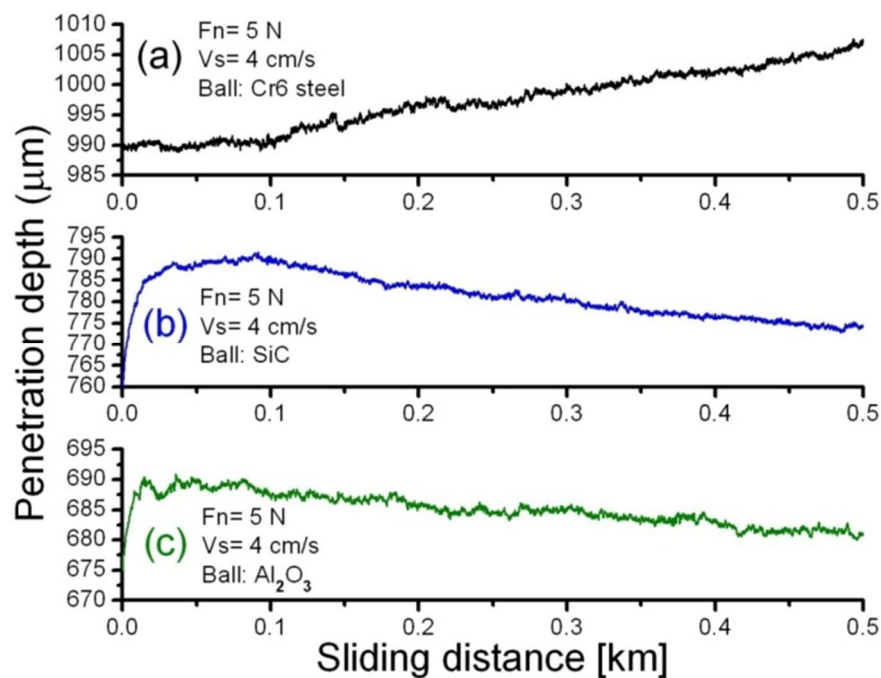
Figure 3.4   Insitu penetration depth of TiAlN film sliding with (a) Cr6 steel (b) SiC and (c) Al$_2$O$_3$ balls

Such a characteristic is ascribed to the softness of the steel ball which deforms easily as compared to the hard TiAlN coating (Chom-Cheng et al 1993). This is well supported by the wear profile of the TiAlN/steel system as shown in Figure 3.5(a). In this profile, the wear depth on the TiAlN coating is not observed. In contrast, dense line spikes are observed on the positive side of the scale.
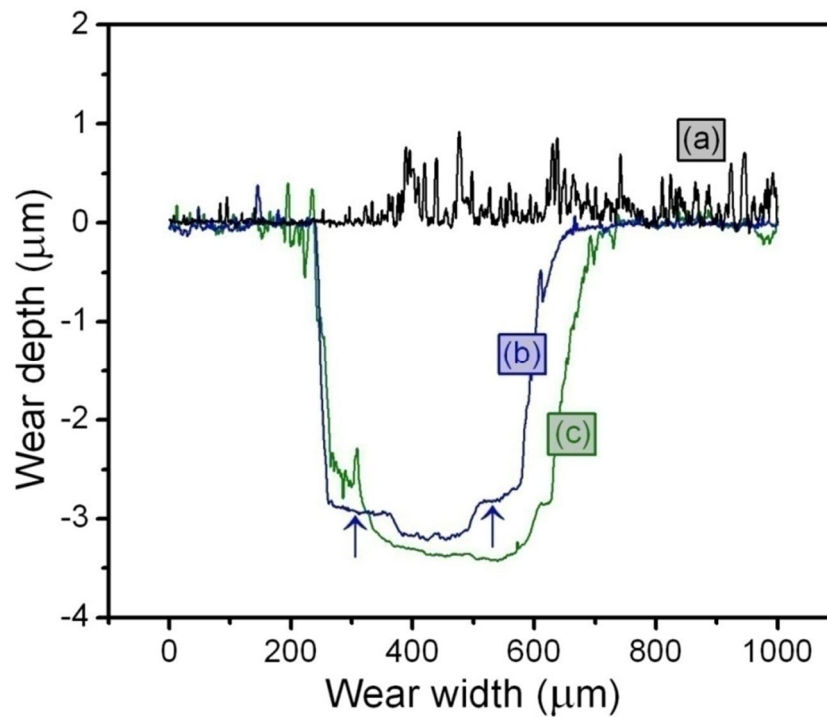
Figure 3.5   Wear profile of TiAlN film sliding with (a) steel (b) SiC and (c) Al$_2$O$_3$ balls

This confirms that, wear loss from the ball occur which forms inhomogeneous layer of wear particles of the steel ball. However, wear depth is decreased with sliding distance in TiAlN/SiC and TiAlN/Al$_2$O$_3$ sliding systems as shown in Figure 3.4(b) and Figure 3.4(c), respectively. This characteristic is due to large scale deformation of TiAlN coating while sliding with SiC and Al$_2$O$_3$ balls (Zhou et al 2010). This is in agreement with the wear profile which is large in TiAlN/SiC and TiAlN/Al$_2$O$_3$ sliding pairs as shown in Figure 3.5(b) and Figure 3.5(c), respectively. The larger dimension of wear tracks corresponds to high wear rate of TiAlN coating which is more or less similar to the wear loss from contacting balls. This is related to the high hardness and elastic modulus of the SiC and Al$_2$O$_3$ balls which are comparable to the TiAlN coating. It is noticed that initially, wear loss from the ball is significantly high in the sliding pair of TiAlN/SiC and TiAlN/Al$_2$O$_3$. This behavior is explained by large local contact stress of the

contacting pairs due to reduced contact area. This causes high wear loss (Grzesik et al 2006, Tillmann et al 2010). Once, contact area of the sliding pairs is increased due to wear loss, the contact stress progressively decreases and wear loss is normalized.

Further, wear loss can be understood by calculating the ratio of hardness and elastic modulus of pairs such as TiAlN/steel, TiAlN/SiC, and TiAlN/Al$_2$O$_3$ with resulting values 10.3, 1.27, 1, respectively. Similarly, ratio of elastic modulus follows the trend of hardness ratio of the pairs. It is 2, 1.1 and 0.9 in TiAlN/steel, TiAlN/SiC, and TiAlN/Al$_2$O$_3$, respectively. From this analysis, it is clearly seen that the difference in hardness and elastic modulus of TiAlN coating and steel ball is significant. This characteristic indicate high wear rate of steel ball (Grzesik et al 2006). However, insignificant difference of these ratios is observed in TiAlN/SiC, and TiAlN/Al$_2$O$_3$ pairs. Therefore, the difference in wear volume is marginal in TiAlN/SiC and TiAlN/Al$_2$O$_3$ sliding pairs as shown in Figure 3.5. Similarly, the difference in wear rate of TiAlN film sliding against SiC and Al$_2$O$_3$ is less as shown in Table 3.2.

Table 3.2 Friction and wear rate of TiAlN sliding with steel, SiC and Al$_2$O$_3$ balls

Sliding pairs.	μ	k, Ball (mm^3/Nm)	k, TiAlN (mm^3/Nm)
TiAlN/steel	0.3	2.8×10^{-4}	4.0×10^{-10}
TiAlN/SiC	0.17	4.3×10^{-7}	1.7×10^{-7}
TiAlN/Al$_2$O$_3$	0.45	5.7×10^{-6}	2.3×10^{-6}

The wear loss and deformation is evaluated by calculating the H^3/E^2 factor which indicates resistance to plastic deformation. This ratio is

less in steel ball which describes less resistance for plastic deformation. However, resistance is high in SiC and Al_2O_3 ball which is directly supportive to the calculated value of reduced wear rate. Wear volume V of ball is calculated from the method used by Qi and Vohra (2008) and given in Equation (3.1).

$$V= \pi t^2 (3r-t)/3 \qquad\qquad (3.1)$$

Here, t represents thickness of the transferred layer after the sliding event, r is the radius of the ball and d is the diameter of the transfer layer which is known to be equal to the width of wear track of the coating. d is measured directly from the scar of the ball and it represents t in the above formula. If the wear volume is known, the wear rate is obtained from the Equation (2.12). This equation is general and it has been used to calculate the wear rate of both coating and the ball.

3.4.1 Deformation Mechanism of Wear Track

The wear loss and deformation mechanism in these sliding pairs are elaborately studied by SEM and EDS. The results are presented in Figure 3.6. In this figure, wear track of the sliding system of TiAlN/steel is shown. Low and high magnified images shows that wear track is fully covered by the oxide scales and metallic debris of steel ball. It is well evident from the wear profile where wear track is absent, as seen from Figure 3.5(a). Therefore, line spikes to the positive side on the scale are clearly observed. This arises due to the interaction of hard TiAlN and soft steel ball where loss of wear from the steel ball is quite significant on the intact TiAlN coating (Barshilia and Rajam 2005, Chen et al 2011). The wider wear scar of ball is shown in the inset of

Figure 3.6. This behavior supports increase in penetration depth vs sliding distance in TiAlN/steel sliding pair. This is shown in Figure 3.4(a). Penetration is due to the wear loss from the ball and it is clearly shown in wear profile Figure 3.5(a). However, edges of the wear track are partially covered by oxide scales. In this image, it is clearly seen that the background contains TiAlN grains which does not deform Figure 3.5(a). It is protected by the thick oxide scales which are in the form of oxide nanoparticles. Formation of such nanoparticles occurs due to oxidation process induced by sliding. The evidence of metallic oxide is ascribed to the formation of Fe and Cr spectra which are shown in EDS in the inset of this figure. These elements are formed due to wear of steel ball. Presence of O line in this spectrum originates formation of metallic oxide. However, the presence of following elements Ti, Al and N arise due to wear of TiAlN coating. In this spectrum, W, Co and C which are elemental constituents of the substrate are absent.

These observations confirm that the surface of the TiAlN coating is not severely deformed while sliding with steel ball. Therefore, the wear and friction mechanism in this sliding system is governed by the oxide scale and the nature of wear mechanism is oxidational (So et al 2002). This type of mechanism is mild and generally shows low friction coefficient. However, severe oxidation process may induce high friction coefficient due to ionic nature of bonding causing adhesion and friction.
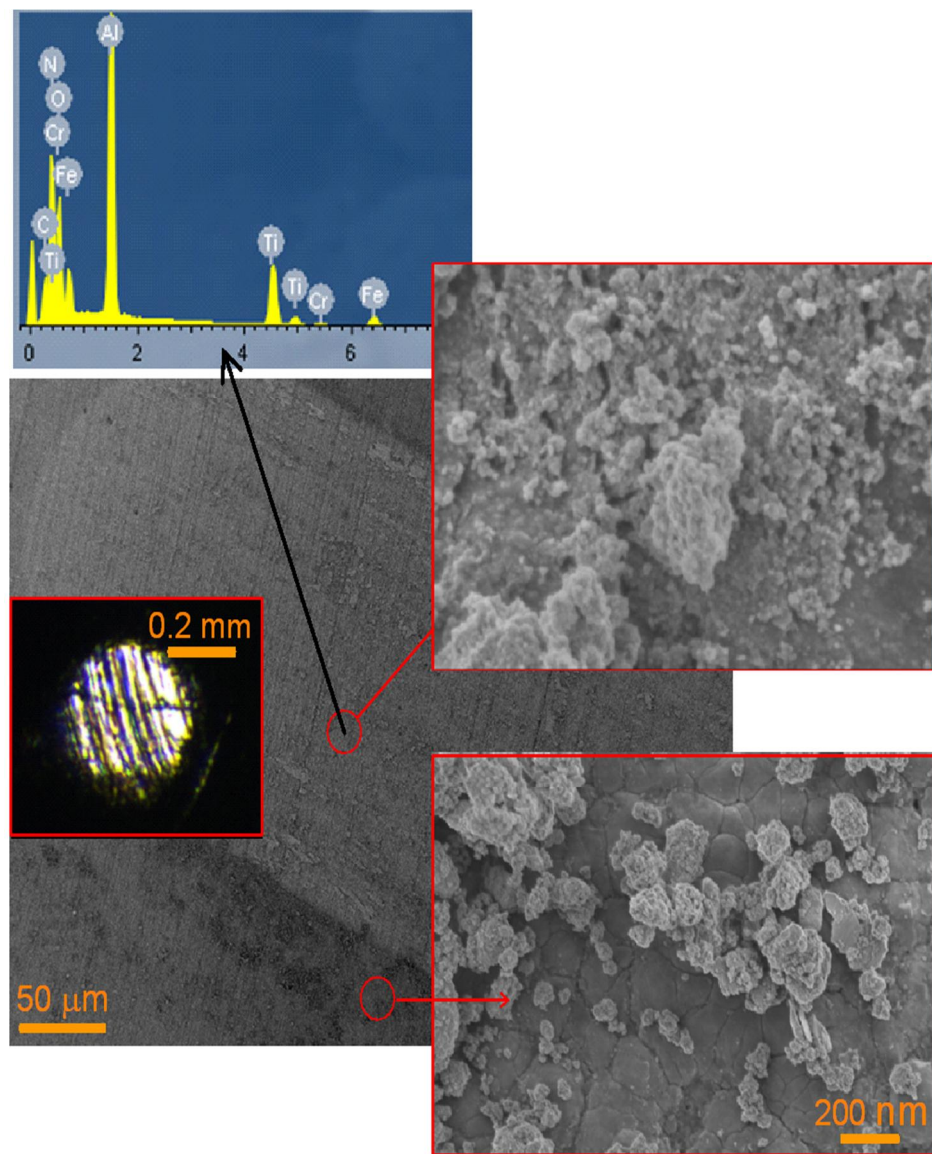
Figure 3.6   Deformation behavior of wear track in case of TiAlN/steel ball.

In contrast, friction coefficient in TiAlN/SiC sliding system is stable and it yields a value as low as ~0.17 as given in Figure 3.3(b). Such a low friction coefficient is associated with the formation of narrow wear track as compared to wider wear mark formed in the pairs of TiAlN/steel sliding system as shown in Figure 3.6. The dimension of wear scar on the ball is also small. Such characteristic of wear and friction is associated to the deformation mechanism of TiAlN film. This is shown in Figure 3.7.
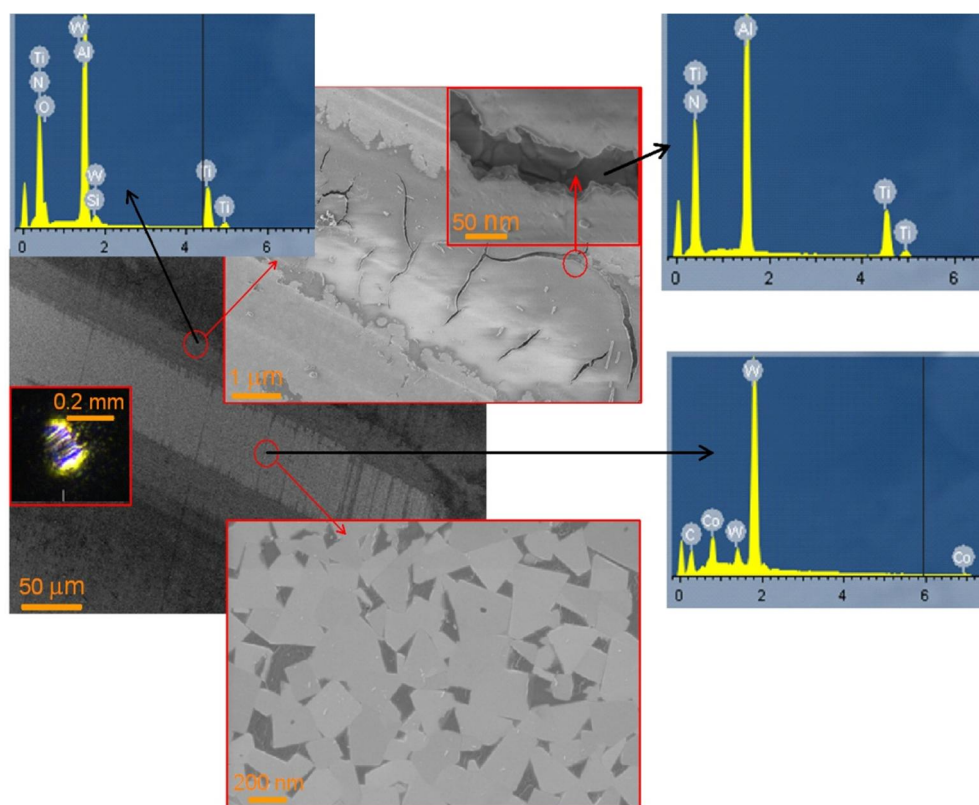
Figure 3.7   **Deformation behavior of wear track in case of TiAlN/SiC ball.**

In the low magnified SEM image, two different colors of the wear track are observed. The edges of the wear track are grayish-darker in color while central region of the track is brighter. Further, high magnified image of edge of wear track shows presence of oxide scales. Formation of this scale in particular region is evident from EDS results which shows presence of Si and intense peak of O lines. The growth of such oxide scales acts as protective layer and restrict to develop deeper profile as shown in Figure 3.5(b). In this profile, both the edges of the wear track have low penetration depth compared to the central region. This is marked in the arrow in Figure 3.5(b). Formation of such oxide scale in the edge of wear track is governed by low stress which induces tribochemical reaction and mechanical stability. In this oxide scale, the microscopic cracks within the scales are clearly observed and it is shown in the inset of Figure 3.7. The typical thickness and separation length of this

crack is 20-40 nm and 30–50 nm, respectively. Generally, the dimension of the crack depends on the compressive stress and thickness of the oxide layer. Within this crack, the TiAlN grains are clearly visible. To confirm this, the EDS was carried out in the cracked region which shows presence of elemental constitutes such as Ti, Al and N. This clearly confirms that edge of the wear track does not deform severely and the coating is constituted by TiAlN grains. In contrast, in the central region of wear track (brighter one), the deformed grains in the form of plates are observed. These plates- like morphology of the grains are identical to the grains of WC-12Co substrate as shown in Figure 3.1(b). It is well observed by EDS which shows presence of typical elements, W, Co, and C. The stress distribution in this central region is high when harder ball was used which causes high wear loss of TiAlN coatings and ultimately the ball penetrates the substrate. This clearly indicates that WC-12Co grains are plastically deformed due to high stress exhibited by the interaction of harder sliding pairs and absence of oxide layer. Moreover, most of the deformed grains are welded due to severe plastic deformation.

In this particular system, primarily the friction mechanism is governed by the formation of lubricious oxide scales on the edge of the wear track due to reduced stress (So et al 2002). Secondly, plastic deformation of the grains is exhibited due to high stress in the middle of the wear track. The role of surface films is a direct result of frictional contact and hence called tribofilms (Godet 1984). This still remains a topic of debate, largely because of the fact that the structure of such films is not fully understood, but is known to vary from film to film. The tribofilm is most likely a compositional mixture of the two base materials and other oxidation products caused by friction heating. A thin tribofilm is believed to be associated with low wear rate. It also mechanistically relate to the low friction coefficient.

In the sliding pair of TiAlN/Al$_2$O$_3$, the wider wear track is shown in the low magnified image (Figure 3.8).
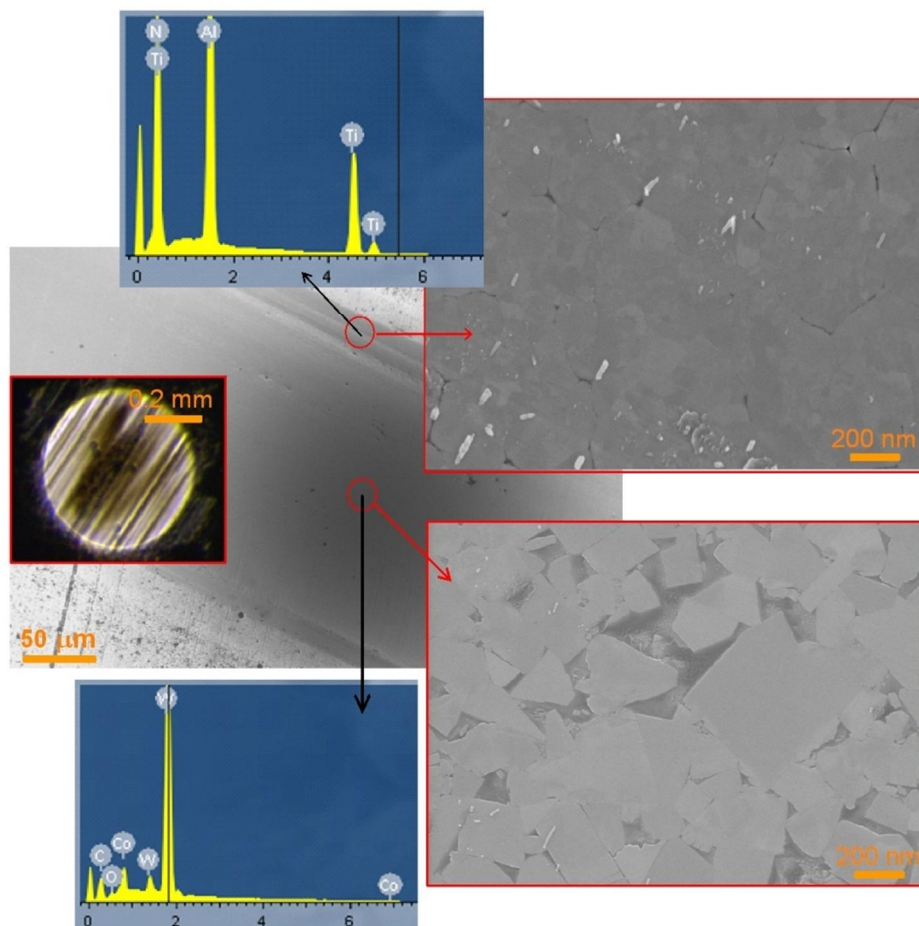
Figure 3.8   Deformation behavior of wear track in case of TiAlN/Al$_2$O$_3$ ball.

Similarly, the dimension of wear scar on the Al$_2$O$_3$ ball is also large. This is wider compared to wear track formed in case of TiAlN/steel sliding pair. This can be understood by deformation mechanism across the wear track. It shows that TiAlN grains deformed plastically on the edge of the wear track where contact stress is less. To confirm that the edge of the wear track is constituted by TiAlN, the EDS analysis was carried out which shows the presence of elements such as Ti, Al and N. However, pure plastic deformation of the WC-12Co grains is also observed in the central region of

the wear track where high stress is exhibited which results in high wear loss. It is clearly shown in EDS by the presence of elements such as W, C and Co. Low intensity peak of O line is also observed which may be due to the adsorption of atmospheric oxygen. This is the reason why ball penetrates the WC-12Co substrate in the central region of the track. The oxide scales are absent in the wear track as well as on the edge of the track. Whole area of the wear track is found to be plastically deformed. A typically deformed edge and central region of the wear track are shown in the magnified SEM images. The nature of deformation is similar in both the locations where significant plastic deformation is observed. Similar kind of deformation is observed in the central region of wear track using sliding pair of TiAlN/SiC (Figure 3.7). Sharp grain boundaries which was observed on the virgin surface of TiAlN film is found to be absent after the onset of plastic deformation. In this system, the wear mechanism and friction are governed by plastic deformation.

3.4.2   Raman Spectroscopy of Wear Tracks

To understand the tribo- chemical reaction and chemical behavior, the micro Raman spectra was obtained from the different locations of wear tracks and compared with TiAlN coating surface and WC-12Co substrate. In this respect, Raman spectra shows the typical feature of TiAlN coating as presented in curve (a) of Figure 3.9. It consists of two broad- band, centered at 268 and 644 cm^{-1}. However, curve (b) shows a broad- band around 970 cm^{-1} which is typical feature of WC. In this curve, other bands appear at 1336 and 1588 cm^{-1} which is typical of amorphous carbon (Ferrari and Robertson 2000, Ferrari and Robertson 2001). Such carbon, constituted of chemical impurities in the form of precipitates present in the grain boundary of WC. Narrow peak around 1448 cm^{-1} corresponds to C=C stretching vibrational mode (Kumar et al 2012).
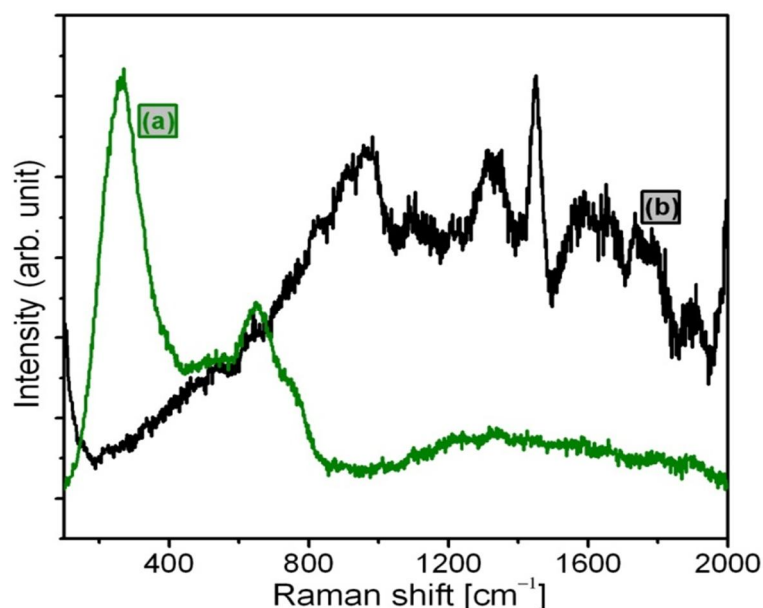
Figure 3.9   **Raman spectra of (a) coating surface and (b) WC-12Co substrate**

In the sliding system of TiAlN/steel, no clear distinction between central region of wear track and edge could be observed in the optical image during the Raman spectroscopy experiment. This is shown in Figure 3.10. However, darker and brighter regions were observed and from these locations, the Raman spectra were obtained. Brighter region corresponds to the curve (a) which is obtained from the spot (a) as shown in optical image (Figure 3.10). In this spectrum, various peaks are observed. These are centered at 218 and 281 cm^{-1} belongs to Fe_2O_3 oxide scales (Barshilia and Rajam 2005). In addition, peak at 402 cm^{-1} is typical for Fe_3O_4. Moreover, amorphous carbon related peaks are also observed at 1307 and 1585 cm^{-1} (Kumar et al 2012). Here, the optical transition mode of TiAlN occur around 656 cm^{-1}. In contrast, in darker region [spot (b)], the peak characteristic belongs to the TiAlN coating. In addition, amorphous carbon peaks at 1378 and 1565 cm^{-1} were detected. This indicates that wear track is mostly covered by oxide scale due to tribochemical reaction of steel ball with H_2O molecules. Amorphous carbon originates from steel ball which contains 0.95% C as alloy

constituents. From these results, it is clearly observed that deformation of TiAlN coating is insignificant while wear loss from the steel ball is significant.
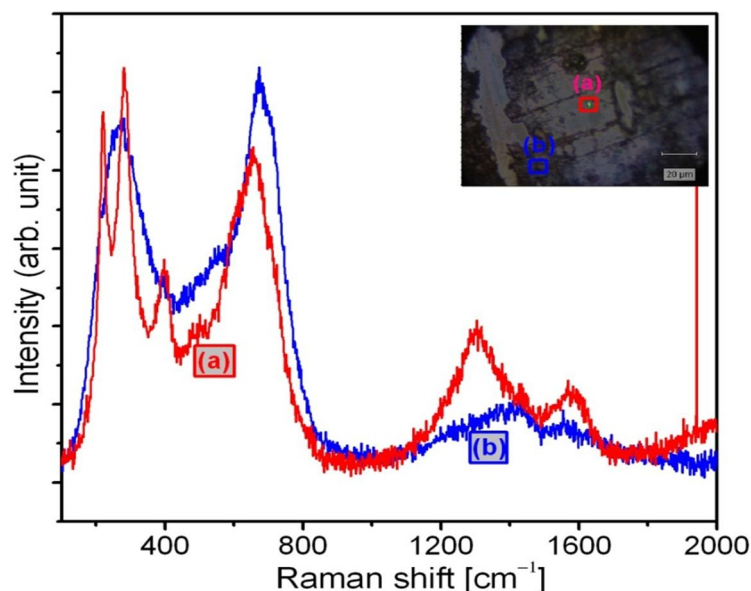
Figure 3.10 Raman spectra of wear track formed in sliding system TiAlN/Steel (a) brighter and (b) darker location of the wear track

In the sliding system of TiAlN/SiC, the plastically deformed region shows typical feature of WC band in spectra (Figure 3.11) obtained from the spot (a) and shown in optical image. However, in the edge of the wear track, the coating is present which is covered by oxide scales. This shows characteristic feature of Raman spectra corresponding to TiAlN. This region belongs to edge of the wear track (Figure 3.7), where oxide scales with cracks are shown. This oxide scale is also clearly shown in Figure 3.7. In the Raman spectra, the oxide peaks are not observed because of thin layer (20–30 nm) of this scale. Therefore, the Raman light penetrates below the oxide scales where TiAlN grains are present. Through the cracks, these grains are clearly visible in the corresponding SEM image (Figure 3.7).
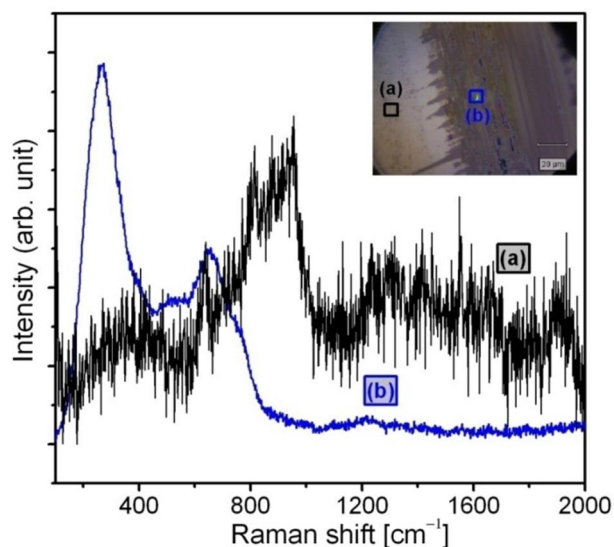
Figure 3.11 Raman spectra of wear track formed in sliding system TiAlN/SiC (a) centre of the track (b) inner edge of the wear track

When the tribology test is carried out in TiAlN/Al_2O_3 system, significantly deformed region shows weak features of TiAlN peak around 265 and 642 cm^{-1} (Spengler et al 1978, Chen et al 2011). This is given in curve Figure 3.12 which is obtained from the spot (a) of wear track as shown in the corresponding image. In addition, in this spectrum, a weak band appears around 856 cm^{-1} which represents TiAlN peak (Saunders et al 2009). The shift of this band is ascribed to change in optical phonon frequency. In contrast, strong intensity of TiAlN is obtained from the inner and outer edges of the deformed wear track as shown in curves (b) and (c), respectively. This is marked as spot (b) and (c) in the optical image.

From this analysis, it is clearly shown that the wear loss from the centre of the wear track is significant and TiAlN coating is absent. However, in the edge of wear track, where contact stress during the sliding is less, the TiAlN features persist. This is well corroborated with the SEM image shown in Figure 3.8. This shows deformed grains of TiAlN in the edge of wear track. However, in the centre of wear track, the WC plates like deformed particle are visible.
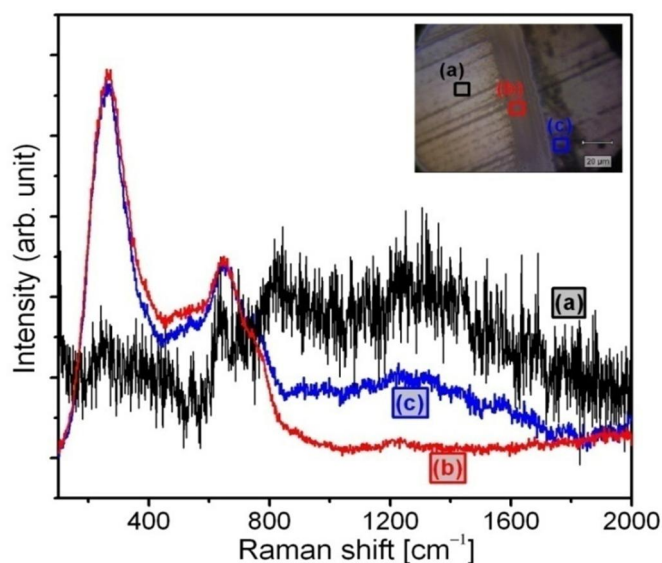
Figure 3.12   Raman spectra of wear track formed in sliding system TiAlN/Al$_2$O$_3$ (a) centre of the track (b) inner edge and (c) outer edge of the wear track

3.4.3   Tribochemistry

Tribofilm formation is exhibited by interfacial sliding of two surfaces. The physical and chemical nature of this film depends on several factors such as mating bodies, their morphology, surface roughness, microstructure, crystal structure, chemical composition and test conditions. Chemical nature of tribofilms is one of the basic aspects that influence the friction coefficient due to distinct chemical interaction and bonding. The chemical interaction is governed by dangling bonds and its passivation which largely control the friction behavior. These dangling bonds are covalent and ionic in nature which chemically interlocks the sliding interfaces causing high friction coefficient. Normally, the dangling bonds on the sliding surfaces does not chemically passivate if the oxide scales are absent. Formation of such oxides are absent in the sliding pair of TiAlN/Al$_2$O$_3$. The absence of oxide scales is evident from SEM and Raman spectroscopy. This fact is explained by high oxidation resistance and strong ionic character of Al$_2$O$_3$ ball. However, oxidation resistance of SiC is weaker compared to Al$_2$O$_3$ which

form various types of silicon oxides. These oxide scales are originating form tribochemically induced reactions with moist air which contains large amount of water molecules. Formation of such oxide scales passivate the dangling bonds of sliding interface, hence friction coefficient is less. Formation of oxide scale is governed by the following chemical reactions (Liu et al 2008) given in Equations (3.2), (3.3) and (3.4)

$$SiO_2 + 2H_2O \rightarrow SiOH_4 \qquad (3.2)$$

$$SiO_2 + H_2O \rightarrow SiO(OH)_2 \qquad (3.3)$$

$$SiO_2 + 1/2H_2O \rightarrow 1/4 O_2 + SiO(OH) \qquad (3.4)$$

Formation of SiO_2 occurs due to inward diffusion, so that oxygen is transported through the silica scale. Molecular oxygen is the primary medium for transport of oxygen during formation of SiO_2. Atmospheric molecular water is the dominant species resulting in an increase in the oxidation rate. In case of TiAlN/steel pair, the oxidational wear is severe due to low oxidation resistance of steel. The reason of low oxidation resistance is caused by weak metallic bonding and low electronegativity of steel ball. In contrast, oxygen is a good electron acceptor. This leads to formation of various metallic oxides reacting with atmospheric H_2O molecules during the tribology process. The H_2O has a large dipole moment and lone pair electrons and therefore, it is a good electron donor. Adsorption occurs by acid/base interaction process occurring with metal ions. Non-dissociative molecular adsorption also occurs and forms ionic metal oxides. Formation of metallic oxides compensates the dangling bonds, hence low friction coefficient results. The Fe_2O_3 and Fe_3O_4 form due to the following reactions. These are given in Equations (3.5) and (3.6).

$$2Fe^{3+} + 6e^- + 3/2O_2 \rightarrow Fe_2O_3 \qquad (3.5)$$

$$2Fe^{3+} + Fe^{2+} + 4O^{2-} \rightarrow Fe_3O_4 \qquad (3.6)$$

When these oxides scales react with H_2 molecules it forms following substance (Liu et al 2008) expressed in Equation (3.7).

$$3Fe_2O_3 + H_2 = 2Fe_3O_4 + H_2O \qquad (3.7)$$

Further growth of the oxide scale depends on a large extent on ensuing transport processes, where the so-called H_2/H_2O bridges provide the transport mechanism. The above mentioned chemical reaction and self-generated oxides scales act as tribo- lubricants.

3.5   CONCLUSION

Tribological properties of TiAlN coating was studied while sliding against various counterbodies such as 100Cr6 steel, SiC and Al_2O_3. Friction coefficient of TiAlN/Al_2O_3 sliding pair was significantly high with the values in the range 0.6–0.9. In this system, wear rate of Al_2O_3 ball and TiAlN coating was in the same order 5.7×10^{-6} and 2.3×10^{-6} mm^3/Nm, respectively. For this sliding pair, the wear mechanism was governed by plastic deformation. However, the friction coefficient was less than 0.2 in sliding pair of TiAlN/steel. The wear rate of SiC ball and TiAlN coating was also in the same order 4.3×10^{-7} and 1.7×10^{-7} mm^3/Nm, respectively. Improved tribological properties in this system are governed by the formation of lubricious oxide layer. In the sliding system of TiAlN/steel ball, the value of friction coefficient is ~0.3. The wear arte of TiAlN coating sliding with steel ball is significantly less 4.0×10^{-10} mm^3/Nm. However, the wear rate of ball is high 2.8×10^{-4} mm^3/Nm. In this sliding pair, the mechanism of wear is oxidational.

CHAPTER 4

WEAR MECHANISM OF CrN/NbN SUPERLATTICE COATING SLIDING AGAINST Al₂O₃, SiC AND STEEL BALLS

4.1 INTRODUCTION

Hard coatings deposited by PVD are suitable for improving wear resistance of components in several engineering applications. In this respect, nitrides of transition metals such as CrN, TiN and NbN have been studied extensively and these are well established in industrial applications (Chang et al 2011, Zhang et al 2007, Hovsepian et al 2005, Gwang et al 2003). Among them, CrN coating is one of the widely used in cutting tools, die and mould, mechanical components and artificial joints. Such coating increases the service life due to excellent oxidation resistance, corrosion resistance, low friction coefficient and high wear resistance (Zhang et al 2007, Gwang et al 2003, Lee et al 2006, Chang and Wang 2004, Cheng et al 2011, Hones et al 1997, Ehiasarian et al 2004, Chang et al 2004).

Further, it is possible to deposit such species in a periodic way to achieve a nanoscale multilayer structure with improved mechanical and tribological properties as compared to single layer monolithic coatings. Moreover, the deposition of multilayer coatings by magnetron sputtering is useful in several applications (Hovsepian et al 2005, Gwang et al 2003). High

coating hardness has been observed for TiN/VN (Helmersson et al 1987) and TiN/NbN (Chu et al 1993, Larsson et al 1996) multilayer coatings. Both improved corrosion resistance and decreased erosive and abrasive wear rates due to multilayer structures have also been reported for CrN/NbN (Tomlinson et al 1999) and TiN/CrN systems (Nordin et al 1999). The properties of these coatings are dependent on the period of the individual layers in the structure. In this coating, the layer thickness is less enough such that the coatings form a superlattice structure. In this context CrN/NbN nano-scale multilyered coatings (Cameron et al 2001) have performed particularly well in corrosion resistant applications because of the use of chemically stable metals like Nb and Cr stacked a nano-scale multilayer architecture.

High hardness and wear resistance is derived due to the superlattice effect, i.e. the suppression of dislocations, grain refinement, coherency strain hardening, dislocation line energy effects and interfacial cracking. The detrimental effects of macroparticles, solidifying from melt cathode droplets poorly react with N-plasma on the substrate. This results in local loss of coating adhesion, surface roughening and grain coarsening. In addition it creates non-uniform N and phase distribution within the particle, and formation of shrinkage porosity due to droplet self-repulsion mechanism.

In this chapter, tribological properties of CrN/NbN superlattice coating sliding against 100Cr6 steel, Al_2O_3 and SiC spherical counterbodies were investigated. Deformation behavior and chemical nature of corresponding wear tracks were investigated by SEM and micro Raman spectroscopy, respectively. The correlation of friction and wear mechanism is proposed with respect to microstructure and oxidation resistance of sliding ball counterbodies.

4.2   EXPERIMENTAL AND CHARACTERIZATION TECHNIQUES

The ~2.7 µm thick coating of CrN/NbN superlattice was deposited by PVD technique using magnetron sputtering at a deposition temperature of 450^oC. The coatings have been deposited in a cylindrical closed field unbalanced magnetron system using two seperate targets. The coating structure comprises an initial Cr adhesion layer, a CrN base layer and then a CrN/NbN superlattice layer. One target has been used for Cr sputtering and the opposing target used for Nb sputtering. The film stoichiometry has been controlled by an Optical Emission Monitor (OEM) feedback system which controls the reactive gas flow rate to maintain a particular intensity from the Cr emission line in front of the Cr target. The Cr-Nb flux ratio has been fixed by setting the ratio of the Cr to Nb target currents taking into account their relative sputter yields. The substrates have been mounted on a one-axis rotation system in one of two positions; at radii of 8.5 (S position) or 17 cm (B position) equivalent to 17.5 and 8 cm, respectively from the targets at their nearest point. The substrate was biased using a pulsed DC power supply with a frequency of 250 kHz and a pulse width of 1200 ns. The effect of the substrate to target distance is to vary the metal to reactive gas and also the ratio of the ion to atom arrival rates.

Nanoindentation measurements were carried out with Berkovich diamond indenter at a constant loading/unloading rate of 5 mN/min. The tests were conducted at a peak load of 15 mN. The formalism of Oliver and Phar (1992) was used to calculate the elastic modulus and hardness of all the specimens. Linear reciprocating mode of ball on the disk micro- tribometer (CSM Instruments, Switzerland) was used to carry out the tribological tests.

In these measurements, the normal load and sliding speed were constant 5 N and 4 cm/s, respectively. Three different kinds of ball counterbodies such as 100Cr6 steel, SiC and Al_2O_3 were used for sliding against CrN/NbN superlattice coating. The diameters of these balls was 6 mm. Surface roughnesses of the balls were 0.04, 0.02, and 0.03 µm for 100Cr6 steel, SiC and Al_2O_3, respectively. Tribological experiments were conducted in ambient atmospheric condition at room temperature where the relative humidity was 75%±2. Insitu wear track depth was measured by a LVDT sensor coupled to the micro- tribometer.

In addition, wear profile after the test was measured by a Dektak 6M–stylus profiler using 5 mg load with a scanning speed of 30 µm/s. In this method, tip of diamond stylus with a radius of curvature of 12.5 µm was scanned across the wear track. On each sample, wear profile was measured 3 times and it was found to be reproducible. The surface morphology and microstructure of the coatings were analyzed using a FESEM (CARL ZEISS SUPRA 55). HRXRD measurements were carried out to obtain the structural information of coating. The incident angle of the X-ray was 0.8^o. The atomic concentrations, chemical and bonding states in CrN/NbN superlattice film were investigated by XPS (PHI 5802 system) with a monochromatic Al *Kα* X-ray source.

4.2.1 Morphology and Microstructure of the Coating

The morphology of the honeycomb like structure of CrN/NbN superlattice is shown in Figure 4.1. Droplets and grooves are clearly seen in low magnified image of SEM in Figure 4.2.
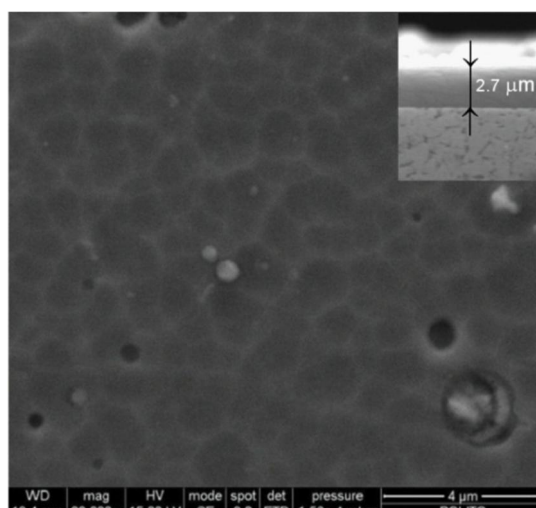
Figure 4.1   Surface morphology and cross section of CrN/NbN superlattice coating
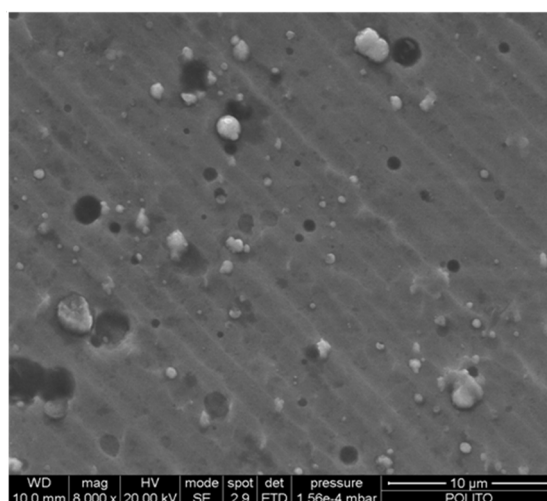
Figure 4.2 Low magnified image clearly shows droplet and grooves

The presence of deeper craters and larger droplets is responsible for the high roughness which is typical of this arc-deposited CrN/NbN supperlattice (Lewis et al 2006, Martini and Ceschini 2011). Thickness of the coating is 2.7 µm as shown in the cross section (Figure 4.1). It is useful to determine the superlattice structure by observing the diffraction peak at low angles in XRD. The superlattice spacing is a function of the deposition rate which depends mainly on the target current, target to substrate distance and

on the rotation speed of the substrate arrangement (Cameron et al 2001). It can be seen that there is a wide variation in the intensity of the diffraction peak and in many cases no peak could be observed indicating that there was no superlattice structure. In some cases satellite peaks could also be observed around the high angle diffraction peaks. The intensity of the diffraction peak can be taken as an approximate measure of the abruptness of the change in composition between the chromium nitride and niobium nitride layers in the structure. The intensity of this peak was plotted as a function of the superlattice period. The plotted data are taken from a wide range of deposition conditions such as bias, rotation speed, intensity of the OEM setting and target current. It can be seen that irrespective of the deposition parameters the intensity of the peak is a linear function of the superlattice period and that once the expected period reaches <10 Å there in no diffraction peak observed at all.

Further, in the present chapter the structure of the coating was determined from XRD using a Pearson fitting. Lattice parameters, a_o, were described by Cohen-Wagner function (cos θ cot θ) in order to eliminate symmetric errors. An extrapolation to $\cos\theta \cot\theta = 0$ gives the lattice parameter a_o. The superlattice period Δ, in the low angle region was measured directly from the standard Bragg equation: $\Delta = (n\lambda/2d \sin\theta)$, where θ is the Bragg angle, λ is X- ray wavelength and n is order of the wavelength. The XRD pattern from the films was characteristic of a face centered cubic structure with lattice parameters intermediate between CrN and NbN as shown in Figure 4.3. The main peak of cubic CrN is observed at 61.7^o 2θ with the orientation of (220) that corresponds to Cr_2N (NaCl-type, $a_o=0.414$ nm) (Hovsepian et al 2005, Cameron et al 2001).
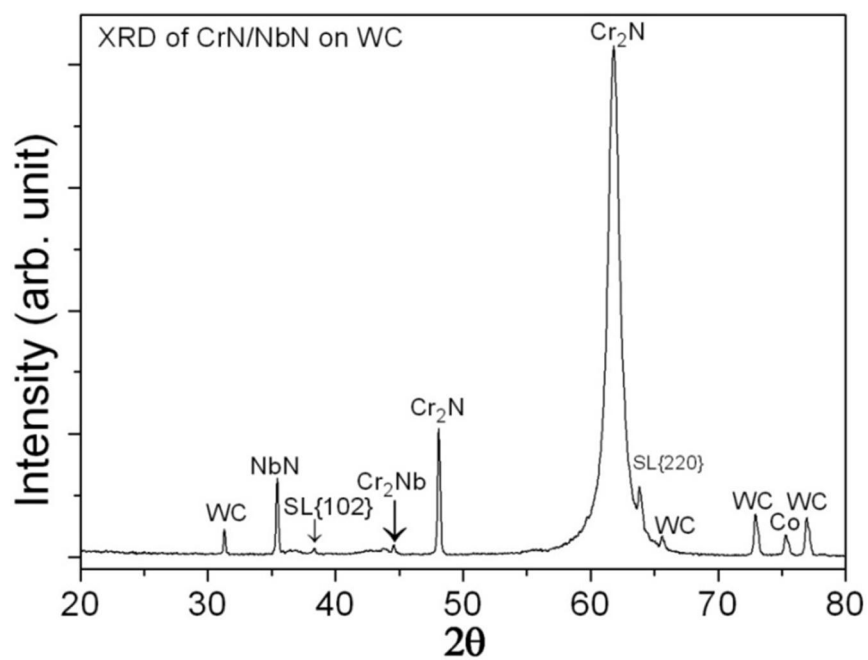
Figure 4.3 XRD of CrN/NbN superlattice coating
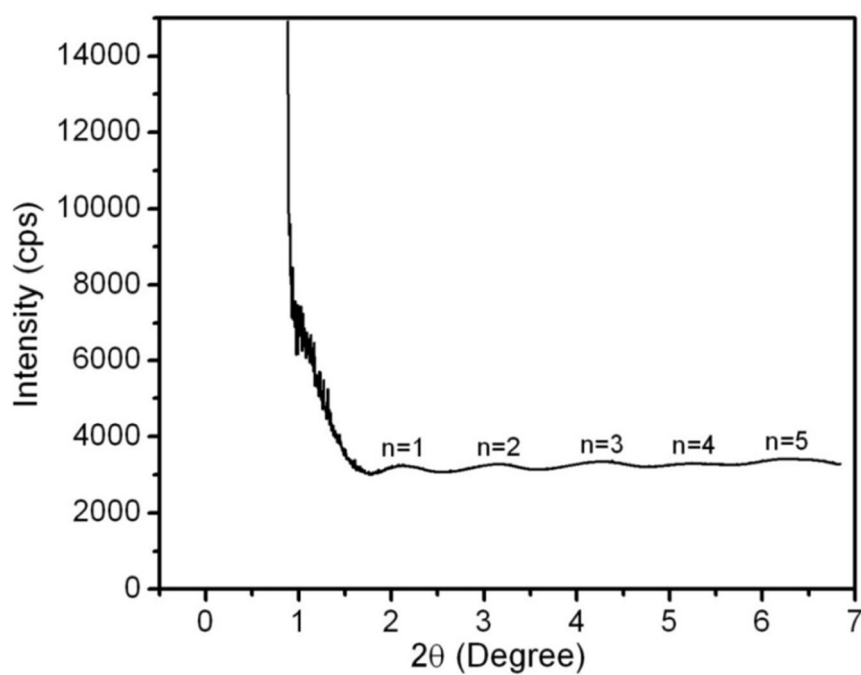
Figure 4.4   Low angle XRD spectrum of the CrN/NbN coating shows superlattice period

Moreover, NbN and Cr$_2$Nb peaks are observed at 35.4 and 48.1^o 2θ angles. In addition, WC and Co peaks are also present. The presences of these peaks are due to the substrate. Low angle XRD (LA XRD) spectrum of the CrN/NbN coating is shown in Figure 4.4. In this case, triggering time is low enough to obtain nanometric layers.

4.2.2   XPS analysis of CrN/NbN coating

For the detail chemical analysis, the XPS measurements on the CrN/NbN coating was carried out and it is shown in Figure 4.5.
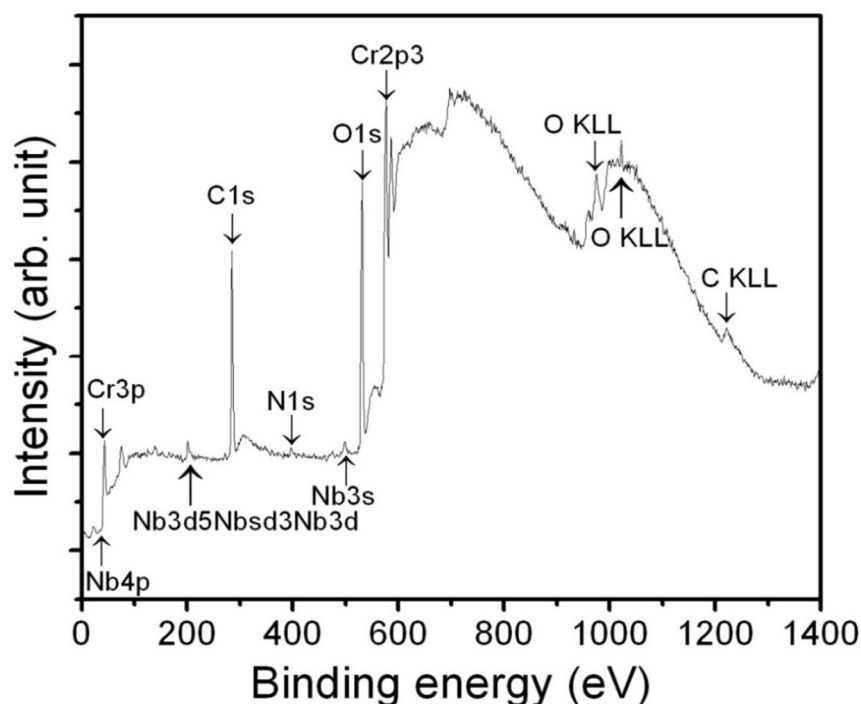
Figure 4.5 XPS of CrN/NbN superlattice coating

The core level photoelectron spectra of Cr2p, C1s and N1s were fitted by Gaussian and Lorentzian peaks. Note that the spin–orbit splitting for Cr2p is 9.2 eV and the fitting was performed only using the Cr2p 3/2 peak. In these fittings, a Shirley type background- subtraction was used (Ermolieff et al 1988). The surface chemical and phase composition derived from available

binding energies of the respective peaks are listed in Table 4.1. In addition, their FWHM values are included. The electron binding energy of Cr2p 3/2 peak shows a broad peak around 575.1 eV that is high for metallic 574 eV. This peak consists of four components that correspond to Cr metal at 574.1 eV, Cr (nitride) at 576.2 eV and Cr (oxynitride) at 583.5 eV and 577.2 eV. Further, the C1s spectra consists of three components with peaks at 284.1 eV (sp^2C-C) and carbonitrides (sp^2 C-N) at 286 eV and 288.6 eV. The N1s peak is described by three peaks of different intensities that correspond to CrN and Cr_2N centered at 396.7 eV, and 397.6 eV and sp^3C-N at 399.5 eV, respectively (Vyas et al 2008).

Table 4.1 Binding energy on the surface of CrN/NbN superlattice coating

Peak	Binding energy (eV)	Bonding state	FWHM
Cr2p	574.1	Cr (metal)	0.78
	576.2	Cr (nitride)	0.85
	583.5	Oxynitride	1.3
	577.2	Oxynitride	1.6
C1s	284.8	C-C ligand (sp^2C-C)	0.65
	286	C-N ligand (sp^2C-N)	1.2
	288.6	C-N ligand (sp^2C-N)	1.3
N1s	396.7	CrN	1.1
	397.6	CrN	0.8
	399.5	CrN (sp^3C-N)	0.95
Nb3d	200.7	Nb	0.8
	202.4	N	0.85
	206.6	O- NbN	1.2

In addition, a broad feature at 201.2 eV is observed which corresponds to the Nb3d. This peak consists of three components that correspond to Nb, N and O- NbN binding states around 200.7, 202.4 and 206.6 eV, respectively.

4.3   TRIBOLOGICAL PROPERTIES

Friction behavior of CrN/NbN coating is shown in Figure 4.6 while sliding with Al_2O_3, steel and SiC balls. The value of friction coefficient is lowest ~0.01 when coating slides against Al_2O_3 ball as shown in Figure 4.6(a). However, this value is higher ~0.17 and 0.3 in Figure 4.6(b) and Figure 4.6(c), respectively, when it slides against steel and SiC balls, respectively. The corresponding penetration depth, measured insitu is shown in Figure 4.7. It is found to increase with sliding distance. Further, the magnitude of penetration depth is more or less similar (~ 2 µm) when coating slides against all the three balls. Initially, the wear loss is high which shows rapid increase in penetration depth i.e., declining behavior of curves is shown. However, after lapse of few hundred sliding distances, this curve is all most saturated (reduced declining is observed). Initially, the increase in penetration depth is caused due to two reasons.
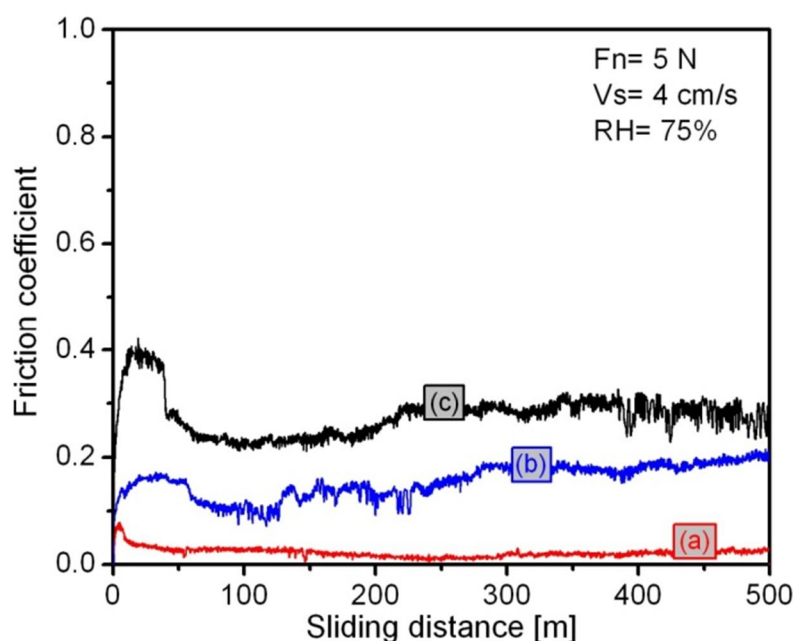
Figure 4.6   Friction coefficient of CrN/NbN coating sliding against (a) Al_2O_3 (b) SiC and (c) steel ball
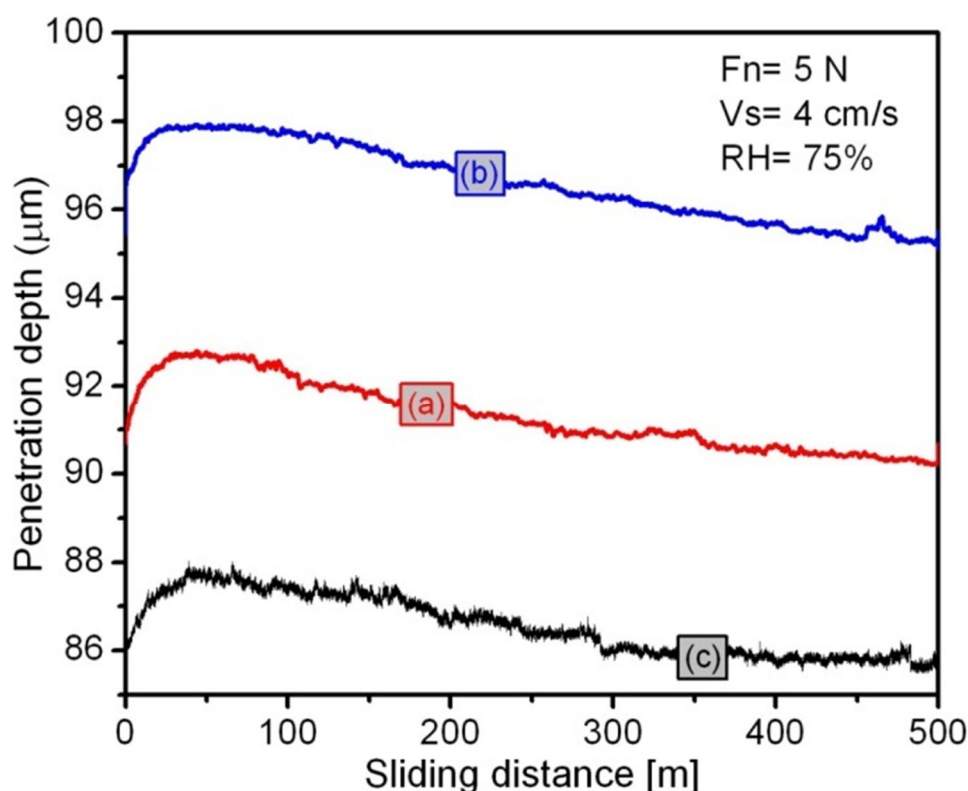
Figure 4.7 **Insitu penetration depth of CrN/NbN coating sliding against (a) Al$_2$O$_3$ (b) SiC and (c) steel ball**

Firstly, during initial sliding passes, the contact stress is high due to reduced contact area of interfaces. Secondly, high wear loss is ascribed to softening of the contact interfaces which takes place during the initial sliding passes. However, the contact area of sliding interfaces continuously increases with sliding distance due to progressive wear loss. This leads to decrease in contact stress which subsequently causes declination in the penetration depth and wear loss. Secondly, the concentration of defect complexes is high across the sliding interfaces while longer sliding passes which enhances the strain hardening. The increase in strain hardening increases the resistance for deformation, hence less wear loss. Strain hardening due to defect concentration and their correlation with wear mechanism is well described by Anirban Mahato et al (2011).

4.3.1 Dimension of wear profile

In addition, wear profile is measured by a Dektek surface profiler after the tribology test and the result is shown in Figure 4.8. In this consequence, insitu wear depth measured by LVDT sensor during the tribology test is more or less agrees with the wear profile measured by Dektek after the tribo- test. The wear depth is ~ 2 µm while coating slides against steel and SiC ball. These are shown in Figure 4.8(b) and Figure 4.8(c) respectively. However, this is less in Al_2O_3 ball as shown in Figure 4.8(a). Low friction coefficient and oxidation resistance of the Al_2O_3 ball sliding against CrN/NbN coating could be primary reason for high wear resistance.
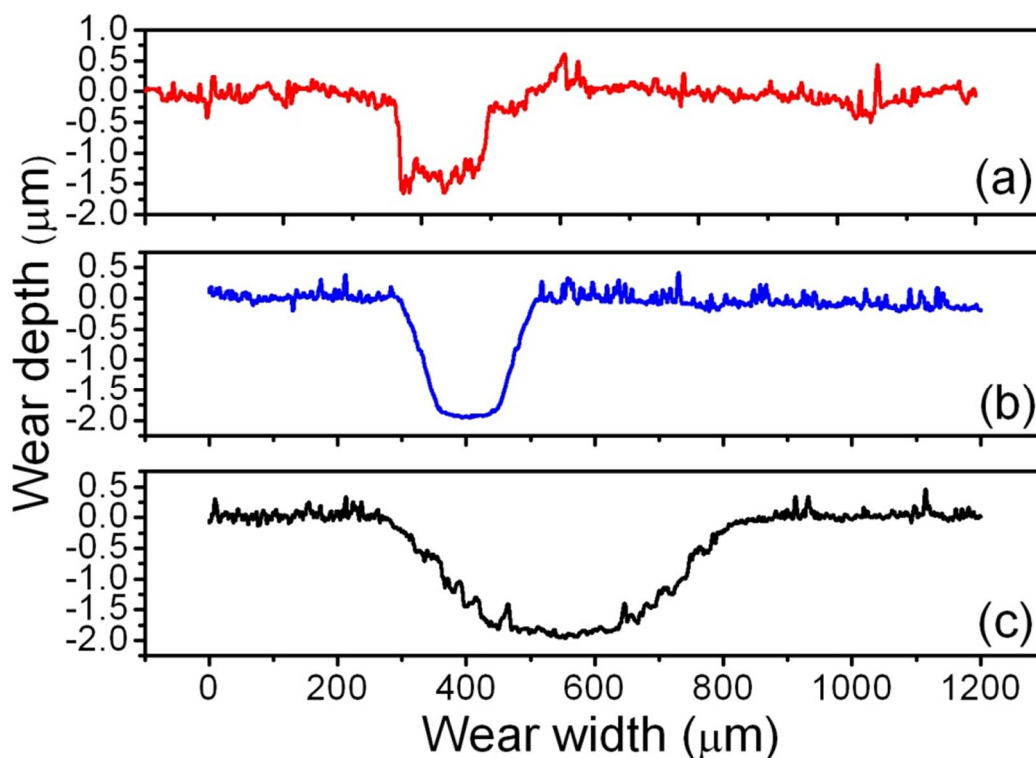
Figure 4.8 **Wear depth and width profile of CrN/NbN coating sliding against (a) Al_2O_3 (b) SiC and (c) steel ball**

Further, the wear width is narrow and features are similar when coating slides against Al_2O_3 and SiC balls. However, the wear track widens while sliding against steel ball. This behavior is explained by determining hardness and elastic modulus of balls and coating and calculating the resistance against plastic deformation. These are given in the Table 4.2. It is shown that hardness and elastic modulus of coating is 27±3 GPa and 420 GPa±23 GPa, respectively, as measured from nanoindentaion technique. Further, hardness and elastic modulus along with H^3/E^2 factor for the CrN/NbN coating and various balls were calculated and these are also given in the Table 4.2. It is shown that the resistance to plastic deformation in case of steel ball is lowest 0.00057. This causes pronounced deformation of steel ball and the ensuing contact area becomes wider. Therefore, wear track width consequently increases.

Table 4.2 Mechanical properties of CrN/NbN coating and counterbody balls

	H (GPa)	E (GPa)	H^3/E^2
CrN/NbN	24±3	398±18	0.1
Al_2O_3	26±2.3	382±32	0.12
100Cr6 steel	2.7±0.2	185±17	0.00057
SiC	22±1.8	345±28	0.09

In the view of above results, the tribological properties of CrN/NbN coating sliding with Al_2O_3, steel and SiC balls are described by two distinct aspects i.e., belonging to mechanical and chemical characteristics. In case of Al_2O_3 ball, the hardness is comparable to the hardness of CrN/NbN coating. Both the sliding interfaces exhibit near similar resistance to plastic deformation. This behavior is equally valid while CrN/NbN coating slides against SiC ball. However, friction coefficient is significantly low 0.01 and

wear resistance is high in Al_2O_3 as compared to sliding against SiC ball. Wear resistance is described by calculating the wear rate. It is calculated by considering the wear track width, depth and length from which wear volume is subsequently computed and wear rate is determined by equation (2.12). The values of friction coefficient and wear rate are given in Table 4.3. Here, such a difference in friction coefficient cannot be explained alone by hardness and H^3/E^2 factor of the sliding interface. It is necessary to consider high oxidation resistance and high surface chemical inertness of Al_2O_3 ball. Such properties cause high chemical resistance of the sliding surfaces. In order to elucidate the wear mechanism which shows low friction coefficient of CrN/NbN superlattice coating while tested with Al_2O_3 ball. The surface morphology, composition of the wear track and wear debris formed on the track test were analyzed.

Table 4.3 Friction coefficient and wear rate of CrN/NbN coating sliding against Al_2O_3, steel and SiC balls

	μ (Average)	k (mm^3/Nm)
Al_2O_3	0.01	2.6×10^{-7}
100Cr6 steel	0.17	8.2×10^{-7}
SiC	0.3	3.4×10^{-5}

4.3.2   Wear Track Morphology

It is shown that the abrasive particles of the CrN coating are present in the track. However, the abrasion of the Al_2O_3 ball was found to be negligible which confirms high abrasive and oxidation resistance of Al_2O_3 ball (Cheng et al 2011). Cheng et al (2011) also shows appreciable amount of debris, corresponding to the low wear rate of the CrN coatings sliding against Al_2O_3 balls. It is shown that the tribochemical interaction between the Al_2O_3 ball and the coating is rather limited and consequently, the wear rate of the

balls becomes negligible (Polcar et al 2007). Therefore, sliding with Al_2O_3 balls is a typical three-body abrasive interaction mode with protective wear debris accumulating at interlayer. The appearance of wear tracks clearly demonstrates a polishing wear mode that occurs in combination with plastic deformation of the coating. However, SiC ball exhibits reduced oxidation resistance and chemical inertness when compared to the Al_2O_3 ball. This leads to chemical interlocking, causing severe abrasive wear (Wang et al 2011). In case of steel ball which is much softer than CrN/NbN coating, formation of abrasive particles from the steel ball occurs. Therefore, wear mechanism becomes dominant by oxidational and abrasive (Cheng et al 2011, Mo et al 2008).

In this case, the transfer of ball material to the surface of the coating was quite significant and the coating surface becomes fully covered by a layer of oxidized ball materials (Polcar et al 2007). Wear debris are entrained in metal oxide layer on the wear track. Such debris is porous, irregular shaped and consists of nano-sized particles. In case of CrN/NbN coating sliding against Al_2O_3 ball, the plastically deformed and smooth wear track is observed as presented in Figure 4.9(a). This feature includes polished surface of wear track with grooves and fine abrasive particles. In the work of Cheng et al (2011) the wear mechanism of the low friction coefficient of CrN coatings tested with Al_2O_3 balls is also observed. The surface morphology and composition of the wear track and wear debris on the test coupons were investigated using SEM and EDS.

It is shown that the wear track on CrN coatings is much narrower than that on TiN coatings. High magnification observations show that the wear track on CrN coating surface exhibits a fine polish-like structure. However, on TiN coating surface, wear grooves parallel to the sliding direction could be clearly observed. This indicates that the wear mechanism

of CrN and TiN coatings against Al_2O_3 is abrasion wear, but CrN coatings have higher wear and abrasion resistance against Al_2O_3 ball. However, in the case of CrN/NbN coating sliding with SiC and steel balls, oxide layers on the wear track are formed as seen in Figure 4.9(b) and Figure 4.9(c), respectively.
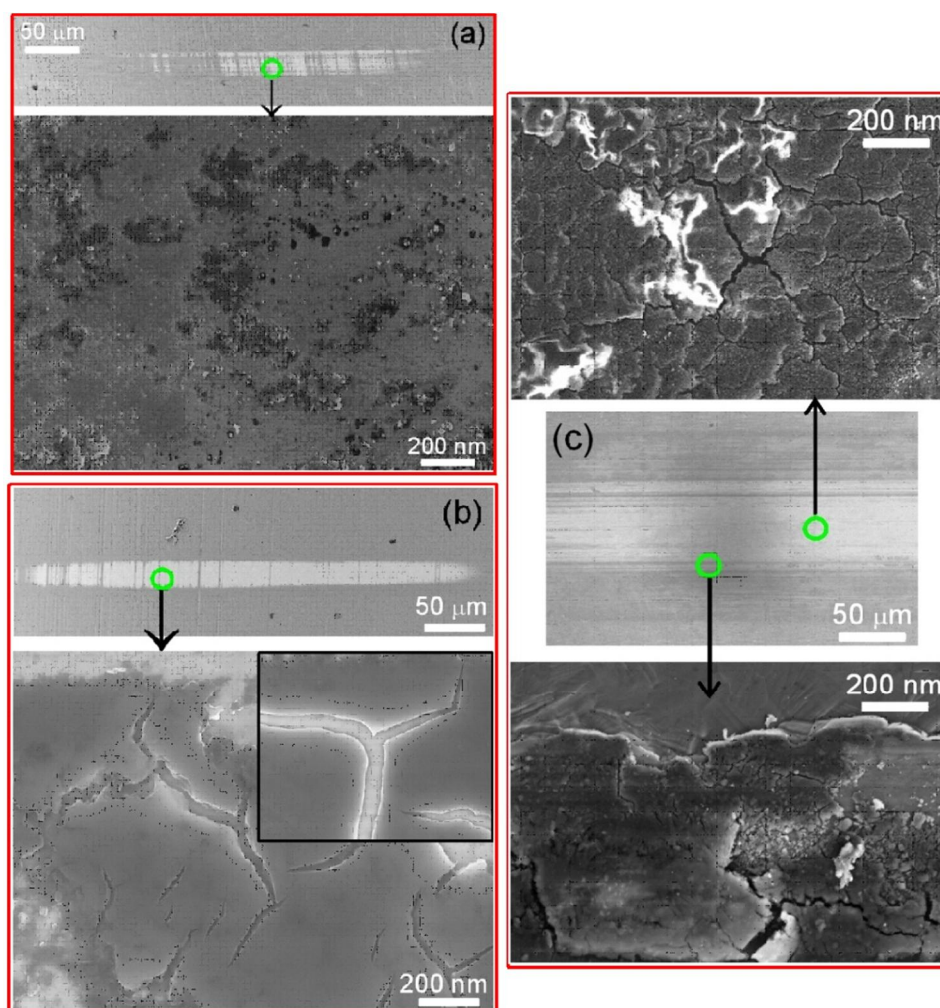
Figure 4.9 **Deformation behavior of CrN/NbN coating sliding against (a) Al_2O_3 (b) SiC and (c) steel ball**

The oxides are mostly constituted by silicon oxide and metallic oxide in SiC and steel balls, respectively. The cracks in the oxide layers are clearly visible. Prominent feature of metal oxide scale are visible when CrN/NbN coating sliding against steel ball. This kind of wear is generated due to the tribochemical reaction of metal with ambient atmosphere. Metal surface

is normally covered with a layer of oxide, which could prevent metal-to-metal contact, and thus avoiding the formation of adhesion and reducing the tendency of adhesive wear. In this respect, oxide is favourable to reduce wear rate of metallic materials. However, whether such beneficial effect can be realized is strongly dependent on the material properties and contact conditions. When the hardness of the metal underlying an oxide layer is low or when the contact load is relatively higher, the metal beneath the oxide layer will plastically deformed and asperities in the hard surface will penetrate through the thin oxide layer. This leads to the normal metal-to-metal contact.

In such case, wear by abrasion or adhesion will occur depending on the mechanical and chemical properties of the contacting metals. The beneficial effect of oxide is minimal and wear rate is generally high. On the other hand, when the underlying metal is hard enough to support the oxide film, such as on engineered hard surface, the oxidation wear is exhibited. The mechanism of oxidation wear is schematically shown in Figure 4.10.

At the beginning of a wear process, the original oxide film on the metal surface was removed when hard asperities rub across the point of the oxide layer, leaving the underlying metal uncovered. The fresh metal will quickly react with oxygen in air to form a fresh oxide layer, which will then be scraped off again by asperities in the following cycle. Such an "oxidation – scrape", or "chemical – mechanical" cycle repeats during the oxidation wear process, producing wear debris of finely powdered oxide. The worn surface is smooth and frequently covered with a layer or patches of oxide which can be visually seen. For steel, the worn surface becomes dark brown (colour of iron oxide). The morphologies of a surface worn by oxidation wear are shown in Figure 4.10.
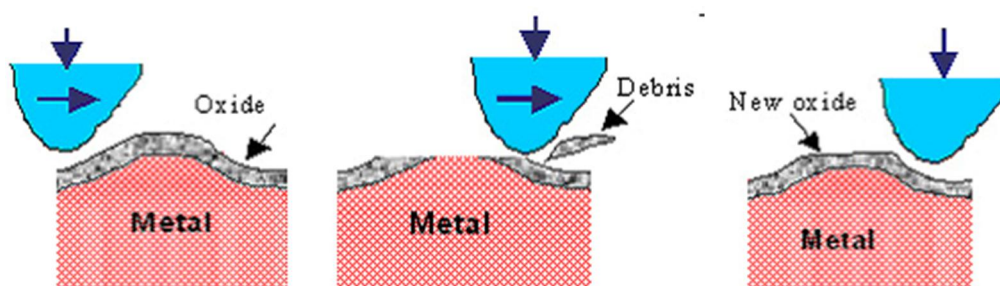
Figure 4.10 Generalized schematic of oxidation wear process

It needs to be mentioned that during sliding, the high surface temperature induced by frictional heating, and the reduced activation energy of oxide formation caused by plastic deformation, can increase the oxidation rate. Thus, rapid oxidation can be achieved, and the oxide layer can grow thicker during sliding under static conditions. This ensures the fresh metal is rapidly covered with a new layer of oxide after the original oxide film was worn away. Oxidation wear is absent in vacuum or in inert atmosphere, since re-oxidation is not possible. Oxidation wear is a mild form of wear. When the predominant wear mechanism is changed from abrasive or adhesive to oxidation wear, wear rate can be decreased by several orders of magnitude. In this study the oxidational wear mechanism is present when CrN/NbN coating sliding with SiC and steel ball.

The fact is that, engineering surface is practically never perfectly flat. The surface of a most highly polished engineering component show irregularities or asperities. When two such surfaces are brought into contact, the real contact actually occurs only at some high asperities which are a small fraction, e.g. 1/100 of the apparent contacting area. As a result, plastic deformation and intermetallic adhesion will occur, forming cold weld junctions between the contacting asperities. The strength of junction is determined by the surface structure and by the mutual solubility of two contact metals. The tendency of adhesion is the lowest for a pair of metals

with almost zero mutual solubility, but this is limited to very few metals. Most metallic materials show appreciable tendency of adhesion.
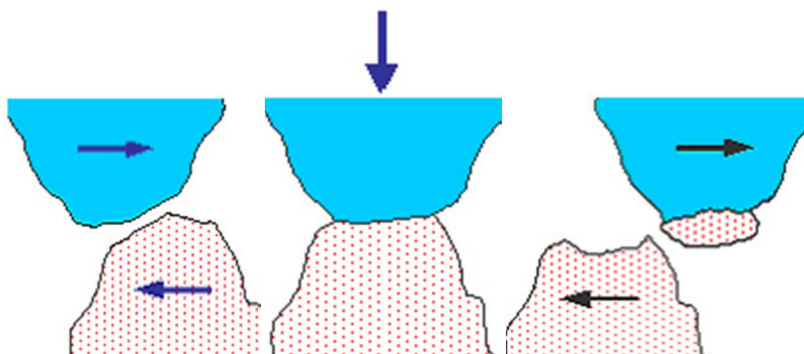
Figure 4.11 Schematic of adhesive wear which occurs by material transfer

When two contact surfaces undergo relative movement, tearing must take place either at the (cold weld) junction or inside the original materials depending on which is weaker. If the strength of the adhesion junction is relatively low, as in the case of a contact pairs with low mutual solubility or metallic surfaces separated by oxide film, tearing will take place at the junction and material loss during wear will be minimal. However, when tearing occurs inside the softer material, a fragment of the softer material will be dragged away and adhering to the harder body, as a schematic shown in Figure 4.11. This process is known as material transfer as discussed in detail in chapter 3.

The transferred fragment is plastically deformed during continued action of sliding so that the transferred materials frequently have a plate-like morphology. Multi-material transfer and plastic deformation of the transferred material result in a layered surface morphology on the counterface. This mechanism is present in all the sliding counterbodies such as Al_2O_3, SiC and steel ball sliding against CrN/NbN coating as shown in Figure 4.9(a-c). The next stage is detachment of the transferred layer, probably when the bond

between the layer and the underlying material has been locally weakened by cyclic loading.

4.3.3   Raman Analysis of the Wear Tracks

The friction values were strongly correlated with the coating type and the counterface composition. The friction was higher for an Al_2O_3 counterface compared to a WC counterface for both coatings. Similarly, the TiAlN/VN has lower friction for both counterfaces compared to the CrN/NbN (Zhou et al 2007). Thus, the interaction between the two materials clearly have a strong effect on friction, and therefore the nature of the tribofilm formed and the structure of the wear debris is the key to understand the friction behavior. It has been shown that the friction and wear observed between hard coatings and the counterface depends strongly on the formation of tribofilm. Friction invariable starts at low values, but then tends to increase, despite the wear process giving a smoothing of the surface. The change in friction has been correlated with the development of a tribofilm that consists of components of both surfaces. Where adhesion is strong, extensive transfer from the counterface tends to occur resulting in a tribofilm that is usually an oxide based on components from both surfaces. Zhou et al (2007) observed Fe_3O_4 and Al_2TiO_5 in a thin (~100 nm) tribofilm on the surface of a TiAlN/CrN multilayer worn against steel, which tended to promote high friction and was shown to eventually lead to failure of the coating. In contrast, the TiAlN/VN studied. Frictional heating and adhesion with the counterface has been shown to develop due to oxidation that can substantially reduce friction.

In order to elucidate the associated chemical nature of wear track and the consequent oxidation resistance, the Raman spectra were obtained from the corresponding wear tracks and virgin surface of the CrN/NbN

coating. These are shown in Figure 4.12. There are several weak spectral features at 298, 480, 797, 894, 959, 1405 and 1555 cm^{-1} as shown in Figure 4.12 (virgin surface of CrN/NbN superlattice coating). The peaks at 298 and 797 cm^{-1} belong to Fe_2O_3 and Cr_2O_3 phases (Quinn 1971, Quinn 2002, Quinn 1985, Wei and Stott 1989, Kumar et al 2012). Peaks at 480, 894, 959 cm^{-1} belong to $CrNbO_3$ (Barshilia et al 2002, Fontalvo et al 2007). Further, Raman shift at 1405 and 1555 cm^{-1} designated as formation of amorphous carbon which occurs in the form of impurities (Ferrari and Robertson 2001). The intensities of these peaks are rather weak. Further, wear track formed during sliding against Al_2O_3 ball shows weak Raman shifts at 810 and 888 cm^{-1} as shown in Figure 4.12(a). These peaks belong to Fe_2O_3 and Cr_2O_3 phases, respectively (Quinn 2001, Kumar et al 2012). This indicates that there is absence of oxidation in wear track. This is due to high oxidation resistance of Al_2O_3 ball. However, several intense peaks appear when SiC and steel balls slide against the CrN/NbN coating.
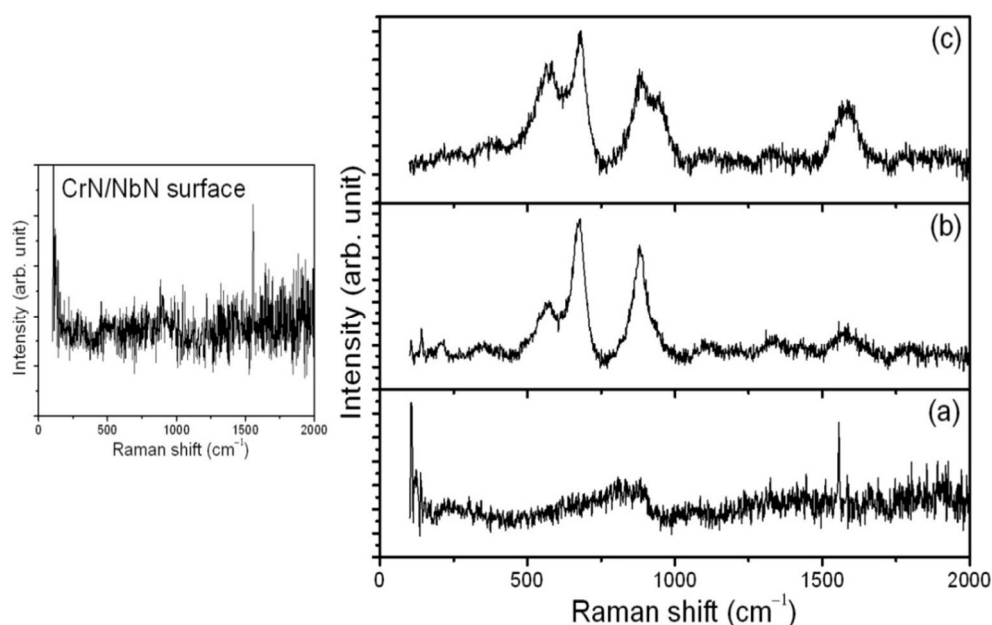
Figure 4.12 Raman spectra of virgin CrN/NbN coating surface and wear track formed sliding against (a) Al_2O_3 (b) SiC and (c) steel ball

Their peaks at 212, 574 and 882 cm^{-1} correspond to the Fe$_2$O$_3$ phase (Quinn 1971, Quinn 2001, Kumar et al 2012) when SiC ball slides against coating. This is shown in Figure 4.12(a). Both Fe$_3$O$_4$ and Cr$_2$O$_3$ peaks are observed at 345 and 673 cm^{-1}, respectively (Quinn 2001, Kumar et al 2012). Peak at 1106 cm^{-1} belong to O–H vibration arising out of contact with ambient atmospheric moisture (Phillips 1986). The spectra at 1327 and 1571 cm^{-1} belong to amorphous carbon due to ingress of atmospheric carbon. This occurs along with residual impurities present at sliding interfaces (Ferrari and Robertson 2001). In addition, peak at 1792 cm^{-1} occurs due to interaction of nitrogen molecules present in ambient atmosphere (Ferrari and Robertson 2001). Similarly, most of these features are also present in the wear track formed during sliding against steel ball as shown in Figure 4.12(c). The spectra at 260, 574 and 885 cm^{-1} belong to Fe$_2$O$_3$ phase (Quinn 1971, Quinn 2002, Quinn 1985, Wei et al 1989, Kumar et al 2012). Moreover, the spectra at 377, 677 and 949 belong to Fe$_3$O$_4$ phase (Quinn 1985, Kumar et al 2012). The peak at 1122 cm^{-1} corresponds to O–H vibration (Phillips 1986). Amorphous carbon peaks are present at 1332 and 1585 cm^{-1} (Ferrari and Robertson 2001). The above analysis shows that oxidation is significant in case while SiC and steel balls slide against CrN/NbN coating. These results are well corroborated with the wear track morphology and Raman spectral investigations.

4.4 CONCLUSION

Tribological properties of CrN/NbN superlattice coating are investigated while using 100Cr6 steel, SiC and Al$_2$O$_3$ counterbodies as friction pairs. Ultra low friction coefficient 0.01 and high wear resistance 2.6×10^{-7} mm^3/Nm was measured in case of CrN/NbN superlattice coating slide against Al$_2$O$_3$ ball. Such a low friction coefficient and high wear resistance is ascribed to high oxidation resistance and chemical inertness of

the Al_2O_3 ball. However, friction coefficient increased to 0.17 and 0.3 when coating was tested against steel and SiC balls. Similarly, wear resistance was also found to be reduced to 8.2×10^{-7} mm^3/Nm and 3.4×10^{-5} mm^3/Nm while sliding against steel and SiC balls, respectively. Such a high friction coefficient and less wear resistance are explained on the basis of oxidational wear mechanism. This mechanism dominates in the case of steel and SiC balls due to less oxidation resistance.

CHAPTER 5

TRIBOLOGICAL PROPERTIES OF DIAMOND LIKE CARBON AND NANOCRYSTALLINE DIAMOND NANOWIRE FILMS

5.1   INTRODUCTION

We have discussed that there is technological need to synthesize and design hard coatings for tribology applications (Balandin 2011, Robertson 2002, Bhaskaran et al 2002). In this respect, the carbon is one of the fascinating elements in periodic table which exists in various forms that find numerous applications. It exits in the form of diamond and graphite like structures with sp^3 and sp^2 hybridization states, respectively. DLC coating consists of a network of sp^3 and sp^2 coordinations and can exist as amorphous carbon or hydrogenated amorphous carbon (Moseler et al 2005, Zhang et al 2008, Crombez et al 2011). The sp^3 bonding state in DLC coating is mostly constituted by metastable amorphous carbon, results in superior hardness. It exhibits low friction and high wear resistance useful for several applications (Voevodin and Zabinsk 1998, Tsai and Bogy 1987, Cirino et al 2010). Nevertheless, improvement of their mechanical properties and extension of the use of DLC films for wear protection requires understanding of their friction and wear properties while sliding against various counterbodies.

Microcrystalline Diamond (MCD) film generally consists of bigger grains with a sharp boundary phase of carbon impurities. It has high surface roughness, high friction coefficient and week wear resistance (Biigli et al

1995, Erdemir et al 1999). In contrast, nanometer grain-sized polycrystalline diamond films provide smooth and low friction useful for mechanical and tribological applications (Ikeda et al 2006, Panda et al 2012, Krauss et al 2001, Konicek et al 2008). The Nanocrystalline Diamond (NCD) films are characterized as a two-phase system consisting of nanometer-sized grains and amorphous carbon that forms intercrystalline boundaries. With decreasing the diamond crystallite size, the relative volume fraction of amorphous intercrystalline boundary phase in the film increases (Auciello and Sumant 2010, Fayette et al 1998). In this condition, tribological properties of the films are dominated by the presence of boundary phase that is highly metastable. The sp^2 bonded carbon and amorphized boundary phase exhibit low friction coefficient under certain specific conditions (De Barros Bouchet et al 2012, Kumar et al 2012). However, it has low wear resistance due to reduced elastic energy leading to low fracture toughness (Geng et al 2007).

Therefore, NCD and Ultrananocrystalline Diamond (UNCD) films are not suitable for tribological application where low friction coefficient and high wear resistance are desirable features. Some specific diamond films, like hydrogenated UNCD and diamond nanowires (DNWs) show low friction coefficient and high wear resistance in humid atmosphere (Panda et al 2012, Sumant et al 2010, Sumant et al 2005). Additionally, DNWs films treated in H_2 plasma show near frictionless behavior (Sankaran et al 2013). Such a friction behavior is described by the passivation of uncompensated carbon dangling bonds by hydrogen content and adsorption of H_2O molecules (Konicek et al 2008, Konicek et al 2012). However, wear resistance of this film weakens due to large fraction of sp^2C-C bonding and amorphous carbon which persist even after the H_2 plasma treatment. In this respect, there are limited options to modify the chemical behavior of film to improve their tribological properties.

In this regard, the first part of the present chapter describes friction behavior of hydrogenated DLC coating sliding against 100Cr6 steel, Al_2O_3 and SiC balls. The chemical behavior of DLC wear tracks and wear scars on the balls was examined by micro-Raman spectroscopy and X-ray photoelectron spectroscopy. From this chemical analysis, the correlation of friction with chemical characteristic of sliding interfaces is established. In the second, tribological property of as-deposited and O_2 plasma treated DNW films were studied at moderately high loading condition and longer sliding distances. Microstructure and chemical changes in these films were investigated and correlated with friction and wear mechanism. In addition, chemical nature of the wear track and change in surface energy were also investigated. These are used to explain the friction and wear characteristics.

5.2   EXPERIMENTAL AND CHARACTERIZATION TECHNIQUES

The hydrogenated DLC coating was deposited by magnetron sputtering of graphite target in the presence of CH_4 gas in Ar plasma at a pressure of $\sim 10^{-4}$ mbar. Film thickness was 2.4 µm measured by Dektak 6M–stylus profiler using 5 mg load with a scanning speed of 30 µm/s. The topography and film roughness were measured by an AFM (Park XE-100) in non contact mode. The tribological tests were carried out by a ball-on-disc CSM tribometer (Switzerland). Various balls such as steel, Al_2O_3 and SiC were used to slide against the DLC coating. All these spherical balls have a diameter of 6 mm. The normal load was 5 N and the sliding speed was 3 cm/s. Experiments were conducted in ambient conditions where the relative humidity was 75%. The Raman spectra on the surface, wear track and ball scar were recorded in back scattering geometry using 514.5 nm line of an Ar-ion laser of a micro-Raman spectrometer. XPS (PHI 1600) with monochromatic Al $K\alpha$ radiation at 1486.74 eV was used to analyze the

chemical characteristic of DLC coating, wear debris and ball scars. Spectrometer was attached with a monochromatic X-ray source having an energy resolution of 0.6 eV. Before the measurements, the XPS instrument was calibrated in accordance with prescribed ISO standard.

DNW films were deposited on silicon (100) substrates in N_2 (94%)/CH_4 (6%) plasma by MPECVD (6" IPLAS-CYRANNUS) system, with a microwave power and frequency of 1200 W and 2.45 GHz, respectively. During the deposition, the chamber pressure was kept at 70 mbar and total flow rate of gases was maintained at 100 sccm. An external heater was used to heat the substrate to a temperature of 700 °C. The substrate temperature was measured using a thermocouple (K-type) embedded in the stainless steel substrate holder. Before the deposition of DNW film, the silicon substrates were ultrasonicated in a methanol solution containing nanodiamond (30 nm) and titanium powders (325 mesh) for 45 min to create nucleation sites. After the deposition of the DNW, the films was post treated by pure oxygen plasma for 3 and 10 min at a pressure of 7 mbar with a microwave power of 600 W.

The topography and film roughness were measured by an AFM (Park XE-100) in non contact mode. Morphological characterization of the films was carried out using a FESEM (JEOL 6500). The bonding structure of the films was characterized by Raman spectroscopy (Lab Raman HR800, Jobin Yvon) carried out at an incident wavelength of 632.8 nm. The Auger electron energy distribution was measured with a single pass varian Cylindrical Mirror Analyzer (CMA) having an integral electron gun and a continuous dynode electron multiplier connected for pulse counting detection. The primary beam energy ranged between 1200 and 1500 eV, giving an energy resolution near to 1 eV at the carbon Auger peak energy. The electron beam current at the target was kept low at approximately 50 nA with a beam

diameter less than 0.5 mm. This was needed to minimize charging and possible surface damage. The typical value of maximum count rate was 2×10^4 counts/eV that was accumulated over 5 s to maximize the Auger peak interaction. The Auger spectra from standard materials were used to calibrate the spectrometer and to check the efficiency of the analytical technique. The infrared absorbance spectra with 4 cm^{-1} resolution were obtained at normal incidence in an evacuated chamber of an IFS 66 V FTIR spectrometer (Bruker Optics). A KBr beam-splitter and a DTGS detector with KBr window were used to follow the frequency range 400–5000 cm^{-1}. This may be noted that the micro FTIR spectra were obtained from the surface of the DNW and O_2 plasma treated DNW film for a period of 10 minutes. Spectra from the wear track in corresponding DNW films were also obtained to investigate difference in surface chemistry.

Contact angles (CA) on the surface of the film and inside the wear track were measured by sessile drop method with a Kruss EasyDrop contact angle instrument (EasyDrop DSA 100). The volume of the water droplets was 1 μL. These measurements were carried out at room temperature and atmospheric pressure with a relative humidity of ~50%. Standard deviations of the CA measurements were typically ± 2°. Friction and wear behavior of films were measured by ball-on-disk tribometer (CSM, Switzerland) operating in a linear reciprocating mode. The Al_2O_3 ball with 6 mm diameter was used as a sliding couterbody against the test specimen. The normal load and sliding speeds were kept constant at 10 N and 3 cm/s, respectively. A stroke length of 3 mm was used during each experiment. The tests were carried out in ambient (dry and unlubricated) conditions with relative humidity of 72 %. In- situ wear depth was measured by a LVDT sensor coupled to this tribometer. Measurements were repeated five times on each sample and data was found to be reproducible.

5.3 RESULTS AND DISCUSSION

5.3.1 Surface topography and FTIR analysis of DLC film

Surface topography of the DLC coating was analyzed by AFM. It is shown in Figure 5.1.
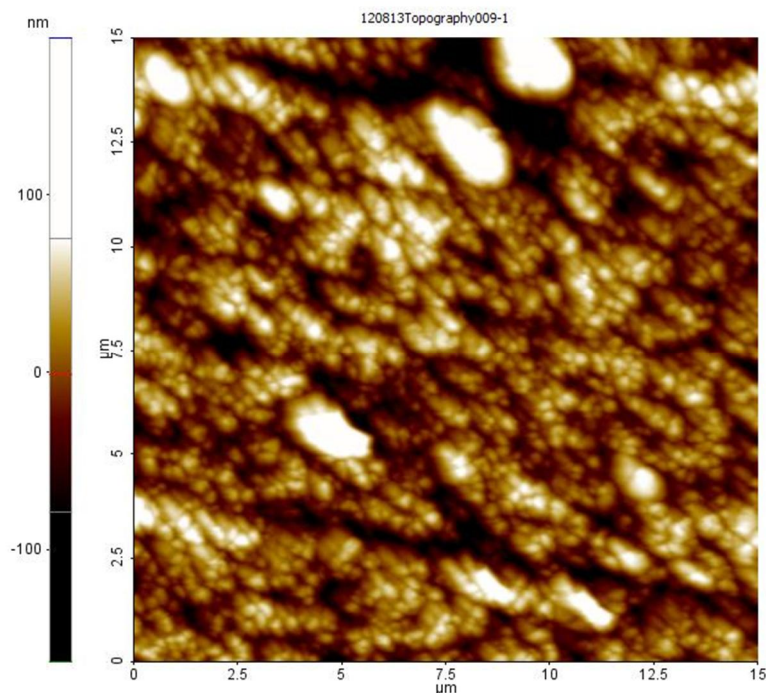
Figure 5.1 AFM image of the DLC coating

In this topography, the clusters with sp^3 bonding are well distrubuted. RMS surface roughness of the coating is ~30±2 nm. The diamond-like carbon films are usually described as an amorphous carbon network having small sp^2 carbon clusters (distorted graphitic rings) bonded by sp^3 bonds (Pandey et al 2012, Tang et al 2010, Apatiga et al 2003). Thus, it is expected that the FTIR study of DLC films prepared by the magnetron sputtering should exhibit interesting features. The spectrum indicates the presence of sp^2 and sp^3 bonded carbons as shown in Figure 5.2.
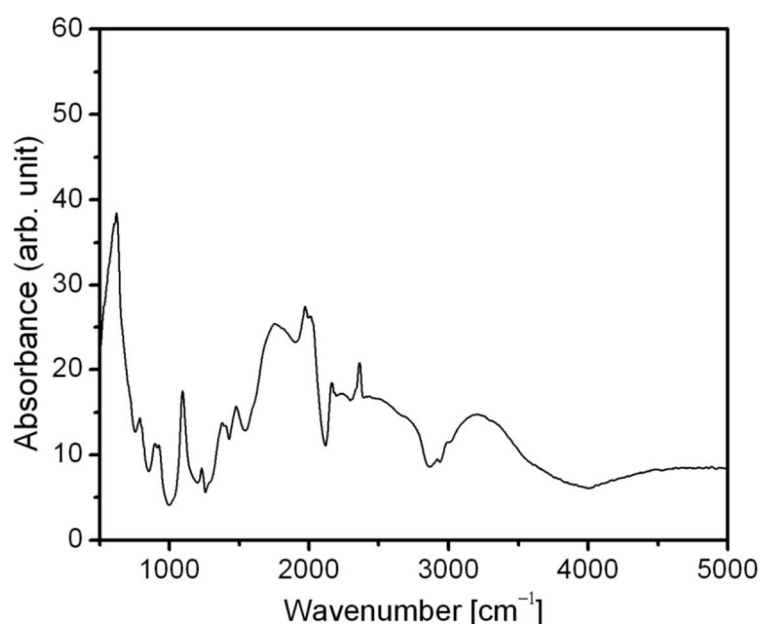
Figure 5.2 FTIR analysis on the DLC coating

In this context, the peak at 2916 cm^{-1} appears due to sp^{3}CH$_2$ bonding or sp^{3}CH symmetric modes. Small peak at 2839 cm^{-1} is assigned as sp^{3}CH$_2$ olefinic group or sp^{3}CH$_2$ bonding. Further, the peaks at 1465 and 1090 cm^{-1} correspond to C=C aromatic stretching and O–CH$_3$ deformation mode, respectively (Apatiga et al 2003, Erdemir and Donnet 2006). In addition, peaks at 1223 and 890 cm^{-1} are assigned to the bending of sp^3 hybridized of (C–H) bond which indicates the formation of hydrogenated sp^3 hybridized carbon in the DLC films.

Peak at 773 cm^{-1} is attributed to the out of plane bending vibration of graphite like carbon (Erdemir and Donnet 2006). A broad band at 1624 cm^{-1} is assigned to sp^2 hybridized (C=C) bonding. Another broad signal around 1740 cm^{-1} is attributed to the presence of carbonyl group (C=O). Further, spectra show sharp peaks around 2375 cm^{-1} which corresponds to C=O group occurring due to interaction of atmospheric CO$_2$. In addition, a broad absorption band between 3700 cm^{-1} and 3000 cm^{-1} appears due to OH group (Pandey et al 2012, Apatiga et al 2003). This group is caused by the

adsorption of water molecules in the hydrogenated DLC film. The shoulder around 3500 cm^{-1} is ascribed to O–H groups arising due to adsorption of atmospheric moisture. The FTIR analysis confirms that the DLC coating is hydrogenated and contains sp^3 matrix bonded with sp^2 carbon. Moreover, carboxylic and hydroxylic groups are present in the coating as impurities arising from deposition process and atmospheric contamination.

5.4 TRIBOLOGICAL PROPERTIES OF DLC FILM

It is clearly shown that friction coefficient does not deviate much while it slides against steel, Al$_2$O$_3$ and SiC balls. The results are shown in Figure 5.3.
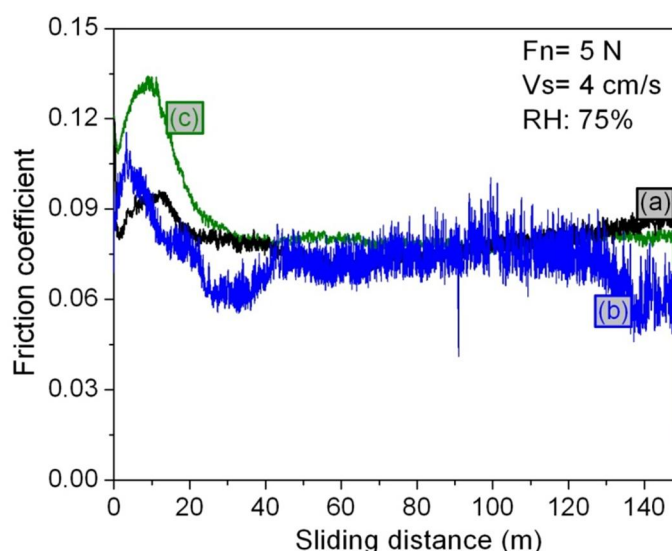
Figure 5.3 **Tribological properties of hydrogenated DLC film sliding against (a) steel (b) SiC and (c) Al$_2$O3 balls**

However, there are significant changes in these values during initial sliding passes. But the trend of friction coefficient is similar in all the sliding pairs such as DLC/steel, DLC/Al$_2$O$_3$ and DLC/SiC. However, during initial sliding passes, the magnitude of friction coefficient is high in DLC/Al$_2$O$_3$ and DLC/SiC ball as compared to the DLC/steel sliding pair. To understand the

friction mechanism in these sliding pairs, two different approaches are considered. Firstly, the micro- mechanical aspect may govern the friction behavior. Secondly, surface micro- chemistry changes among sliding pairs is important to consider for explaining such friction behavior. Above two approaches, were used to explain friction behavior while sliding with various counterbodies.

Firstly, during initial sliding cycles, the increase in friction coefficient in the sliding system of DLC/Al_2O_3, DLC/SiC and DLC/steel is governed by the surface roughness of the ball. In this case, the surface asperities of ball and DLC's rough surface asperities mechanically interlock resisting for sliding (Erdemir and Donnet 2006). Therefore, friction mechanism during initial sliding cycles is governed by mechanical interlocking between surface asperities. In this region, it is noticed that at the outset friction coefficient increases and then it gradually decreases. The increase in friction coefficient is ascribed to deformation of asperities across sliding interface. The contact area of the sliding interfaces increase when the asperities deform. Therefore, larger contact area with asperities appears that causes to decrease in contact stress. In this case, friction coefficient decreases due to plastic deformation of surface asperities. This means that smooth sliding surfaces appear which are mechanically polished during the course of sliding.

In DLC/Al_2O_3 and DLC/SiC sliding systems, initially the magnitude of friction coefficient is high compared to DLC/steel sliding pair. This could be explained by two reasons. Firstly, harder surface asperities present on Al_2O_3 and SiC balls due to high hardness of 22 GPa and 18 GPa, respectively. However, hardness of steel ball is only 2.8 GPa, which deforms quite easily compared to harder Al_2O_3 and SiC balls (Sharma et al 2012). It means that hardness of the asperities present on Al_2O_3 and SiC balls are high which has high resistance for plastic deformation. It takes longer sliding

distance to get smoothened. This behavior is translated into high sliding resistance yielding high friction coefficient. Secondly, chemical reactivity of Al_2O_3 and SiC balls are less which does not have much ability to passivate the dangling bonds. These dangling bonds have covalent and ionic chemical bonds that cause to increase in friction coefficient. In contrast, steel ball is chemically active and it can easily form metal oxide scales which passivate the dangling bonds, hence low friction coefficient (Konicek et al 2008). The magnitude of surface roughness is more or less similar for all the three balls. It is 0.06, 0.04 and 0.05 µm in steel, Al_2O_3 and SiC balls, respectively. In view of this, the influence of roughness on the friction behavior is similar for all the balls. For the longer sliding distances, it is observed that the values of friction coefficients in all the three sliding systems are nearly similar.

5.4.1   Raman spectra of the Film surface, Wear track and Ball scars

To explain the friction mechanism, the Raman spectra on the DLC wear track (Figure 5.4) and ball scars (Figure 5.5) were recorded and compared with the spectra obtained from the virgin DLC.
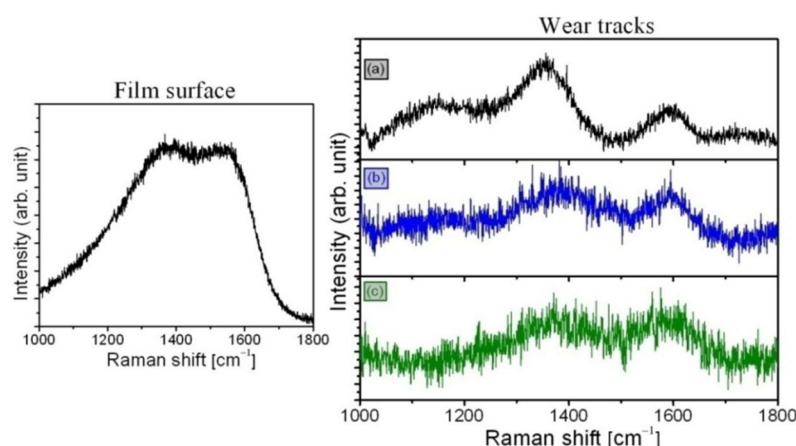
Figure 5.4   Raman spectra of DLC film surface and inside the wear track formed using (a) steel (b) SiC and (c) Al₂O3 balls

On the virgin surface of DLC, the peak at 1378 cm^{-1}, designated as D band, represents zone-edge A_{1g} mode appears due to the disorder which involves phonons near the K zone boundary (Ferrari et al 1999). The G peak represents stretching of all the pairs of sp^2 atoms centered on 1544 cm^{-1} that correspond to sp^2 network. These peaks are found to present on the wear track inscribed while sliding against various counterbodies.
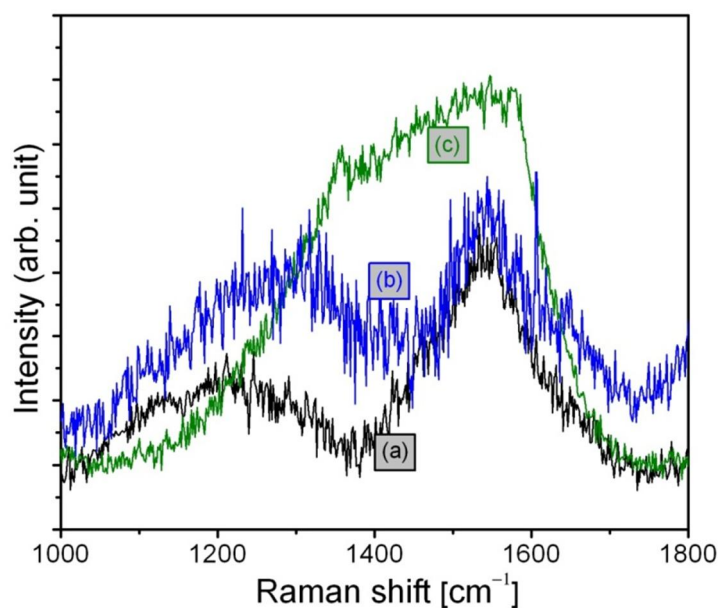
Figure 5.5 **Raman spectra on the ball scars of (a) steel (b) SiC and (c) Al$_2$O$_3$ balls**

However, D and G bands shift to lower and higher wavenumbers, respectively. The shift of the wavenumber corresponds to strain which arises due to sliding (Ferrari et al 1999, Ferrari and Robertson 2001). The chemical nature of the carbon present in the wear track is identified as a-C. The conversion of diamond like to a-C occurs by tribochemical reaction during the sliding.

In addition, the Raman spectra obtained from the ball scars also show typical features of amorphous like carbon (Figure 5.5). In this case, the peaks are broader and shifted to lower wavenumbers. This could be related to

strain due to disorder in a-C network. From this analysis, it is confirmed that DLC wear tracks and ball scars are constituted by a-C. This means formation of transferlayer and sliding exhibited between a-C/a-C layers (Gayathri et al 2012). In this condition, the friction mechanism is governed by sliding between a-C layers.

However, the chemical features of balls contacting with DLC are absent. This is the reason that the friction coefficient in all the three sliding systems is more or less similar because the chemical nature of the sliding systems is similar at sliding interfaces. Therefore, it is confirmed that in the initial sliding passes the friction mechanism is dominated by surface roughness of the ball. When the roughness disappears due to the surface smoothening, the carbonaceous transferlayer is developed on the ball and the ensuing friction mechanism persists through a-C/a-C sliding layers. To investigate the transferlayer formation on the ball scar, the Raman spectra was obtained after a sliding distance of 8 m. It is shown in Figure 5.6.
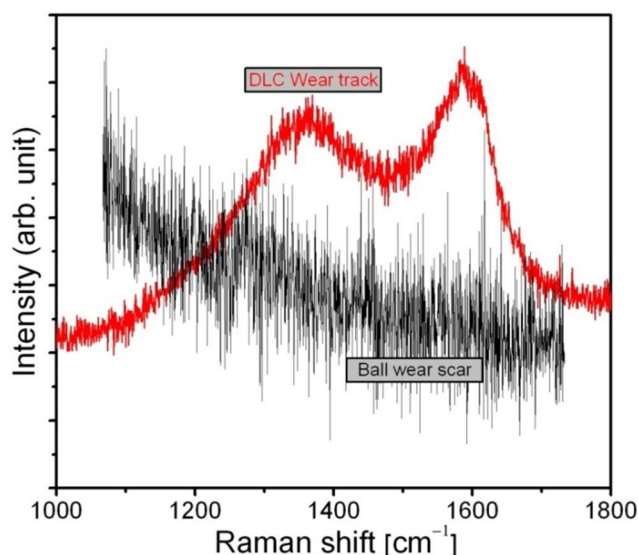
Figure 5.6   Raman spectra on steel ball scar and DLC wear track obtained at sliding distance of 8 m

The purpose of this particular experiment was to determine the formation of transferlayer and the alteration of value of friction coefficient that normally depends on surface roughness. Interestingly, on the ball scar, the typical feature of DLC or a-C related peaks were absent (Figure 5.6). However, on the DLC wear track, the G peak becomes intense as compared to virgin DLC surface. In addition, D peak is broadened. This behavior corresponds to sliding induced graphitization of DLC wear track. Here, it is confirmed that the initial friction mechanism does not depend on transferlayer formation. The transferlayer develops after lapse of longer sliding distance when sliding surfaces get smoothened.

5.4.2   XPS Analysis of Wear Debris

To understand the detail chemical nature of the transferlayer and wear debris, the XPS measurements were carried out. The results are shown in Figure 5.7.
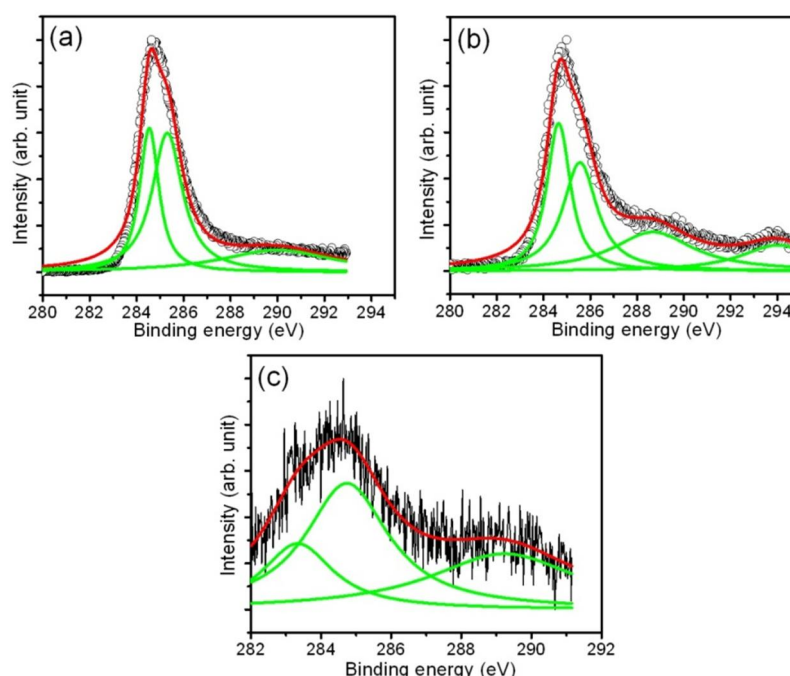
Figure 5.7   XPS measurements on (a) DLC coating (b) wear debris formed with steel ball and (c) steel ball scar

The spectral background was subtracted using Shirley's method (Janos 2004). Moreover, the data were fitted with Lorentian peaks with binding energies located at 284.5, 285.3, 289.9 eV corresponding to $sp^2C=C$, sp^3C-C and $HO-C=O$ bonds, respectively (Yue et al 1999, Paik 2005). This is shown in Figure 5.7(a). However, spectra were modified for wear debris formed due to sliding of DLC coating with steel as shown in Figure 5.7(b).

It shows that in wear debris, the $sp^2C=C$ increases and sp^3C-C fraction decreases as compared to DLC virgin surface. The result is shown in Figure 5.7(a). The increase in $sp^2C=C$ fraction is attributed to tribochemically induced graphitization. Further, the shifts of $sp^2C=C$ and sp^3C-C peaks to higher binding energies are observed. These shifts are associated with the surface charging of wear debris due to oxidation. Two other peaks were observed at binding energies 288.6 and 294 eV corresponding to highly charged $C=O$ bonding. These peaks originated from tribochemical reaction in ambient atmosphere. In addition, XPS measurement on the steel ball scar showed three peaks centered at 283.3, 284.7 and 289.2 eV, corresponding to $sp^1C=C$, sp^2C-C and $C=O$ bondings, respectively. This is presented in Figure 5.7(c). The peak of sp^3C-C is found to be absent on the ball scars. Here, it can be conclude that chemical nature of carbon bonding in the wear track of DLC coating, wear debris and ball scars is different from such other and it is essentially linked to the tribochemical reactions.

5.5 TRIBOLOGY OF NANOCRYSTALLINE DNW FILMS

5.5.1 Morphology and Surface Topography of the Films

The top-view FESEM micrographs of as-deposited and O_2 plasma treated DNW films are shown in Figure 5.8. It can be observed that as-deposited DNW film possesses highly dense and uniformly distributed wire-

like granular morphology as presented in Figure 5.8(a). These wires are composed of several UNCD grains. The boundary of this wire consists of chemical impurities like a-C and sp^{2}C-C bonded constituents. The thickness of the graphitic shield varies from a few atomic layers to more than 5 nm (Vlasov et al 2007). Tilting of a single nanowire around its long axis reveals that the shape and the diameter always remain unaltered. This confirms to cylindrical shape of the nanowire and the presence of coated graphitic sheath. However, after the O$_2$ plasma treatment for 3 and 10 minutes, the wire-like features collapsed as shown in Figure 5.8(b) and (c). The transition in structure and morphology of the as-deposited DNW film occurs due to O$_2$ plasma treatment. This process removes sp^{2}C-C bonded carbon from the sheath of DNW. When this sheath is etched out, the wire collapses.
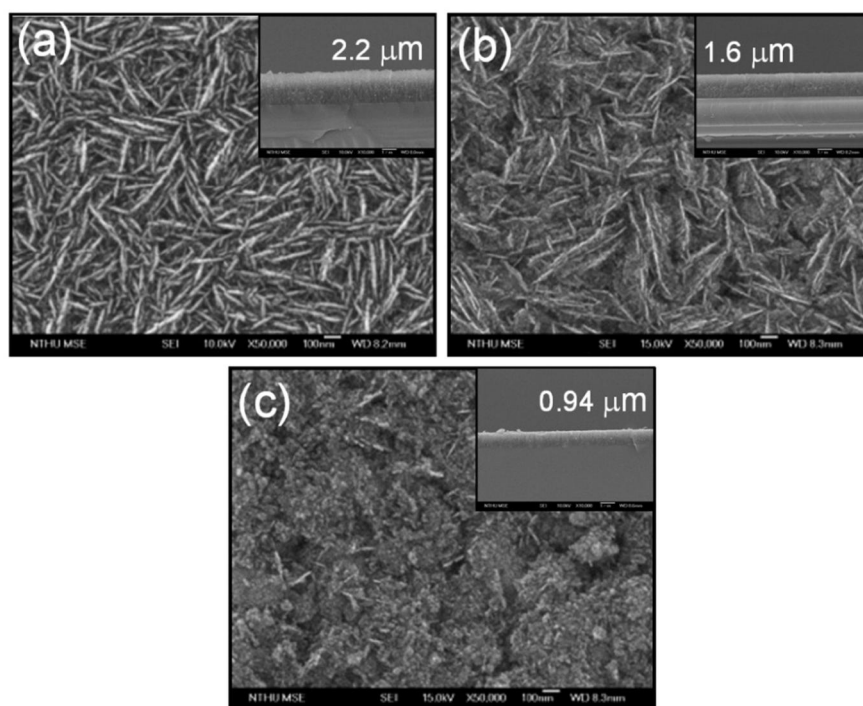
Figure 5.8   Morphology of (a) as-deposited DNW film and O$_2$ plasma treatment at (b) 3 minutes and (c) 10 minutes.

In the inset of these images, the cross section of the film shows significant decline in thickness of film upon O$_2$ plasma exposure. This

happens due to etching of sp^2C-C sites from the sp^3C-C bonded crystals. This process further densifies the film morphology. In AFM image, the surface topography of the film is shown (Figure 5.9). In Figure 5.9(a), the DNWs are clearly seen in which several nanograins are encapsulated. However, after the O_2 plasma treatment, the wire- like morphology collapses as shown in Figure 5.9(b) and (c). The surface roughness of as-deposited DNW film is 6.5 nm which increases to 12 nm upon exposure to O_2 plasma for 3 minutes. The results are shown in Figure 5.9(a) and (b), respectively. However, surface roughness decreases to ~7 nm in O_2 plasma treated film for 10 minutes as shown in Figure 5.9(c).
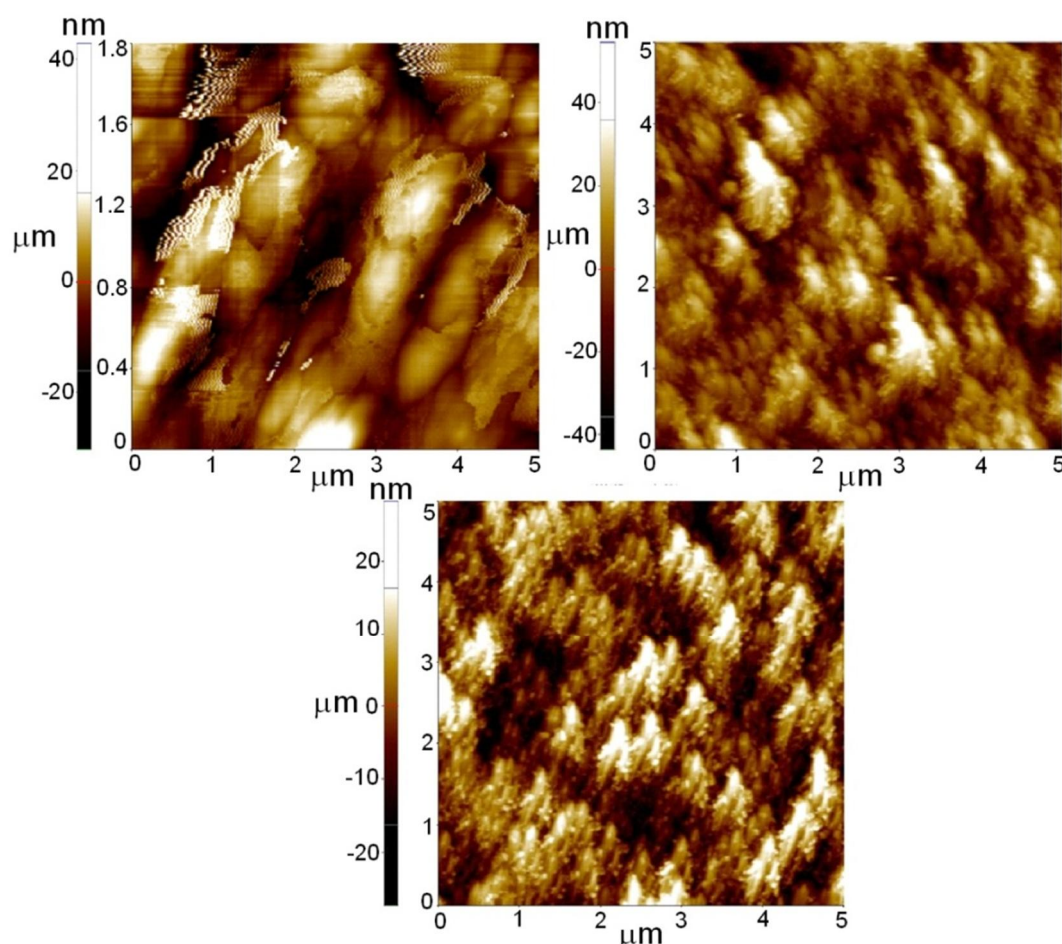
Figure 5.9 **AFM topography of (a) as-deposited DNW film and O_2 plasma treatment at (b) 3 minutes and (c) 10 minute**

5.5.2   Raman Spectroscopy

Figure 5.10 shows the Raman spectra recorded at 632.8 nm on as-deposited and O_2 plasma treated DNW films. Gaussian fits were used to study these parameters. In the fitting the Gaussian line was justified because this shape is expected for a random distribution of phonon lifetimes in disorder materials (Casiraghi et al 2005, Ferrari and Robertson 2001). Typical UNCD Raman spectral features can be seen in all these samples. These consist of six distinctive peaks shown in Figure 5.10(a) and Figure 5.10(b). However, only five peaks are observed in Figure 5.10(c). Peak assigned as v_1 (1116–1142 cm^{-1}), v_2 (1165–1177 cm^{-1}) and v_3 (1486–1505 cm^{-1}) originated from C–H bending and C–C stretching Raman modes of trans-polyacetylene (t-PA or poly-CH*x*). The t-PA is an alternate chain of sp^2C-C carbon atoms in which single hydrogen is bonded to each carbon atom. This occurs in the grain boundary of UNCD crystallites. After the O_2 plasma treatment, the v_3 peak shifts to higher wavenumber. This behavior is associated with bond disorder in C–H and C–C of t-PA Raman modes. The v_3 peak corresponding to C–C bond disorder is absent in Figure 5.10(c) due to excessive oxygenation. Furthermore, the pair of peaks assigned as D (1326–1330 cm^{-1}) and G (1562–1571 cm^{-1}) bands correspond to sp^2C-C bonded carbon.

The G band has E_{2g} symmetry which appears due to bond-stretching vibration of a pair of sp^2C-C sites in the form of olefinic chains or aromatic rings. Further, D band is A_{1g} breathing mode of a sixfold aromatic ring which is activated by disorder. This band is shifted to higher wavenumebr after the O_2 plasma exposure leading to increase in sp^3C-C bonded fraction. Consequently, the results show that the plasma etching treatment leads to the shift of D and G bands towards lower wave numbers and a decrease in I(D)/I(G) ratio (Casiraghi et al 2005, Ferrari et al 1999). The width of the *G* peak FWHM characterizes bond length as well as bond angle

distortion. In Figure 5.10(a), FWHM of G peak is low which gets slightly broadened after O_2 plasma treatment as shown in Figure 5.10(b) and Figure 5.10(c). This indicates that the graphitic clusters become smaller in size and get more disordered (Arenal et al 2008). As a result of this, the sp^3C-C/sp^2C-C ratio increased after the O_2 plasma treatment. This means that O ions generated by O_2 plasma leads to increase in sp^3C-C fraction consisting of sp^3C–H group on the surface. In addition to these features, the G* (1603–1620 cm^{-1}) peak corresponds to in-plane clusters of nanocrystalline graphite. Broadening of this peak consistently increases after the O_2 plasma treatment.
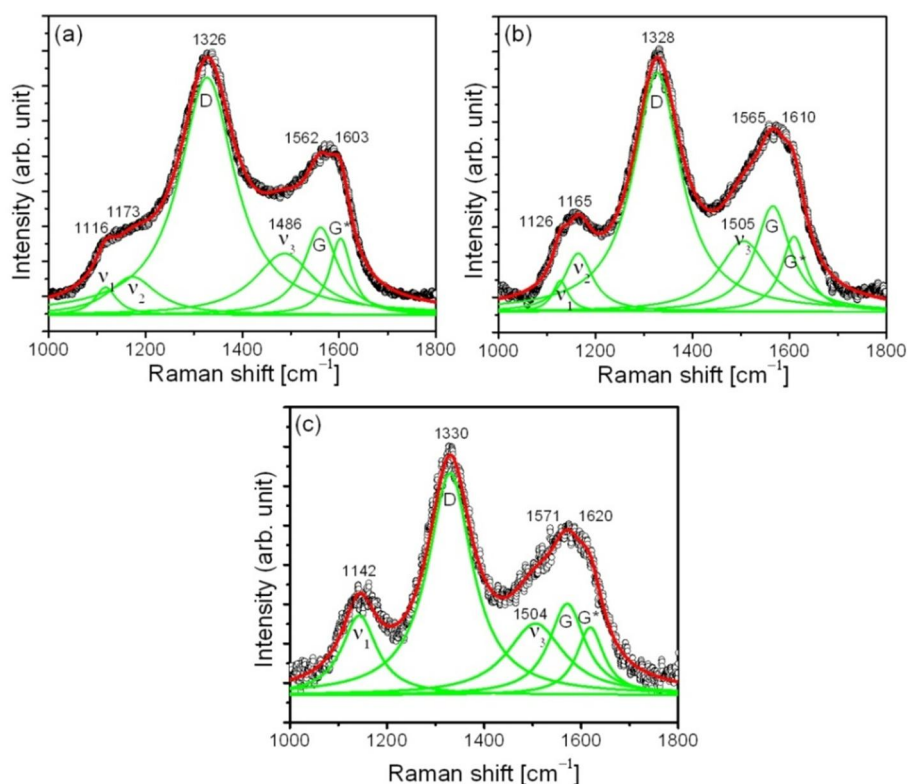
Figure 5.10 Raman spectra of (a) as-deposited DNW film and O$_2$ plasma treatment at (b) 3 minutes and (c) 10 minutes.

This behavior is associated with the disorder in nanocrystalline graphite that occurs upon O_2 plasma exposure. The atomic concentration of nitrogen incorporated into the films is much less even with N_2 addition to an extent of 20% to the plasma gas. Therefore, the vibration frequencies of these

systems are expected to be close to those of the pure carbon ones i.e., 1300–1600 cm^{-1} for aromatic sp^{2}C-C rings and 1500–1600 cm^{-1} for olefinic chains. Thus, in the region 1300–1600 cm^{-1}, there is no particular signal that could be distinguished from these modes compared with those belonging to carbon structures. Therefore, it is reasonable to ignore formation of C–N and N–N type of modes in the present study (Arenal et al 2008).

5.5.3   Auger Electron Spectroscopy

AES is a surface analytical technique used to determine the chemical bonding state (Gutiérrez et al 1997, Sharda et al 1998). In Figure 5.11(a), the AES spectra show the as-deposited DNW film containing high fraction of sp^{2}C-C bonding state. After O$_2$ plasma treatment, the shape and intensity of the peak changes and it clearly shows that peak related to sp^{2}C-C i.e., G band is reduced and broadened as shown in Figure 5.11(a) and (b). This indicates reduction in sp^{2}C-C bonding state upon O$_2$ plasmas exposure. However, intensity of (b$_1$) peak, corresponding to D band increases in oxygen plasma treated film. The peak (c$_1$) i.e., G band has a lower kinetic energy position than one observed for as- deposited DNW film. It is well corroborated by the Raman spectra. Feature (a$_1$) is assigned to self-convolution of occupied π states in the valence band of sp^{2}C-C atoms. Subsequently, intensity of this band decreases as shown in the Figure 5.11(b) and (c). The presence of feature (a$_1$) induces a broadening of the Auger main peak a$_o$.

This increases with the sp^{2}C-C content (Gutiérrez et al 1997, Sharda et al 1998). The width of a$_o$ peak corresponds to amount of π bonding present in the film. Another important aspect of the spectra is the relative intensities of the maxima in the dN(E)/dE plot marked as G and D near the main a$_o$ peak (Sharda et al 1998). The intensity of D band is higher relative to

G band and the ratio of I(D)/I(G) is 1.8, 1.2 and 0.8 in Figure 5.11(a-c), respectively. This indicates that after the O_2 plasma treatment, the sp^2C-C fraction is decreased. This is in agreement with the SEM image and Raman spectra.
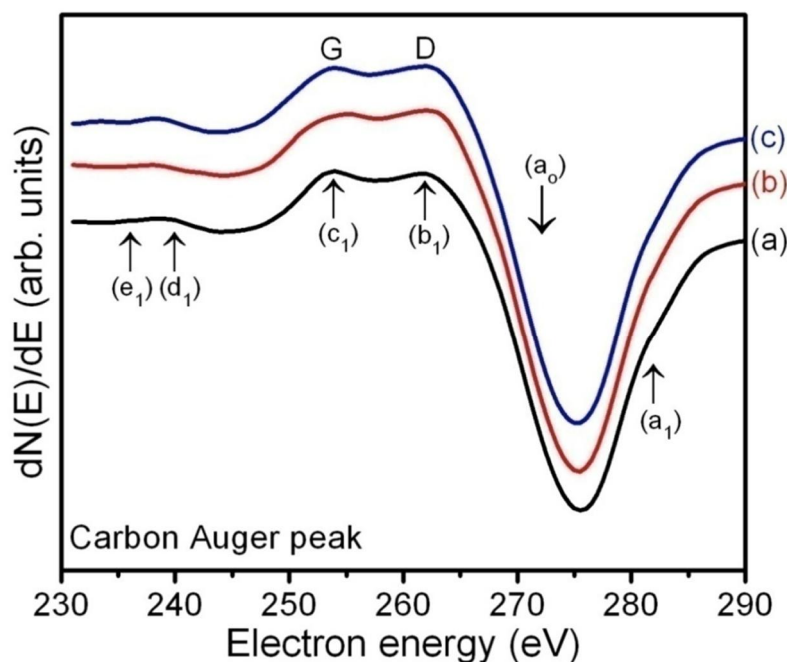
Figure 5.11   Carbon *KLL* Auger spectra in (a) as-deposited DNW film and O_2 plasma treatment at (b) 3 minutes and (c) 10 minutes

Furthermore, the characteristic plasmon loss features, (d_1) and (e_1) are also found to be present. The intensity of plasmon peak is high in O_2 plasma treated film. Thus the main Auger (KV_1V_1) transition a_o peak is located at 275 eV in these films. The same peak in natural diamond occurs at 268 eV. The observed shift is related to charging of the film. It is noted that the prominent features of the Auger line shape of diamond (D and G) are very sensitive to the surface states. Therefore, changes suggest a surface reconstruction resulting in formation of localized sp^2C-C bonding (Sharda et al 1998). Hence, the Auger peak shape is a characteristic of the diamond lattice where oxygen plasma causes dangling bond formation and subsequently carbon carbon interaction leading to sp^3C-C characteristics.

5.5.4   X-ray Photoelectron Spectroscopy

The XPS studies were carried out on as-deposited and O_2 treated DNW films as shown in Figure 5.5. In as-deposited DNW film as shown in Figure 5.12(a), the C1s peak is observed at 285.02 eV which is shifted by 1.32 and 3.17 eV towards higher binding energy after O_2 plasma treatment for 3 and 10 minutes, respectively. These are shown in Figure 5.12(b) and Figure 5.12(c), respectively.
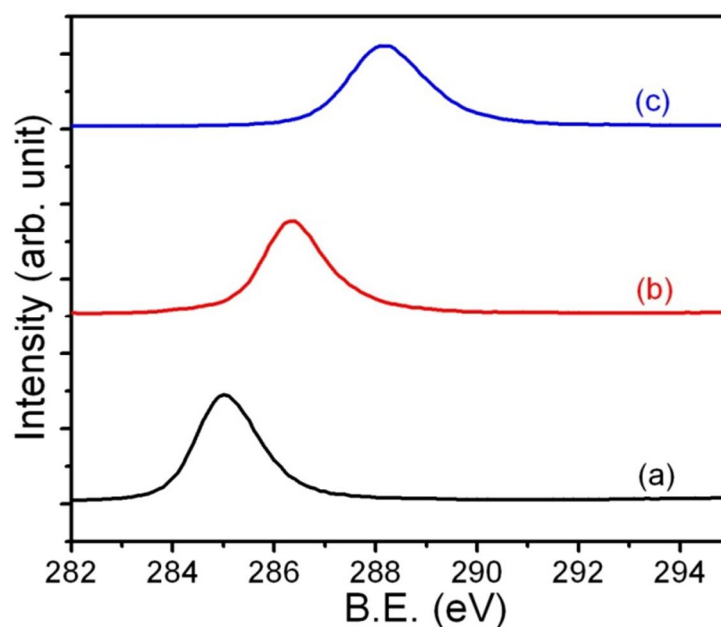
Figure 5.12   XPS of C1s spectra of (a) as-deposited DNW film and O_2 plasma treatment at (b) 3 minutes and (c) 10 minutes.

Similarly, O1s peak is observed at 532.7 eV in pristine DNW film as presented in Figure 5.13(a) which is shifted to 0.4 and 2.1 eV after the O_2 plasma treatment for 3 and 10 minutes, respectively (Ma et al 2006, Janos 2004, Li et al 2011). These are shown in Figure 5.13(b) and Figure 5.13(c), respectively. The intensity of O1s peak for as-deposited DNW film is low and this is associated with adsorption of oxygen from the ambient atmosphere in the form of surface impurities.

However, the intensity of the peak increases with O_2 plasma treatment time. This happens due to adsorption of oxygen in the film. The shift of the peaks is related to surface charging due to oxidation of DNW film. It involves generation of electron trapping centers in these films. Trapping of charges in the defect states is a possible reason for enhanced surface charging. Hence, C1s and O1s peaks shift to higher binding energy (Joseph et al 2008). This is also evident from AES results as shown in Figure 5.11. In addition, the O_2 plasma treatment produces defect complexes such as carbon clusters, vacancies and dimers. These defect complexes act as electron trapping sites that further enhances surface charging leading to shift of the C1s and O1s peaks to higher binding energy.
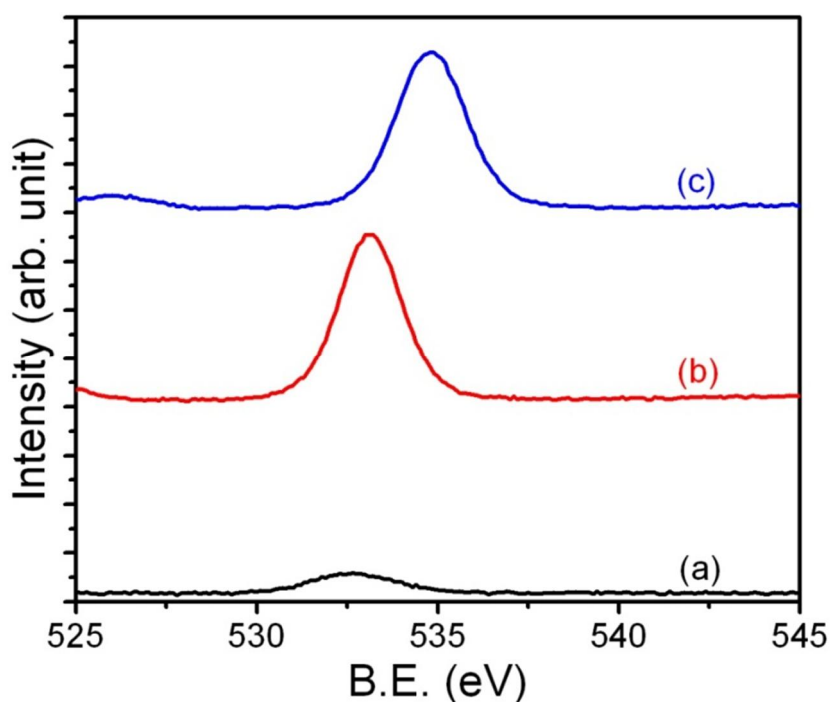
Figure 5.13 XPS of O1s spectra of (a) as-deposited DNW film and O_2 plasma treatment at (b) 3 minutes and (c) 10 minutes.

5.5.5 FTIR Studies on Virgin DNW Film Surface

Investigation of functional bonding state on the surface is one of the important aspects to describe the surface energy. In this aspect, O_2 plasma

treated diamond film showed an enhanced band at 1774 cm^{-1} which corresponds to C=O group. Several bands in the region 1363–1017 cm^{-1} are assigned to the C–O–C stretching vibration (Figure 5.14).
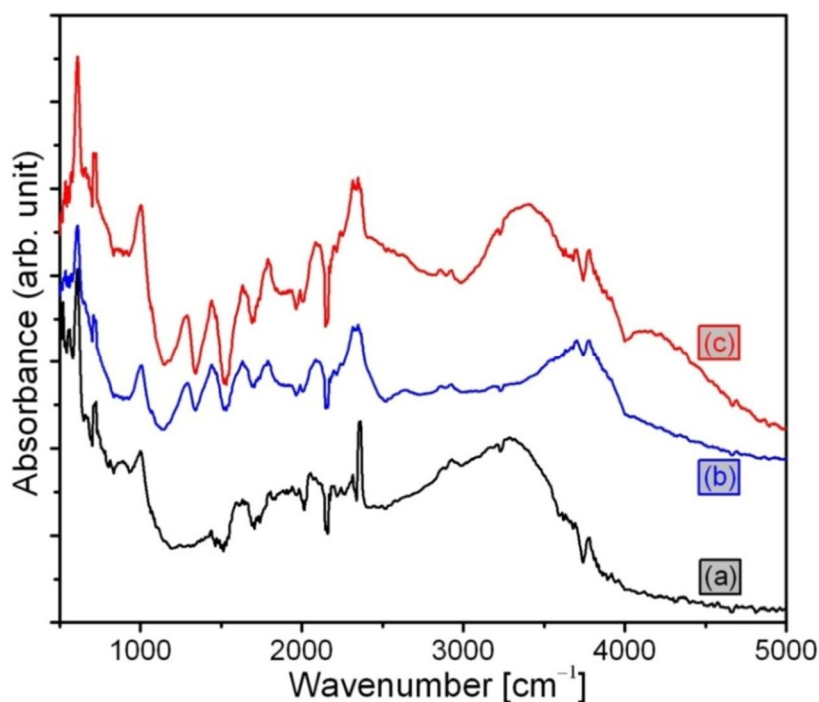
Figure 5.14 FTIR spectra of (a) as-deposited DNW film and O$_2$ plasma treatment at (b) 3 minutes and (c) 10 minutes.

The presence of these functional groups indicates oxidation of film during the O$_2$ plasma exposure. These bands are rather weak in as-deposited DNW film as shown in Figure 5.14(a). In contrast, these bands become stronger after O$_2$ plasma exposure as given in Figure 5.14(a) and (b). The peak appearing at 1640 cm^{-1} is due to physically adsorbed molecular water. This indicates that O$_2$ atoms react with H$_2$ to form H$_2$O molecules (Pandey et al 2012, Tang et al 2010, Apatiga et al 2010). Oxygen basically occupies the grain boundaries of the diamond crystallites.

Further, diamond crystallites contain sp^{3}C-C hybridized bonding state. However, sp^{2}C-C and a-C occupies grain boundaries. Oxygenated

plasma predominantly affects the grain boundaries since existence of dangling bond density in this region is rather high. Moreover, several absorption bands are observed in the spectral range 2800–3100 cm^{-1} which arises from C–H stretching vibrations. It suggests that hydrogenation of diamond film occurs during the synthesis. In this respect, two prominent peaks present at 2930 and 2852 cm^{-1}, are assigned to the stretching vibration of C–H bond specific to hydrogenated diamond. These peaks belong to symmetric and anti-symmetric stretching vibrations of sp^{3}CH$_3$ and sp^{2}CH$_2$, respectively. The diamond crystallites contain sp^{3}C-C hybridized carbon atoms and grain boundaries are occupied by both sp^{3}C-C and sp^{2}C-C hybridized carbon atoms. The C–H vibrational frequencies are assigned according to the carbon hybridization (sp^3, sp^2 or sp^1) and group (C–H$_3$, C–H$_2$ or C–H). Thus, the C–H stretching frequency depends weakly on the arrangement of more distant neighbors. This suggests that the hydrogen was incorporated into non-crystalline or defective regions of the film. Oxygenation occurs easily in the grain boundaries since more dangling bonds exist (Apatiga et al 2010).

Further, the peak at 1465 and 1090 cm^{-1} corresponds to C=C aromatic stretching and O–CH$_3$ deformation mode, respectively (Pandey et al 2012, Tang et al 2010). In addition, peaks at 1223 and 890 cm^{-1} are assigned to the bending of sp^{3}C-C hybridized C–H bond which indicates formation of hydrogenated sp^{3}C-C carbon. Peak at 773 cm^{-1} is attributed to the out of plane bending vibration of graphite like carbon (Tang et al 2010). A broad band at 1624 cm^{-1} is assigned to sp^{2}C-C hybridized (C=C) bonding. The shoulder around 3500 cm^{-1} is ascribed to O–H groups arising from interaction with atmospheric moisture. Other two peaks at 3680 and 3772 cm^{-1}, correspond to symmetric and antisymmetric vibration mode of H$_2$O molecules, respectively. The symmetric vibration mode present at 3680 cm^{-1} is absent in as-deposited DNW film. However, intensity of these peaks

increase with O_2 plasma treatment time. High adsorption of H_2O molecules is favorable due to high surface energy of O_2 plasma treated film.

5.5.6   FTIR Studies in Wear Track of DNW Film

The micro FTIR spectra were obtained from the wear track inscribed in as-deposited and 10 minutes O_2 plasma exposed DNW film. The results are shown in the Figure 5.15(a) and Figure 5.15(b). From different location of each wear track, 30 FTIR spectra were obtained. The nature of spectra (shape, size and intensity) obtained from each wear track was more or less similar. In this respect, three representative spectra from the each track are plotted. Spectra from wear track of plasma exposed DNW film, as-deposited film and virgin surface possess distinctive features (Figure 5.14). Wear track of both as-deposited and plasma exposed DNW films yielded enhanced spectral intensities. The O_2 plasma treated DNW film shows an intense band at 1772 cm^{-1} which corresponds to C=O group. Several bands in the region 1400–1000 cm^{-1}, assigned to the C–O–C stretching vibration (Pandey et al 2012, Tang et al 2010) indicated that the diamond film is prone to surface oxidation in wear tracks. This is shown in Figure 5.8(b).
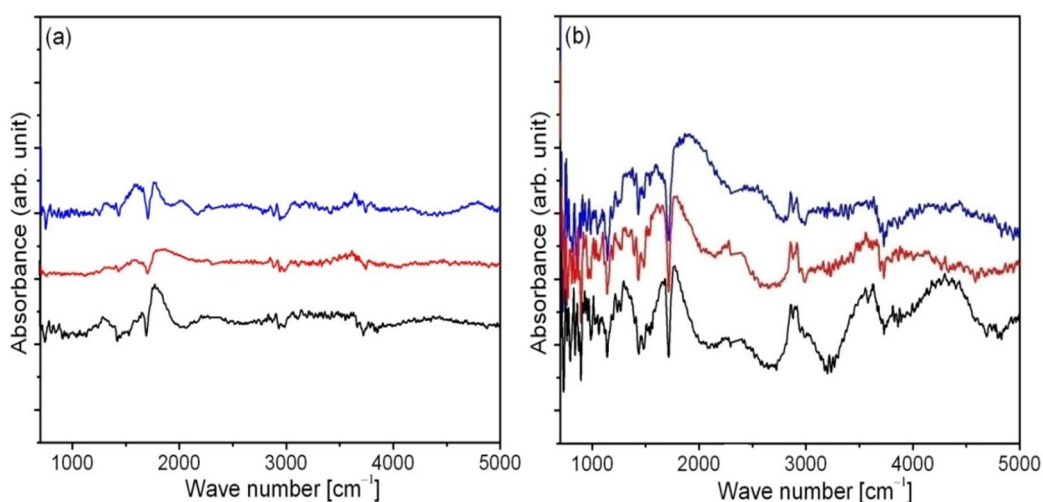
Figure 5.15 FTIR spectra in the wear track of (a) as-deposited DNW and (b) O_2 plasma treated DNW film for 10 minutes

High oxidation is caused by the presence of more C=O and C–O–C group in the O_2 plasma treated DNW film as shown in Figure 5.14. The oxidation process is activated by the tribochemical reaction in the presence of atmospheric oxygen. These bands are rather weak on the surface of as-deposited DNW film and wear track of as-deposited DNW film. The results are shown in Figure 5.114(a) and Figure 5.15(a), respectively. The peak at 1640 cm^{-1} becomes more intense in the wear track of O_2 plasma treated DNW film due to physisorption of molecular H_2O (Apatiga et al 2003). Such a high adsorption of H_2O molecules occurs due to increase in dangling bond density in wear track. Further, the intensity of spectra in range 2800–3100 cm^{-1}, in the wear track increases. This arises from C–H stretching vibrations (Tang et al 2010, Apatiga et al 2003). The increase in intensity of C–H vibration is caused by tribochemical reaction with hydrogen molecules present in ambient atmosphere and carbon in the DNW film.

Moreover, the intensity of spectra present at 2930 and 2852 cm^{-1} corresponding to sp^3CH_3 and sp^2CH_2 groups increase in the wear track formed in both the samples (Figure 7). The intensification of these bands is rather strong in the wear track of O_2 plasma treated DNW film. The peaks around 1410–1465 and 1050–1100 cm^{-1} correspond to C=C aromatic stretching and O–CH_3 deformation mode, respectively (Pandey et al 2012, Tang et al 2010). In addition, the intensity of peak at 1223 and 890 cm^{-1} assigned to the bending of sp^3C-C also increases. Increase in intensity of peak at 3525 cm^{-1} is ascribed to O–H groups formed by tribochemical reaction with atmospheric moisture. Other two peaks at 3560 and 3628 cm^{-1} correspond to symmetric and antisymmetric vibration modes of H_2O molecules. The symmetric vibration mode present at 3680 cm^{-1} is absent in DNW film surface. However, intensity of these peaks increase in the wear track of O_2 plasma treated sample. High adsorption of H_2O molecules is favorable due to high surface energy of O_2 plasma treated film.

5.5.7 Contact Angle Measurements

To investigate the role of surface energy in tribo chemical interactions, the CA was measured by sessile drop method using distilled water. Image analysis method was used to calculate CA from the shape of the droplet. On the as-deposited DNW surface the CA is 152° and it represents superhydrophobic behavior as shown in Figure 5.16(a). However, after the O_2 plasma treatment of DNW film, the film surface becomes superhydrophilic with CA 36.5^o and 16° as shown in Figure 5.16(b) and Figure 5.16(c), respectively. It was observed that the superhydrophobic property of DNW film persist even after H_2 plasma treatment (Sankaran et al 2013). However, O_2 plasma treated DNW film shows transition to superhydrophilic behavior. The enhancement of the hydrophobic properties of diamond in hydrogenation is associated with adsorption processes on the surface. As a result of hydrogen chemisorption, the dangling carbon bonds are saturated to form C−H bonds, leading to a weaker film-water interaction (hydrophobic behavior) (Ostrovskaya et al 2007, Ostrovskaya et al 2005, Azevedo et al 2009).
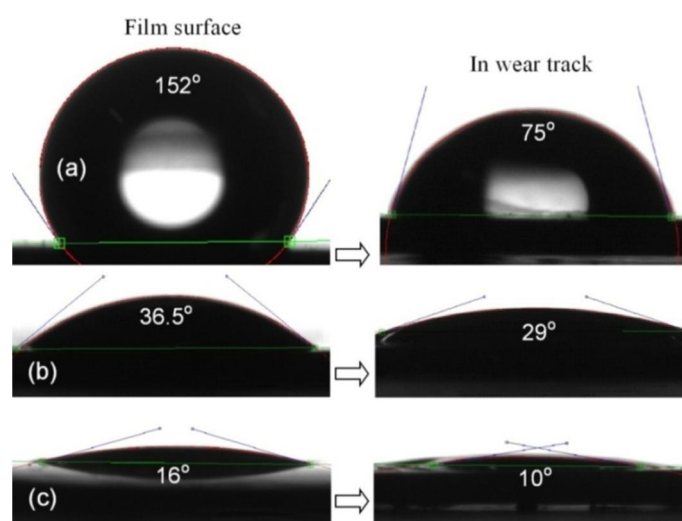
Figure 5.16   Contact angle of (a) as-deposited DNW film and O_2 plasma treatment at (b) 3 minutes and (c) 10 minutes.

The surface dipole moment is reduced due to the formation of a dipole layer initiated by heteropolar C^--H^+ bonds. This, in turn, weakens the interaction between polar water molecules and the film surface. Under oxygenation, the surface is made more reactive due to the formation of oxygen containing functional groups serving as active centers for water wetting. The replacement of nonpolar C−H bonds by polar C−O bonds transforms the surface to hydrophilic one. This means that the high concentration of carbon– oxygen sites is generated after O_2 plasma treatment. This is clearly shown in FTIR and XPS results. Origin to increase the surface energy is related to increase in electron centers that are dangling bonds due to O_2 plasma treatment of the films. It is seen from XPS and AES analysis that surface charging is increases due to O_2 plasma treatment that causes to increase chemically reactive centers. The O_2 plasma treatment is related to the increase in dangling bonds from sp^3C-C sites desorbed at the carbon network of the surface. The weakly bonded sp^2C-C carbon atoms at grain boundaries are removed by oxygen atoms during the oxidation.

However, it is an analytically established that the graphitic content is high in as-deposited DNW film that points to the absence of surface reaction centers implying absence of dangling bonds on the surface. This is responsible for low wettability of as-deposited DNW film. A comparison among these data shows that depending on the chemical state of the surface, the film can assume either hydrophobic or hydrophilic (Ostrovskaya et al 2007, Azevedo et al 2009). The surface roughness of the films was measured over an area of 2 μm × 2 μm. The rms roughness of the as-deposited DNW film is 22±1.8 nm which slightly decreases to 20±1.3 nm and 18±1.6 nm after the O_2 plasma treatment for 3 and 10 minutes, respectively. These values are comparable to rms roughness of the film obtained after the H_2 plasma treatment of as-deposited DNW film (Sankaran et al 2013). This indicates that the roughness of the diamond films remained almost unaffected under H_2 and

O$_2$ plasma treatments. On account of these facts, the effect of surface roughness on wettability behavior of the films is ignored. However, plasma surface treatment and plasma (H$_2$ and O$_2$) strongly modifies the chemical and bonding nature of the surface. In the right side of the Figure 5.16, the corresponding CA inside the wear track is shown. It is clearly shows that the CA in the wear track consistently decreases in as-deposited and O$_2$ plasma treated DNW films. This means surface energy within the wear track is high compared to the surface of the film. Such an increase in surface energy in wear track is related to tribo induced changes in chemical state.

It is understood that wear track is mechanically deformed and this leads to an increase in defect complexes. These defect complexes cause increase in dangling bonds that leads to increase in chemical reactivity. These dangling bonds are passivated by C=O, C–O–C and H$_2$O functional groups and molecules as clearly seen from FTIR analysis of wear tracks. The results are shown in Figure. 5.15(a) and (b), respectively. Thus, the decrease in CA and superhydrophilic behavior is supported by the presence of these functional groups and molecules in the wear track.

5.6 TRIBOLOGICAL MECHANISM

In this section, tribological properties of as-deposited and O$_2$ plasma treated DNW films are discussed on the basis of microstructure and surface chemistry. The value of friction coefficient is high ~0.17 in as-deposited DNW film as shown in Figure 5.17(a). However, after the O$_2$ plasma treatment of DNW film, this value significantly decreases to ~0.06 and ~0.002 as shown in Figure 5.17(b) and Figure 5.17(c), respectively. This behavior of friction coefficient is measured in earlier work on H$_2$ plasma treated DNW film while using mN loading range (Sankaran et al 2013). The as-deposited DNW film shows friction coefficient in the range 0.2–0.28 while

using loading conditions in mN loading regime. However, this value was consistently decreased to near frictionless one after the H_2 plasma exposure.
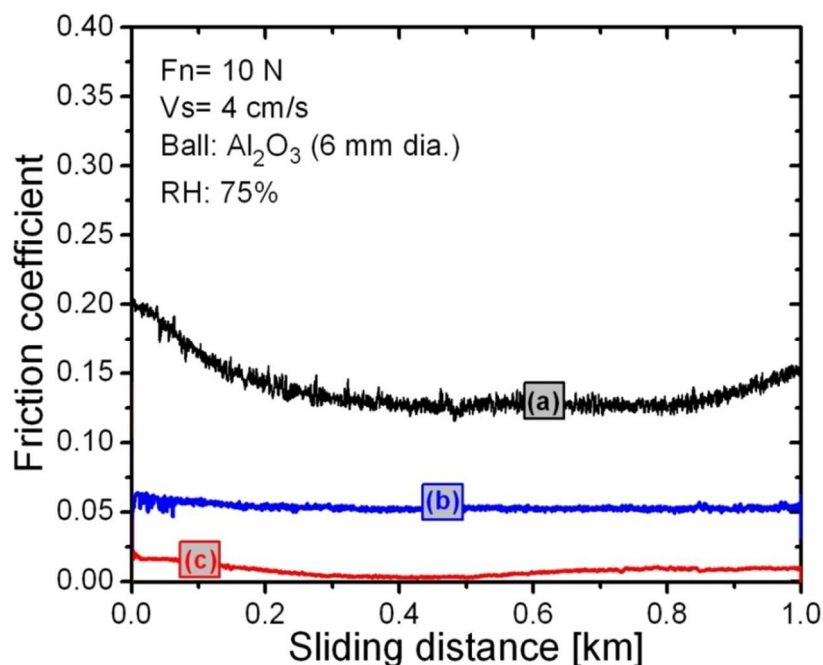
Figure 5.17 Tribological properties of (a) as-deposited DNW film and O_2 plasma treatment at (b) 3 minutes and (c) 10 minutes.

This was explained by surface passivation of dangling bonds with formation of C-H bonding state. However, in present work, extremely high wear resistance with low friction coefficient could be observed in O_2 plasma treated film at moderately high loading condition. In this context, insitu penetration depth measured by LVDT sensor is shown in Figure 5.18. In as-deposited DNW film (Figure 5.18(a)), the depth is higher compared to O_2 plasma treated film as shown in Figure 5.18(b) and Figure 5.18(c). Such a stable and steady friction curve indicates negligible deformation during the tribo- test. Moreover, depth profile of wear track after the tribo- test is shown in inset of Figure 5.18. The penetration depth in as-deposited DNW film is ~200 nm as shown in curve (a) in inset of Figure 5.18. However, after the

plasma treatment, the depth profile decreases to ~150 and ~80 nm as shown in inset of curves (b) and (c), respectively. Such reduced wear depth is obtained even after the 1 km sliding distance at 10 N loads.
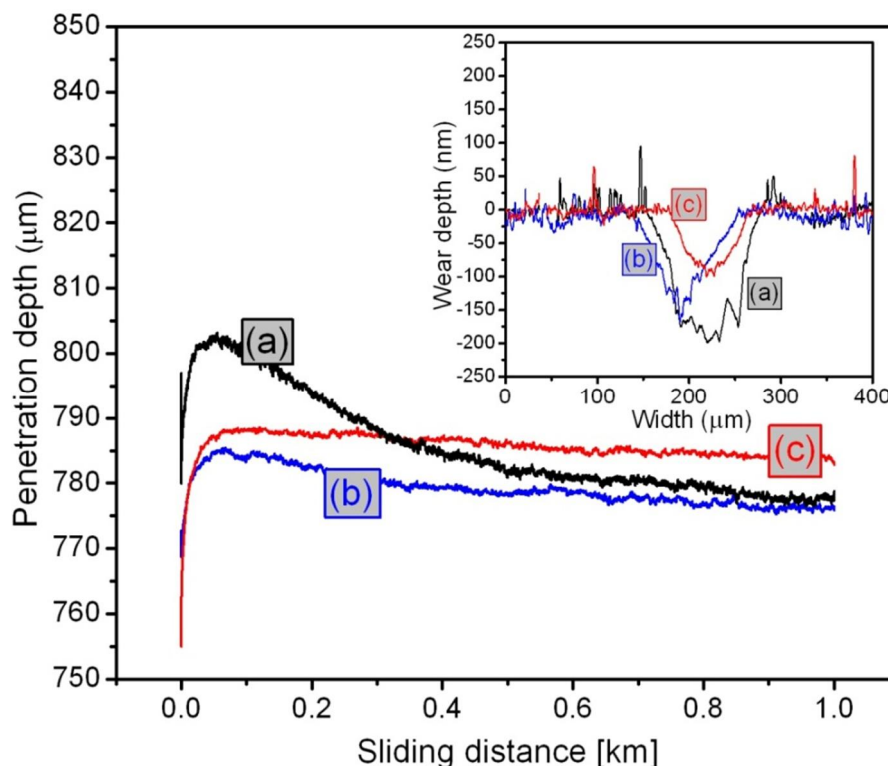
Figure 5.18 Insitu depth profiles of (a) as-deposited DNW film and O$_2$ plasma treatment at (b) 3 minutes and (c) 10 minutes.

This behavior shows extremely high wear resistance of the films. This is described by calculating the wear rate. It is calculated by considering the wear track width and depth as given in the inset of Figure 5.18 to compute wear volume and subsequently wear rate according to relationship given in Equation (2.12). The relationship of friction coefficient and wear rate is presented in Figure 5.19. Results show decrease in wear rate with decreasing friction coefficient. In this figure, data points (a), (b) and (c) represent as-deposited, O$_2$ plasma treated DNW film at 3 and 10 minutes, respectively. It is exceedingly low in 10 minutes O$_2$ plasma treated film.

5.6.1 Raman Imaging of Wear Tracks

To investigate such a high wear resistance and relation with chemical behavior of wear track, the micro Raman imaging was carried out on as-deposited and 10 minutes O_2 plasma treated DNW films.
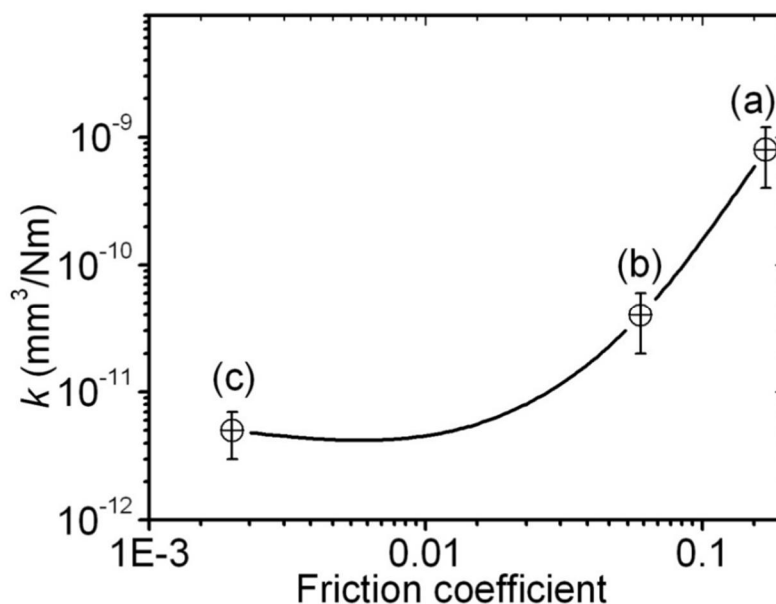
Figure 5.19 Relationship of friction coefficient vs wear rate of as-deposited and O_2 plasma treated DNW for 3 and 10 minutes

These are shown in Figure 5.20 and Figure 5.21, respectively. In both the wear tracks, the spectral features associated with DNW are present. All the peaks such as ν_1, ν_2, ν_3, D, G and G* are clearly observed. However, in both the wear tracks, peak shape and intensity differ as compared to film surface. This change is related to chemical changes in the wear track. In addition, peaks centered at 943 and 978 cm^{-1} (marked as a symbol in Figure 5.20) correspond to α–Al_2O_3 (Misra et al 2001, Otto et al 1989). The genesis of this peak is related to wear of the Al_2O_3 ball. These peaks are not observed in Figure 5.21. This means absence of wear particles from the Al_2O_3 ball due to low value of friction coefficient. The Raman intensity of peak on the edge of wear track in as-deposited DNW film is high as shown in Figure 5.20(a).

The spectral location corresponds to less deformed region. However, in this region, Al_2O_3 peaks are observed due to wear debris which accumulates on the edge of the wear track during the sliding. The intensity of the Raman peaks decreases inside the track as clearly seen in Figure 5.20(b) and at centre of the track Figure 5.20(c).
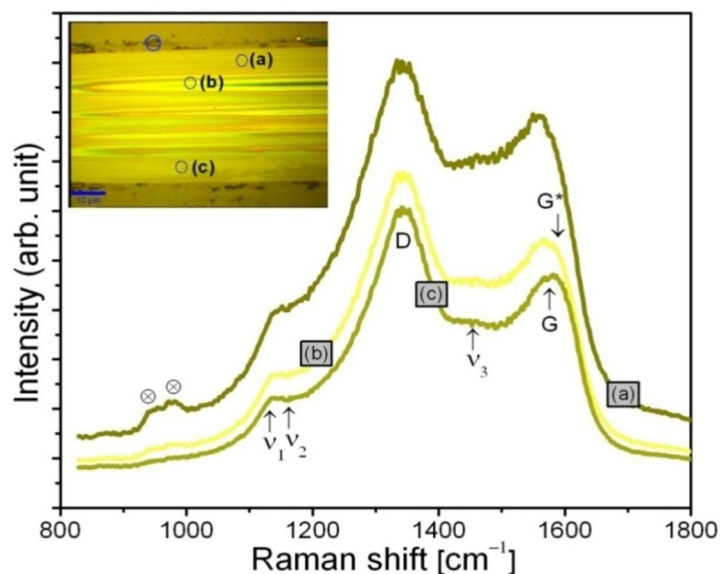
Figure 5.20 Raman imaging of (a) as-deposited DNW film.
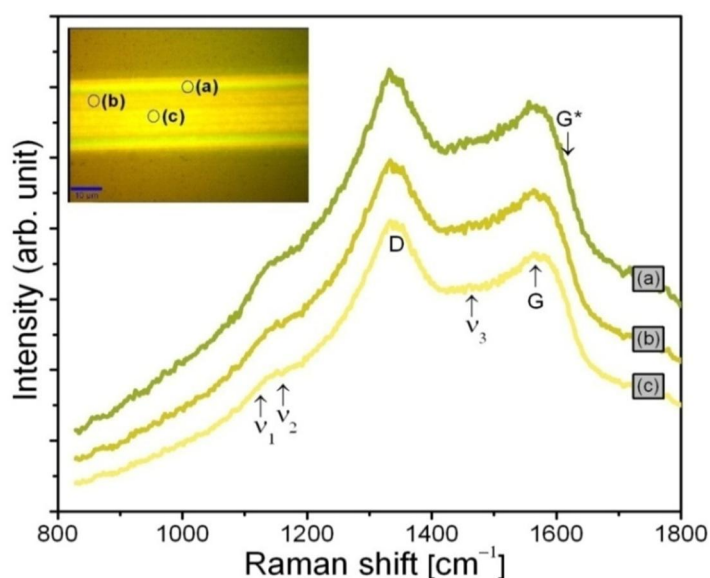
Figure 5.21 Raman imaging of O_2 plasma treated DNW film for 10 minutes

The weak intensity corresponds to deformed region of the track. Consequently, O_2 plasma treated DNW film shows no significant difference in peak intensity and shape of the Raman spectra acquired from wear track (Figure 5.20). The intensity is slightly increased on the edge of the track compared to the central region. These are presented in Figure 5.21(a) and (b), respectively. Overall, high chemical stability of wear track in O_2 plasma treated film explains extremely high wear resistance. This analysis clearly states that the stability of the nanostructured diamond feature in wear tracks is preserved while sliding even up to 1 km at 10 N load.

In as-deposited DNW film, the friction coefficient is mainly associated with large fraction of lubricated sp^2C-C bonded graphitic phases that exist in the grain boundaries of the DNW sheath. In this particular film, the friction coefficient is related to low surface energy which is evident by high contact angle 152° and hence possesses hydrophobic nature. The capability to adsorb C–O–C, C=O, O–H and H_2O molecules is low because of low surface energy of as-deposited DNW film. It is evident by FTIR analysis of the surface and corresponding wear tracks of as-deposited DNW film. The results are shown in Figure 5.14(a) and Figure 5.15(a), respectively.

In this condition, mechanism of surface passivation during tribology test is limited if the adsorption of above mentioned functional groups and molecules are not energetically favored. Further, dissociation of H_2O molecules and formation of C–H, C–O–C, H_2O and C–OH bonds are inadequate as evident by FTIR analysis and do not sufficiently act to chemically passivate the uncompensated valence electrons of C–C bonds. In contrast, super low friction coefficient is ascribed by high surface energy. It is evident from the CA measurement that O_2 plasma treated film shows superhydrophilic behavior. The quantity of adsorbed H_2O molecules, C=O, C–O–C and O–H groups is high due to high surface energy of the oxygenated

surface. The spectral intensity from these chemical groups is rather high in the wear track of O_2 plasma treated DNW film as shown in Figure 5.15(b).

It is shown that the main effect of the adsorbates is to prevent the formation of covalent C–C bond across the contact interfaces. In this condition, the dangling carbon covalent bonds are significantly passivated and transformed through van der Waals and hydrogen bonding. These bonds are rather week compared to the covalent C–C bond. In the corresponding wear track, the CA angle is rather low compared to the virgin surface. The decrease in CA leads to the formation of chemically active sites in the wear track where adsorption of the molecules is high. Further, the CA is lowest in 10 minutes O_2 plasma treated film where electrostatic attraction between the positively charged surface and the compensating water droplet is strong (Zilibotti et al 2009). In this condition, capability of the surface to "self-lubricate" by adsorbing water molecules into the diamond surface further leads to decrease in friction coefficient. The existence of H_2O molecules and the adsorbing capability of the surface consisting of a reservoir of chemical species which continuously saturate the carbon dangling bonds originating at the sliding interface. In this condition, thin layer of adsorbate molecules are present between the contacting interfaces during the tribology test. This layer prevents direct surface to surface contact during the sliding hence results in extremely high wear resistance.

5.7 CONCLUSION

Friction behavior of hydrogenated DLC coating was investigated using three kinds of sliding balls such as steel, Al_2O_3 and SiC. During initial sliding cycles, the friction coefficient was high while using these balls. However, after lapse of longer sliding cycles, the friction coefficient decreases for all the three sliding systems i.e., DLC/steel, DLC/Al_2O_3 and DLC/SiC. For initial sliding cycles, friction mechanism is exhibited by

surface roughness of the sliding systems. However, for longer sliding cycles, the friction behavior is governed by formation of carbonaceous transferlayer when sliding occurs between carbon/carbon layers.

The DNW films were deposited by N_2 gas mixed MPECVD process. As-deposited DNW film was treated in O_2 plasma which results in chemical and microstructural modification. The DNW is chemically constituted by sp^3C-C bonded carbon network where the sheath of these wires contains a-C and sp^2C-C bonded chemical species. After the O_2 plasma exposure, the nanowire collapses due to chemical etching of a-C and sp^2C-C sites which acts as a capsule to preserve the diamond crystallites. After the O_2 plasma treatment, the resulting oxidation and formation of functional groups such as C=O, C–O–C, O–H, O–CH_3 and H_2O molecule increase on the surface. Oxidation and formation of functional groups transform sub-superhydrophobic behavior of as-deposited DNW film into superhydroplic one. Further, advanced tribological properties such as super low friction coefficient and extremely high wear resistance are exhibited in O_2 plasma treated DNW film. Such an advance characteristics is explained by transformation of covalent dangling bonds into hydrogen and weak van der Waals bonding by oxygen plasma treatment. After the treatment, the surface energy is increases which favor adsorbtion and dissociation of chemical species such as H_2O and O–H. Thus, these chemical species are rather high in the wear tracks of O_2 plasma treated DNW film. These species passivate the covalent dangling bonds and form thin adsorbate layer during the tribology test. This layer acts as an interfacial lubricant and prevents direct contact of the surfaces during the sliding. This causes extremely high wear resistance. Such highly advanced tribological properties of O_2 plasma treated films are useful for several real applications in machine tools and mechanical components where low friction coefficient and high wear resistance are desirable feature for energy efficiency and component's longer life.

CHAPTER 6

SUMMARY AND SUGGESTIONS FOR FUTURE WORK

6.1   SUMMARY

An introduction to the tribological properties of hard coatings was given followed by wear mechanism and deformation behavior governing to friction and wear resistance. Tribological properties and evaluation of wear mechanism is introduced in the respect of microstructure and chemical behaviour of the sliding interfaces. Various wear mechanism with different combination of sliding surfaces such as hard coating/soft ball and soft ball/hard coating is introduced in order to understand the wear mechanism. The fundamentals of some of the characterization techniques used to study the mechanical, tribological, morphological, structural, and chemical properties of the coating and wear tracks are discussed.

It is shown that how in the modern technology tribologically suitable component and devices are important to increase the energy efficiency. In this regard, it is discussed that the hard coatings deposited by PVD techniques are adequate solutions for increasing the lifetime of tools and components commonly employed in many different industrial applications. In this respect, the present work deals with systematic studies of tribological properties of hard coatings such as TiAl, TiAlN, CrN and carbon based coating such as DLC and nanocrystalline DNW films. In all the coatings, the tribological properties and wear mechanism are studied in the respect of

microstructure such as hardness, elastic modulus and chemical reactivity of the sliding surface.

Instrumented microindentation tests were performed on γ -Ti-48Al-2Cr-2Nb alloy after hipping at various loads using a Vickers indenter. Hardness and elastic modulus are calculated by the Oliver-Pharr method and the energetic approach by Attaf. The indentation hardness and elastic modulus calculated from the work of indentation approach seem to correlate well with the Oliver-Pharr method at lower as well as higher loads. Deviations in the average hardness may be attributed to the fact of the surface roughness and the mechanical polishing effects. The ratio of hf/h_{max} ranging from 0.80 to 0.82 at various loads indicates the pile-up effect theoretically. In addition some specific material constants describing the properties of materials such as ($v_T, v_P,\ v_E, v_{ET},\ v_{PT}, v_{EP}$) are calculated. The processing route HIP and AEBM process which are successfully being used for the production of γ –TiAl alloys having exceptionally high strength index (K) and nominal yield strength after the Holloman's fitting.

Tribological behavior of γ-TiAl alloy is investigated while sliding against 100Cr6 steel, SiC and Al_2O_3 as counterbodies for friction pairs. The friction coefficient and wear rate was high when γ-TiAl alloy slides with Al_2O_3 and SiC ball. However, these values were less while sliding against steel ball. The wear mechanism is explained by the sliding combination of harder/harder such as SiC/γ-TiAl and Al_2O_3/γ-TiAl alloy. However, softer/harder sliding combination acts in steel/γ-TiAl alloy. Penetration depth during friction measurement shows more or less similar value. This means that magnitude of composite wear is similar in all the three sliding combination. However, deformation of wear track follows the trend of friction coefficient. The wear track is wider in the sliding combination of SiC/γ-TiAl

and Al_2O_3/γ-TiAl alloy. However, in steel/γ-TiAl alloy sliding combination the wear track was narrow.

Tribological properties of TiAlN ternary nitride system which is known as technologically important materials for various applications including wear resistant due to high oxidation resistance at high temperature are studied. Oxidation resistance of TiAlN is governed by higher chemical stability, in comparison to binary nitrides like TiN and AlN coatings.

Tribological properties of TiAlN coating was studied while sliding against various counterbodies such as 100Cr6 steel, SiC and Al_2O_3. Friction coefficient of TiAlN/Al_2O_3 sliding pair was significantly high with the values in the range 0.6–0.9. In this system, wear rate of Al_2O_3 ball and TiAlN coating was in the same order 5.7×10^{-6} and 2.3×10^{-6} mm^3/Nm, respectively. For this sliding pair, the wear mechanism was governed by plastic deformation. However, the friction coefficient was less than 0.2 in sliding pair of TiAlN/steel. The wear rate of SiC ball and TiAlN coating was also in the same order 4.3×10^{-7} and 1.7×10^{-7} mm^3/Nm. Improved tribological properties in this system is governed by the formation of lubricious oxide layer. In the sliding system of TiAlN/steel ball, the value of friction coefficient is ~0.3. The wear arte of TiAlN coating sliding with steel ball is insignificant 4.0×10^{-10} mm^3/Nm. However, the wear rate of ball is high 2.8×10^{-4} mm^3/Nm. In this sliding pair, the mechanism of wear is oxidational.

The properties of superlattice coatings are dependent on the period of the individual layers in the structure. In this coating, the layer thickness is less enough such that the coatings form a superlattice structure. The structural and chemical characteristics of this coating were studied by XRD, XPS and Raman spectroscopy. The morphology of the honeycomb like structure of CrN/NbN superlattice is shown in with the formation of droplets and grooves.

The presence of deeper craters and larger droplets is responsible for the high roughness which is typical of arc-deposited CrN/NbN supperlattice.

Tribological properties of CrN/NbN superlattice coating are investigated while using 100Cr6 steel, SiC and Al_2O_3 counterbodies as friction pairs. Ultra low friction coefficient 0.01 and high wear resistance 2.6×10^{-7} mm^3/Nm was measured in case of CrN/NbN superlattice coating slide against Al_2O_3 ball. Such a low friction coefficient and high wear resistance is ascribed to high oxidation resistance and chemical inertness of the Al_2O_3 ball. However, friction coefficient increased to 0.17 and 0.3 when coating was tested against steel and SiC balls. Similarly, wear resistance was also found to be reduced to 8.2×10^{-7} mm^3/Nm and 3.4×10^{-5} mm^3/Nm while sliding against steel and SiC balls, respectively. Such a high friction coefficient and less wear resistance are explained on the basis of oxidational wear mechanism. This mechanism dominated in case of steel and SiC balls due to less oxidation resistance.

Friction behavior of hydrogenated DLC coating was investigated using three kinds of sliding balls such as steel, Al_2O_3 and SiC. During initial sliding cycles, the friction coefficient was high while using these balls. However, after lapse of longer sliding cycles, the friction coefficient decreases for all the three sliding systems i.e., DLC/steel, DLC/Al_2O_3 and DLC/SiC. For initial sliding cycles, friction mechanism is exhibited by surface roughness of the sliding systems. However, for longer sliding cycles, the friction behavior is governed by formation of carbonaceous transferlayer when sliding occurs between carbon/carbon layers.

The DNW films were deposited by N_2 gas mixed MPECVD process. As-deposited DNW film was treated in O_2 plasma which results in chemical and microstructural modification. The DNW is chemically

constituted by sp^3C-C bonded carbon network where the sheath of these wires contains a-C and sp^2C-C bonded chemical species. After the O_2 plasma exposure, the nanowire collapses due to chemical etching of a-C and sp^2C-C sites which acts as a capsule to preserve the diamond crystallites. After the O_2 plasma treatment, the resulting oxidation and formation of functional groups such as C=O, C–O–C, O–H, O–CH$_3$ and H_2O molecule increase on the surface. Oxidation and formation of functional groups transform sub-superhydrophobic behavior of as-deposited DNW film into superhydroplic one.

Advanced tribological properties such as super low friction coefficient and extremely high wear resistance are exhibited in O_2 plasma treated DNW film. Such an advance characteristics is explained by transformation of covalent dangling bonds into hydrogen and weak van der Waals bonding by oxygen plasma treatment. After the treatment, the surface energy is increases which favor adsorbtion and dissociation of chemical species such as H_2O and O–H. Thus, these chemical species are rather high in the wear tracks of O_2 plasma treated DNW film. These species passivate the covalent dangling bonds and form thin adsorbate layer during the tribology test. This layer acts as an interfacial lubricant and prevents direct contact of the surfaces during the sliding. This causes extremely high wear resistance. Such highly advanced tribological properties of O_2 plasma treated films are useful for several real applications in machine tools and mechanical components where low friction coefficient and high wear resistance are desirable feature for energy efficiency and component's longer life.

6.2 SUGGESTIONS FOR FUTURE WORK

High temperature tribology on these coatings can be performed to understand the wear mechanism and phase changes. At high temperature wear

tests, the deformation behavior and oxidation resistance will be useful to evaluate the performance for high temperature devices and components application.

Load and sliding speed dependent friction and wear behavior on these coatings will be useful to understand wear mechanism and related microstructural and chemical changes of the sliding surfaces.

Humidity dependent wear mechanism can be useful to study the oxidation resistance of the coatings and their friction and wear resistance for practical applications.

Grain size dependent tribology mechanism of γ -Ti-48Al-2Cr-2Nb, TiAlN and CrN/NbN can be useful to understand the fundamental mechanism of wear and their evaluation with friction coefficient. In addition, with the variation of nitrogen in TiAlN and CrN/NbN, the oxidation resistance can be useful to study for high temperature wear application.

The cross sectional SEM analysis of the wear track will further strengthen the subsurface deformation and fracture behavior. Further, the TEM analysis of wear track cross section will give the microscopic details of dislocation mobility and defects concentration. Defects and microscopic deformation across the wear track may help to reveal the clear picture of wear mechanism.

Wear track analysis using surface sensitive techniques such as SIMS and XPS may help to understand the role of chemistry and chemical bonding on friction and wear mechanism of γ -Ti-48Al-2Cr-2Nb, TiAlN and CrN/NbN coatings.

Finally, finite element analysis can be useful to model the deformation behavior of sliding surfaces to understand the wear mechanism in macro scale. Moreover, molecular dynamics simulation will be useful to study the atomic and molecular potential of sliding surface and their correlation with friction and wear in micro scale.

REFERENCES

1. Apatiga, L.M., Velazquez, R. and Castano, V.M. "Photochemical effect on diamond film surfaces induced by extended exposure to UV light", Surf. Sci., 529, pp. 158-162, 2003.

2. Arenal, R., Montagnac, G., Bruno, P. and Gruen, D.M. "Multiwavelength Raman spectroscopy of diamond nanowires present in *n*-type ultrananocrystalline films", Phys. Rev. B Vol. 76, pp. 245316-245321, 2008.

3. Askari, S.J., Chen, G.C., Akhtar, F. and Lu, F.X. "Adherent and low friction nano-crystalline diamond film grown on titanium using microwave CVD plasma", Diam. Relat. Mater., Vol. 17, pp. 294-299, 2008.

4. Attaf, M.T. "New ceramics related investigation of the indentation energy concept", Mater. Lett., Vol. 57, pp. 4684-4693, 2003a.

5. Attaf, M.T. "A unified aspect of power–law correlations for berkovich hardness testing of ceramics", Mater. Lett., Vol. 57, pp. 4627-4638, 2003b.

6. Auciello, O. and Sumant, A.V. "Status review of the science and technology of ultrananocrystalline diamond (UNCD™) films and application to multifunctional devices", Diamond Relat. Mater., Vol. 19, pp. 699-718, 2010.

7. Azevedo, A.F., Matsushima, J.T., Vicentin, F.C., Baldan, M.R. and Ferreira, N.G. "Surface characterization of NCD films as a function of sp^2/sp^3 carbon and oxygen content", Appl. Surf. Sci., Vol. 255, pp. 6565-6570, 2009.

8. Balandin, A.A. "Thermal properties of graphene and nanostructured carbon materials", Nature Mater., Vol. 10, pp. 569-81, 2011.

9. Barei, J.C., Hackl, G., Popovska, N., Rosiwal, S.M. and Singer, R.F. "CVD diamond coating of steel on a CVD-TiBN interlayer", Surf. Coat. Technol., Vol. 201, pp. 718-723, 2006.

10. Barshilia, H.C., Deepthi, B., Selvakumar, N., Jain, A. and Rajam, K.S. "Nanolayered multilayer coatings of CrN/CrAlN prepared by reactive DC magnetron sputtering", Appl. Surf. Sci., Vol. 253, pp. 5076-5083, 2007.

11. Barshilia, H.C. and Rajam, K.S. "A Raman-scattering study on the interface structure of nanolayered TiAlN/TiN and TiN/NbN multilayer thin films grown by reactive dc magnetron sputtering", J. Appl. Phys., Vol 98, pp. 14311-1419, 2005

12. Beckers, M., Schell, N., Martins, R.M.S., Mücklich, A., Möller, W. and Hultman, L. "Nucleation and growth of Ti_2AlN thin films deposited by reactive magnetron sputtering onto MgO(111)", J. Appl. Phys., Vol. 102, pp. 74916-74923, 2007.

13. Beegan, D., Chowdhury, S. and Laugier, M.T. "Work of indentation methods for determining copper film hardness", Surf. Coat. Technol., Vol. 192, pp. 57-63, 2005.

14. Bernhard, N., Burkel, E., Gompper, G., Metzger, H., Peisl, J., Wagner, H. and Wallner, G. "Grazing incidence diffraction of x-rays at a Si single crystal surface: Comparison of theory and experiment", J. Phys. B, Vol. 69, pp. 303-311, 1987.

15. Biamino, S., Penna, A., Ackelid, U., Sabbadini, S., Tassa, O., Fino, P., Pavese, M., Gennaro, P. and Badini, C. Electron beam melting of Ti-48Al-2Cr-2Nb alloy: Microstructure and mechanical properties investigation", Intermetallics, Vol. 19, pp. 776-781, 2011.

16. Biigli, U., Blatter, A., Pirnenov, S.M., Obraztsova, E.D., Smolin, A.A., Maillat, M., Leijala, A., Burger, J., Hintermann, H.E. and Loubnin, E.N. "Tribological properties of smooth polycrystalline diamond films", Diamond Relat. Mater., Vol. 4, pp. 1009–1019, 1995.

17. Bhaskaran, H., Gotsmann, B., Sebastian, A., Drechsler, U., Lantz, M.A., Despont, M., Jaroenapibal, P., Carpick, R.W., Chen, Y. and Sridharan, K. "Ultralow nanoscale wear through atom-by-atom attrition in silicon-containing diamond-like carbon", Nat. Nano., Vol. 5, pp. 181-185, 2010.

18. Bhushan B. "Modern tribology handbook", London: CRC Press, 2001.

19. Bhushan, B. and Gupta, B.K. Handbook of Tribology- Materials, coatings and surface treatments, McGraw-Hill, New York, 1991.

20. Blau, P.J. and Lawn B.R. Editors microindentation techniques in materials science and engineering. Philadelphia, PA: American society for testing and materials, 1986.

21. Brady, J.B. and Boardman, S.J. "Introducing mineralogy students to X-ray diffraction through optical diffraction experiments using lasers", J. Geol. Edu., Vol. 43, pp. 471-476, 1995.

22. Bressan, J.D., Hessem R. and Silva, E.M. "Abrasive wear behavior of high speed steel and hard metal coated with TiAlN and TiCN", Wear, Vol. 250, pp. 561-568, 2001.

23. Brooks, I., Lin, P., Palumbo, G., Hibbard, G.D. and Erb, U. "Analysis of hardness–tensile strength relationships for electroformed nanocrystalline materials", Mater. Sci. Eng., A Vol. 491, pp. 412-419, 2008.

24. Bull, S.J. "Energy concept to construct hardness model for bulk materials and graded films ", J. Phys. D: Appl. Phys., Vol. 39, pp. 1626-1634, 2006.

25. Burakowski, T. and Wierzchon, T. "Surface engineering of metals", 1st edition. London, CRC Press, 1999.

26. Burnett, P.J. and Rickerby, D.S. "The mechanical properties of wear-resistant coatings I: Modelling of hardness behavior", Thin Solid Films, Vol. 148, pp. 41-50, 1987.

27. Burton, R. A and Burton, R.G. Proc. 35th Meeting IEEE Holm Conf. on Electrical Contacts, Chicago, IL, New York: IEEE, pp. 31-34, 1989.

28. Cameron, D.C., Aimo, R., Wang, Z.H. and Pischow, K.A. "Structural variations in CrN/NbN superlattices", Surf. Coat. Technol., Vol. 142-144, pp. 567-72, 2001.

29. Carvalho, N.J.M. "Low friction and wear resistant coatings", Groningen: Groningen University Press, 2001.

30. Casiraghi, C., Ferrari, A.C. and Robertson, J. "Raman spectroscopy of hydrogenated amorphous carbons", Phys. Rev. B Vol. 72, pp. 85401-85415, 2005,

31. Chang, Z.K., Wan, X.S., Pei, Z.L., Gong, J. and Sun, C. "Microstructure and mechanical properties of CrN coating deposited by arc ion plating on Ti6Al4V substrate", Surf. Coat. Technol., Vol. 205, pp. 4690-4696, 2011.

32. Chang, Y.Y. and Wang, D.Y. "Corrosion behavior of CrN coatings enhanced by niobium ion implantation", Surf. Coat. Technol., Vol. 188-189, pp. 478-483, 2004a.

33. Chang, Y.Y., Wang, D.Y. and Wei, T.W. "Tribological enhancement of CrN coatings by niobium and carbon ion implantation", Surf. Coat. Technol., Vol. 177-178, pp. 441-446, 2004b.

34. Cheng, J., Yang, J., Zhang, X., Zhong, H., Ma, J. and Li, F. "High temperature tribological behavior of a Ti-46Al-2Cr-2Nb intermetallics", Intermetallics, Vol. 31, pp. 121-126, 2012a.

35. Cheng, J., Yang, J., Ma, J., Bi, Q., Zhang, X. and Fu, L. "The tribological behavior of a Ti-46Al 2Cr-2Nb alloy under liquid paraffine lubrication", Tribol. Lett., Vol. 38, pp. 1-9, 2012b.

36. Chen, X., Peng, Z., Fu, Z., Wu, S., Yue, W. and Wang, C. "Microstructural, mechanical and tribological properties of tungsten-gradually doped diamond-like carbon films with functionally graded interlayers", Surf. Coat. Technol., Vol. 205, pp. 3631-3638, 2011a.

37. Cheng, Y.H., Browne, T. and Heckerman, B. "Mechanical and tribological properties of CrN coatings deposited by large area filtered cathodic arc", Wear, Vol. 271, pp. 775-782, 2011b.

38. Cheng, Y.T. and Cheng, C.M. "Relationship between hardness, elastic modulus, and the work of indentation", Appl. Phys. Lett., Vol. 73, pp. 614-616, 1998.

39. Chom-Cheng, J., Takashiki, G. and Toshio, H. "Non-stoichiometry of titanium nitride plates prepared by chemical vapour deposition", J. Alloys Comp., Vol. 190, pp. 197-200, 1993.

40. Chraponski, J., Szkliniarz, W., Koscielna, K. and Serek, B. Mater. Chem. Phys., "Microstructure and chemical composition of phases in Ti–48Al–2Cr–2Nb intermetallic alloy", Vol. 81, pp. 438- 442, 2003.

41. Cirino, G.A., Mansano, R.D., Verdonck, P., Jasinevicius, R.G. and Neto, L.G. "Diffraction gratings fabricated in DLC thin films", Surf. Coat. Technol., Vol. 204, pp. 2966-2970, 2010.

42. Chu, X., Barnett, S.A., Wong, M.S. and Sproul, W.D. "Reactive unbalanced magnetron sputter deposition of polycrystalline TiN/NbN superlattice coatings", Surf. Coat. Technol., Vol. 57, pp. 13-18, 1993.

43. Crombez, R., McMinis, J., Veerasamy, V.S. and Shen, W. "Experimental study of mechanical properties and scratch resistance of ultra-thin diamond-like-carbon (DLC) coatings deposited on glass", Tribol. Int., Vol. 44, pp. 55-62, 2011.

44. Dao, M., Chollakoop, N., Van Vliet, K.J., Venkatesh, T.A. and Suresh, S. "Computational modeling of the forward and reverse problems in instrumented sharp indentation", Acta Mater., Vol. 49, pp. 3899-3918, 2009.

45. Das, G., Kestler, H., Clemens, H. and Bartolotta, P. "Sheet gamma TiAl: status and opportunities" JOM J. Minerals, Metals and Mater. Soc., Vol. 56, pp. 42-46, 2004.

46. Das, G., Bartolotta, P.A., Kestler, H. and Clemens, H. "Gamma Titanium Aluminides" In: Kim,. Y.W., Clemens, H. and Rosenberger, A.H. editors, 2003.

47. De Barros Bouchet, M.I., Zilibotti, G., Matta, C., Righi, M.C., Vandenbulcke, L., Vacher, B., and Martin, J.M. "Friction of diamond in the presence of water vapor and hydrogen gas. Coupling gas-phase lubrication and first-principles studies", J. Phys. Chem., Vol. 116, pp. 6966-6972, 2012.

48. Deyneka-Dupriez, N., Iqbal, A.P.M., Das, S., Wunderlich, R. and Fecht, H.J. "Frictional shear induced modification of the mechanical properties of TiAl(Nb) intermetallics near the surface", J. Alloys Comp., Vol. 508, pp. 446-452, 2010.

49. Doerner, M.F. and Nix, W.D. "A method for interpreting the data from depth-sensing indentation instruments", J. Mater. Res, Vol 1, pp. 601-609, 1986.

50. Donohue, L.A., Smith, I.J., Munz, W.D., Petrov, I. and Greene, J.E. "Microstructure and oxidation-resistance of $Til_{xyz}Al_xCr_yY_zN$ layers grown by combined steered- arc/unbalanced-magnetron-sputter deposition", Surf. Coat. Technol., Vol. 94-95, pp. 226-231, 1997.

51. Ehiasarian, A.P., Hovsepian, P.Eh., Hultman, L. and Helmersson, U. "Comparison of microstructure and mechanical properties of chromium nitride-based coatings deposited by high power impulse magnetron sputtering and by the combined steered cathodic arc unbalanced magnetron technique", Thin Solid Films, Vol. 457, pp. 270-277, 2004.

52. Erdemir, A. and Donnet C. "Tribology of diamond-like carbon films: recent progress and future prospects", J. Phys. D: Appl. Phys., Vol. 39, pp. 311-327, 2006a.

53. Erdemir, A. and Donnet, C. "Wear: Materials, Mechanisms and Practice edited by Stachowiak, G.W., New York: Wiley, pp. 191-209, 2006b.

54. Erdemir, A., Eryilmaz, O.L., Urgen, M., Kazmanli, K., Mehta, N. and Prorok, B. Nanomaterials Handbook edited by Gogotsi, Y., Boca Raton, FL: CRC Press, 2005.

55. Erdemir, A. "Friction and wear of diamond and diamond-like carbon films", J. Eng. Tribol., Vol. 216, pp. 371-385, 2002.

56. Erdemir, A. and Donnet, C. "Modern Tribology Handbook edited by B Bhushan (Boca Raton, FL: CRC Press), 2000.

57. Erdemir, A., Fenske, G.R., Krauss, A.R., Gruen, D.M., McCauley, T. and Csencsits R.T., "Tribological properties of nanocrystalline diamond films" Surf. Coat. Technol. Vol. 120-121, pp. 565-572, 1999.

58. Erdemir, A., Eryilmaz, O.L. and Fenske, G. "Synthesis of diamondlike carbon films with superlow friction and wear properties", J. Vac. Sci. Technol., Vol. 18, pp. 582459-582464, 1987.

59. Ermolieff, A., Bernard, P., Marthon, S. and Wittmer, P. "Nitridation of polycrystalline titanium as studied by in situ angle-resolved X-ray photoelectron spectroscopy", Surf. Interf. Anal., Vol. 11, pp. 563-568, 1988.

60. Fayette, L., Marcus, B., Mermoux, M., Tourillon, G., Laffon, K., Parent, P. and Normand, F.L. "Local order in CVD diamond films: Comparative Raman, x-ray-diffraction, and x-ray-absorption near-edge studies", Phys. Rev. B Vol. pp. 14123-14132, 1998.

61. Feng, Y. Zhang, T. and Yang, R. "A Work approach to determine Vickers indentation fracture toughness", J. Am. Ceram. Soc., Vol. 94, pp. 332-335, 2011.

62. Ferrari, A.C. and Robertson, J. "Resonant Raman spectroscopy of disordered, amorphous, and diamondlike carbon", Phys. Rev. B., Vol. 64, pp. 75414-75426, 2001.

63. Ferrari, A.C. and Robertson, J. "Interpretation of Raman spectra of disordered and amorphous carbon", Phys. Rev., B Vol. 61, pp. 14095-14107, 2000.

64. Ferrari, A.C., Robertson, J., Pastorelli, R., Beghi, M.G. and Bottani, C.E. "Elastic constants of tetrahedral amorphous carbon films by surface Brillouin scattering", Appl. Phys. Lett., Vol. 75, pp. 1893-1895, 1999.

65. Finkin, E.F. "A theory for the effect of film thickness and normal load in the friction of thin films", J. Lubr. Technol., Vol. 7, pp. 551-556, 1969.

66. Fischer-cripps, A.C. Nanoindentation, Springer, 2004.

67. Fontalvo, G.A., Terziyska, V. and Mitterer, C. "High-temperature tribological behaviour of sputtered NbNx thin films" Surf. Coat. Technol., Vol. 202, pp. 1017-1022, 2007.

68. Fouvry, S., Kapsa, P. and Vincent, L. "Fretting behaviour of hard coatings under high normal load", Surf. Coat. Technol., Vol. 68-69, pp. 494-499, 1994.

69. Fusaro, R.L. and Sliney, H.E. "Graphite fluoride $(CF_x)_n$- A new solid lubricant" ASLE Trans., Vol. 13, pp. 56-65, 1970.

70. Gao, X.L. "An expanding cavity model incorporating strain-hardening and indentation size effects", Int. J. Solids Struct., Vol. 43, pp. 6615-6629, 2006.

71. Gayathri, S., Kumar, N., Krishnan, R., Ravindran, T.R., Dash, S., Tyagi, A.K., Raj, B. and Sridharan, M. "Tribological properties of pulsed laser deposited DLC/TM (TM= Cr, Ag, Ti and Ni) multilayers", Tribol. Int., Vol. 53, pp. 87-97, 2012.

72.   Geng, C.L., Tang, W.Z., Hei, L.E., Liu, S.T. and Lu, F.X. "Fracture strength of two-step pretreated and diamond coated cemented carbide microdrills", Int. J. Refract. Met. Hard Mater., Vol. 25, pp. 159-165, 2007.

73.   Giacovazzo, C. Fundamentals of crystallography, Oxford: Oxford University Press, 1992.

74.   Giannakopolus, A.E. and Suresh, S. "Determination of elasto plastic properties by instrumented sharp indentation", Scr. Mater., Vol. 40, pp. 1191-1198, 1999.

75.   Godet, M. "The third body approach: A mechanicsl view of wear", Wear, Vol. 100, pp. 437-452, 1984.

76.   Goldstein, J., Newbury, D., Joy, D.C., Lyman, C.E., Echlin, P., Lifshin, E., Sawyer, L. and Michael, J.R. "Scanning electron microscopy and X-ray microanalysis", Springer; 3rd edition, 2003.

77.   Golovin, A.L., Imamov, R.M. and Stepanov, S.A. "Experimental study of x-ray diffraction under specular reflection conditions", Acta Cryst. A, Vol. 40, pp. 225-234, 1984.

78.   Grill, A. "Tribology of diamondlike carbon and related materials: an updated review", Surf. Coat. Technol., Vol. 94, pp. 507-513, 1997.

79.   Grzesik, W., Zalisz, Z. and Król, S. "Tribological behaviour of TiAlN coated carbides in dry sliding tests", J. Achiev. Mater. Manuf. Eng., Vol. 17, pp. 181-184, 2006a.

80.   Grzesik, W., Zalisz, Z., Krol, S. and Nieslony, P. "Investigations on friction and wear mechanisms of the PVD-TiAlN coated carbide in dry sliding against steels and cast iron", Wear, Vol. 261, pp. 1191-1200, 2006b.

81.   Gutiérrez, A., López, M.F., García, I. and Vázquez, A. "X-ray absorption and Auger electron spectroscopy studies of the quality of diamond thin films grown by the oxy-acetylene flame method", J. Vac. Sci. Technol., A Vol. 15, pp. 294-297, 1997.

82.   Guu, Y.Y., Lin, J.F. and Ai, C.F. "The tribological characteristics of titanium nitride coatings. Part I coating thickness effects", Wear, Vol. 194, pp. 12-21, 1996.

83. Gwang, S.K., Sang, Y.L., Jun, H.H. and Sang, Y.L. "Synthesis of CrN/AlN superlattice coatings using closed-field unbalanced magnetron sputtering process", Surf. Coat. Technol., Vol. 171, pp. 91-95, 2003.

84. Helmersson, U., Todorova, S., Barnett, S.A., Sundgren, J.E., Mrkert, L.C. and Greene, J.E. "Growth of single-crystal TiN/VN strained-layer superlattices with extremely high mechanical hardness", J. Appl. Phys., Vol. 62, pp. 481-484, 1987.

85. Holmberg, K., Ronkainen, H., Laukkanen, A. and Wallin, K. "Friction and wear of coated surfaces- scales, modelling and simulation of tribomechanisms", Surf. Coat. Technol., Vol. 202, pp. 1034-1049, 2007.

86. Holmberg, K., Matthews, A., and Ronkainen, H. Coatings tribology-contact mechanisms and surface design", Tribol. Int., Vol. 31, pp. 107-120, 1998.

87. Holmberg, K. and Matthews, A. "Coatings tribology: properties, techniques and applications in surface engineering", Tribology series, Vol. 28. New York: Elsevier, 1994.

88. Holmberg, K. "A concept for friction mechanisms of coated surfaces", Surf. Coat. Technol., Vol. 56, pp. 1-10, 1992.

89. Hones, P., Sanjines, R. and Levy, F. "Characterization of sputter-deposited chromium nitride thin films for hard coatings", Surf. Coat. Technol., Vol. 91-95, pp. 398-402, 1997.

90. Hovsepian, P.Eh., Lewis, D.B., Luo, Q. and Farinotti, A. "Corrosion resistance of CrN/NbN superlattice coatings grown by various physical vapour deposition techniques", Thin Solid Films, Vol. 488, pp. 1-8, 2005.

91. Ikeda, R., Tanei, H., Nakamura, N., Ogi, H., Hirao, M., Sawabe, A. and Takemoto, M. "Elastic constant of nanocrystalline diamond film" Diamond Relat. Mater., Vol. 15, pp. 729-734, 2006.

92. Imayev, V.M., Imayev, R.M., Salischev, G.A., Povarova, K.B., Shagiev, M.R. and Kunznetsov, A.V. Scripta Mater., Vol. 36, pp. 891-897, 1997.

93. Irudayaraj, A.A., Kuppusami, P., Thirumurugesan, R., Mohandas, E., Kalainathan, S. and Raghunathan, VS. "Influence of nitrogen flow rate on growth of TiAlN films prepared by DC magnetron sputtering", Surf. Eng., Vol. 23, 7-11, 2007.

94. Janos, V. "The Shirley-equivalent electron inelastic scattering cross-section function", Surf. Sci. Vol. 563, pp. 183-190, 2004.

95. Joseph, P.T., Tai, N.H., Lee, C.Y., Niu, H., Pong, W.F. and Lin, I.N. "Field emission enhancement in nitrogen-ion-implanted ultrananocrystalline diamond films", J. Appl. Phys., Vol. 103, pp. 43720-43726, 2008.

96. Kato, K., Umehara, N. and Adachi, K. Frequency characteristics of stiffness and damping effect of ferro fluid bearing", Wear, Vol. 254, pp. 1056-1060, 2003.

97. Kato, K. and Adashi, K. in: Bhushan, B. (Ed.), Modern Tribology Handbook, CRC Press, New York, 2001.

98. Kempf, M., Goken, M. and Vehoff, H. "The mechanical properties of different lamellae and domains in PST-TiAl investigated with nanoindentations and atomic force microscopy", Mater. Sci. Eng. A, Vol. 329, pp. 184-189, 2002.

99. Kessler, O.H., Hoffmann, F.T. and Mayr, P. "Combinations of coating and heat treating processes: establishing a system for combined processes and examples", Surf. Coat. Technol., Vol. 108-109, pp. 211-216, 1998.

100. Keunecke, M., Stein, C., Bewilogua, K., Koelker, W., Kassel, D. and van den Berg, H. "Modified TiAlN coatings prepared by d.c. pulsed magnetron sputtering", Surf. Coat. Technol., Vol. 205, pp. 1273-1278, 2010.

101. Khan, M.K., Hainsworth, M.E., Fitzpatrick and Edwards, L. "Application of the work indentation approach for the characterization of aluminium 2024- T351 and Al cladding by nanoindentation", J. Mater. Sci., Vol. 44, pp. 1006-1015, 2009.

102. Konicek, A.R., Grierson, D.S., Sumant, A.V., Friedmann, T.A., Sullivan, J.P., Gilbert, P.U.P.A., Sawyer, W.G. and Carpick, R.W. "Influence of surface passivation on the friction and wear behavior of ultrananocrystalline diamond and tetrahedral amorphous carbon thin films", Phys. Rev. B, Vol. 85, pp. 155448-15560, 2012.

103. Konicek, A.R., Grierson, D.S., Gilbert, P.U.P.A., Sawyer, W.G., Sumant, A.V. and Carpick, R.W. "Origin of ultralow friction and wear in ultra nano- crystalline diamond", Phys. Rev. Lett., Vol. 100, pp. 235502–235506, 2008.

104. Krauss, A.R., Auciello, O., Gruen, D.M., Jayatissa, A., Sumant, A., Tucek, J., Mancini, D.C., Moldovan, N., Erdemir, A., Ersoy, D.M., Gardos, N., Busmann, H.G., Meyer, E.M. and Ding, M.Q. "Ultrananocrystalline diamond thin films for MEMS moving mechanical assembly devices", Diamond Relat. Mater., Vol. 10, pp. 1952-1961, 2001.

105. Kumar, N., Das, C.R., Dash, S., Albert, S.K., Chandramohan, P., Bhaduri, A.K., Tyagi, A.K. and Raj, B. "Tribo-induced phase transformation and associated evolution of friction of NiCrB alloy", Tribol. Trans., Vol. 55, pp. 117-121, 2012a.

106. Kumar, N., Panda, K., Dash, S., Popov, C., Reithmaier, J.P., Panigrahi, B.K., Tyagi, A.K. and Raj, B. "Tribological properties of nanocrystalline diamond films deposited by hot filament chemical vapor deposition", AIP ADVANCES, Vol. 2, pp. 32164-3277, 2012b.

107. La, P., Xue, Q. and Liu, W. "Tribological properties of $Ni_3Al-Cr_7C_3$ composite coating under water lubrication', Tribol. Int., Vol. 33, pp. 469-475, 2000.

108. Larsson, M., Hollman, P., Hedenqvist, P., Hogmark, S., Wahlstrom, U. and Hultman, L. "Deposition and microstructure of PVD TiN-NbN multilayered coatings by combined reactive electron beam evaporation and DC sputtering", Surf. Coat. Technol.,Vol. 86-87, pp. 351-56, 1996.

109. Lawn, B.R. and Wilshaw, T.R. "Indentation techniques for measuring fracture toughness: I direct crack measurements", J. Am. Ceram. Soc., Vol. 64, pp. 533-538, 1981.

110. Lee, J.W., Tien, S.K., Kuo, Y.C. and Chen, C.M. "The mechanical properties evaluation of the CrN coatings deposited by the pulsed DC reactive magnetron sputtering", Surf. Coat. Technol., Vol. 200, pp. 3330-3335, 2006.

111. Lewis, D.B., Reitz, D., Wustefeld, C., Ohser-Wiedemann, R., Oettel, H. and Ehiasarian, A.P. "Chromium nitride/niobium nitride nano-scale multilayer coatings deposited at low temperature by the combined cathodic arc/unbalanced magnetron technique", Thin Solid Films, Vol. 503, pp. 133-142, 2006.

112. Li, J.J., Zheng, W.T., Wu, H.H., Sun, L., Gu, G.G., Bian, H.J., Lu, X.Y. and Jin, Z.S. "Compositional and structural modifications of amorphous carbon nitride films induced by thermal annealing", J. Phys. D: Appl. Phys., Vol. 36, pp. 2001-2005, 2011.

113. Li, X.J., Cheng, G.A., Xue, W.B., Zheng, R.T. and Cheng, Y.J. "Wear and corrosion resistant coatings formed by microarc oxidation on TiAl alloy", Mater. Chem. Phys., Vol. 107, pp. 148-152, 2008.

114. Li, C., Xia, J. and Dong, H. "Sliding wear of TiAl intermetallics against steel and ceramics of Al_2O_3, Si_3N_4 and WC/Co", Wear, Vol. 261, pp. 693-701, 2006.

115. Liu, H., Guo, H., Li, P. and Wei, Y. "The transformation of ferrihydrite in the presence of trace Fe(II): The effect of the anionic media", J. Solid State Chem., Vol. 181, pp. 2666-2671, 2008.

116. Liu, X.B. and Wang, H.M. "Modification of tribology and high-temperature behavior of Ti-48Al 2Cr-2Nb intermetallic alloy by laser cladding", Appl. Surf. Sci., Vol. 252, pp. 5735-5744, 2006.

117. Ma, K.L, Zhang, W.J., Zou, Y.S., Chong, Y.M., Leung, K.M., Bello, I. and Lee, S.T. "Electrical properties of nitrogen incorporated nanocrystalline diamond films", Diamond Relat. Mater., Vol. 15, pp. 626-663, 2006.

118. Mahato, A., Verma, N., Jayaram, V. and Biswas, S.K. "Severe wear of a near eutectic aluminium-silicon alloy", Acta Mater., Vol. 59, pp. 6069-6082, 2011.

119. Manohara, H.R., Chandrashekharaiah, T.M., Venkateswarlu, K. and Kori, S.A. "Dry sliding wear response of A413 alloy: Influence of intermetallics and test parameters", Tribol. Int., Vol. 51, pp. 54-60, 2012.

120. Manika, I. and Maniks, J. "Effect of substrate hardness and film structure on indentation depth criteria for film hardness testing", J. Phys. D: Appl. Phys., Vol. 41, pp. 74010-74015, 2008.

121. Martini, C. and Ceschini, L. "A comparative study of the tribological behaviour of PVD coatings on the Ti-6Al-4V alloy", Tribol. Int., Vol. 44, pp. 297-308, 2011.

122. Matossian, J., Wei, R., Vajo, J., Hunt, G., Gardos, M., Chambers, G., Soucy, L., Oliver, D., Jay, L., Taylor, C.M., Alderson, G., Komanduri, R. and Perry, A. "Plasma-enhanced, magnetron-sputtered deposition (PMD) of materials", Surf. Coat. Technol., Vol. 96, pp. 58-67, 1997.

123. Mattox, D.M. "The foundation of vacuum coating technology", New York: Noyes/ William Andrews Publishing, 2003.

124. Mittemeijer, E.J. and Scardi, P. Diffraction analysis of the microstructure of materials, Springer, 2004.

125. Mitterer, C., Hultman, L., Mayrhofer, P.H. and Clemens, H. "Microstructural design of hard coatings", Prog. Mater. Sci., Vol. 51, pp. 1032-1114, 2006.

126. Mercer, C. and Soboyejo, W.O. "Effects of alloying on crack- tip deformation and sheiding in gamma-based titanium aluminides", Acta Mater., Vol. 45, pp. 961-971, 1997.

127. Misra, A., Bist, H.D., Navati, M.S., Thareja, R.K. and Narayan, J. "Thin film of aluminum oxide through pulsed laser deposition: a micro-Raman study", Mater., Sci. Eng. B Vol. 79, pp. 49-54, 2001.

128. Miyoshi, K., Lerch, B. and Draper, S. "Fretting wear of Ti-48Al-2Cr-2Nb", Tribol. Int., Vol. 36, pp. 145-153, 2003.

129. Mo, J.L. and Zhu, M.H. "Sliding tribological behavior of AlCrN coating", Tribol. Int., Vol. 41, pp. 1161-1168, 2008.

130. Moseler, M., Gumbsch, P., Casiraghi, C., Ferrari, A. and Robertson, J. "The Ultra smoothness of Diamond-like Carbon Surfaces", Science, Vol. 309, pp. 1545-1548, 2005.

131. Moser, M., Mayrhofer, P.H. and Clemens, H. "On the influence of coating and oxidation on the mechanical properties of a g-TiAl based alloy", Intermetallics, Vol. 16, pp. 1206-1211, 2008.

132. Niu, M., Bi, Q., Yang, J. and Liu, W. "Tribological performances of Ni3Si–Cr7C3 composite coatings under water and acid environments", Tribol. Int., Vol. 48, pp. 216-225, 2012.

133. Nordin, M., Herranen, M. and Hogmark, S. "Influence of lamellae thickness on the corrosion behaviour of multilayered PVD TiN/CrN coatings", Thin Solid Films, Vol. 348, pp. 202-209, 1999.

134. Oliveira, S.A.G. and Bower, A.F. "An analysis of fracture and delamination in thin coatings subject to contact loading", Wear, Vol. 198, pp. 15-32, 1996.

135. Oilver, W.C. and Pharr, G.M. "Measurement of hardness and elastic properties by instrumented indentation: advances in understanding and refinements to methodology", J. Mater. Res., Vol. 19, pp. 30-10, 2004.

136. Oliver, W.C. and Pharr, G.M. "An improved technique for determining hardness and elastic modulus using load and displacement sensing indentation experiments", J. Mater. Res., Vol. 7, pp. 1564-1583, 1992.

137. Ostrovskaya, L., Perevertailo, V., Ralchenko, V., Saveliev, A. and Zhuravlev, V. "Wettability of nanocrystalline diamond films", Diamond Relat. Mater., Vol. 16, pp. 2109-2113, 2007.

138. Ostrovskaya, L.Y., Dementiev, A.P., Kulakova, I.I. and Ralchenko, V.G. "Chemical state and wettability of ion-irradiated diamond surfaces", Diamond Relat. Mater., Vol. 14, pp. 486-490, 2005.

139. Otto, K.,Weber, W.H., Graham, G.M. and Shyu, J.Z. "Identification of dispersed platinum on γ alumina by laser Raman spectroscopy", Appl. Sur. Sci., Vol. 37, pp. 250-257, 1889.

140. Ozun, O., Guclu, N., Kolemen, U. and Sahin, O. "Analysis of data on indentation load against penetration depth for bulk MgB_2 crystal using indentation work and Oliver-Pharr approaches", Mater. Chem. Phys., Vol. 112, pp. 5-10, 2008.

141. Paik, N. "Raman and XPS studies of DLC films prepared by a magnetron sputter-type negative ion source", Surf. Coat. Technol., Vol. 200, pp. 2170-2174, 2005.

142. Panda, K., Kumar, N., Sankaran, K.J., Panigrahi, B.K., Dash, S., Chen, H.C., Lin, I.N., Tai, N.H. and Tyagi, A.K. "Tribological properties of Nb ion implanted ultrananocrystalline diamond films", Surf. Coat. Technol., Vol. 207, pp. 124-136, 2012.

143. Pandey, B., Pal, P.P., Bera, S., Ray, S.K. and Kara, A.K. "Effect of nickel incorporation on microstructural and optical properties of electrodeposited diamond like carbon (DLC) thin films", Appl. Surf. Sci., Vol. 261, pp. 789-99, 2012.

144. Pharr, G.M. "Measurement of mechanical properties by ultra-low load indentation", Mater. Sci. Eng. A Vol. 253, pp. 151-159, 1998.

145. Phillips, J.C. "Structural significance of Raman spectra of OH- and F-doped vitreous silica" Phys. Rev. B, Vol. 33, pp. 4443-4445, 1986.

146. Polcar, T., Parreira, N.M.G. and Novák, R. "Friction and wear behaviour of CrN coating at temperatures up to 500 °C", Surf. Coat. Technol., Vol. 201, pp. 5228-5235, 2007.

147. Popov, C., Kulisch, W., Jelinek, M. and Bock, A. and Strnad, J. "Nanocrystalline diamond/amorphous carbon composite films for applications in tribology, optics and biomedicine', Thin Solid Films, Vol. 494, pp. 92-97, 2006

148. Qi, L., Stanishevsky, A. and Vohra, Y.K. "Tribological properties of undoped and boron-doped nanocrystalline diamond films", Thin Solid Films, Vol. 517, pp. 800-804, 2008.

149. Quesada, F., Marino, A. and Restrepo, E. "TiAlN coatings deposited by R.F. magnetron sputtering on previously treated ASTM A36 steel", Surf. Coat. Technol., Vol. 201, pp. 2925-2929, 2006.

150. Quinn, T.F.J. "The oxidational wear of low alloy steels", Tribol. Int., Vol. 35, pp. 691-615, 2002.

151. Quinn, T.F.J. and Winer, W.O. "The thermal aspects of oxidational wear", Wear, Vol. 102, pp. 67-80, 1985.

152. Quinn, T.F.J. "Oxidational wear", Wear, Vol. 18, pp. 413-419, 1971.

153. Rabinowicz, E and Imai, M. "Friction properties of pyrolitic boron nitride and graphite", Wear, Vol. 7, pp. 298-300, 1964.

154. Rastkar, A., Shokri, B. "A multi-step process of oxygen diffusion to improve the wear performance of a gamma-based titanium aluminide", Wear, Vol. 264, pp. 973-981, 2008.

155. Rastkar, A. and Bell, T. "Characterization and tribological performance of oxide layers on a gamma based titanium aluminide", Wear, Vol. 258, pp. 1616-1624, 2005.

156. Rastkar, A., Bloyce, A. and Bell, T. "Sliding wear behaviour of two gamma-based titanium aluminides", Wear, Vol. 240, pp. 19-26, 2000.

157. Robertson, J. "Diamond-like amorphous carbon", Mater. Sci. Eng. R: Reports, Vol. 37, pp. 129-81, 2002.

158. Sakai, M. "Energy principle of the indentation-induced inelastic surface deformation and hardness of brittle materials", Acta Metall. Mater., Vol. 41, pp. 1751-1758, 1993.

159. Sankaran, K.J., Kumar, N., Chen, H.C., Dong, C.L., Bahuguna, A., Dash, S., Tyagi, A.K., Lee, C.Y., Tai, N.H. and Lin, I.N. "Near frictionless behavior of hydrogen plasma treated diamond nanowire films", Sci. Adv. Mater., Vol. 5, pp. 1-12, 2013.

160. Saunders, S.R.J., Monteiro, M. and Rizzo, F. "The oxidation behaviour of metals and alloys at high temperatures in atmospheres containing water vapour: A review", Prog. Mater. Sci., Vol. 53, pp. 775-837, 2008.

161. Savage, R.H. Graphite lubrication", J. Appl. Phys., Vol. 19, pp. 1-10, 1948.

162. Seetharaman, V. and Semiatin, S.L. "Microstuctures and tensile properties of Ti-45.5Al-2Nb-2-Cr rolled sheets", Mater. Sci. Eng. A, Vol. 299, pp. 195-209, 2001.

163. Seog-Young, Y., Jong-Kuk, K. and Kwang, Ho K. "A comparative study on tribological behavior of TiN and TiAlN coatings prepared by arc ion plating technique", Surf. Coat. Technol., Vol. 161, pp. 237-242, 2002.

164. Schuster, J. and Bauer, J. "The ternary system titanium-aluminum-nitrogen", J. Solid Sate Chem., Vol. 53, pp. 260-265, 1984.

165. Sharda, T., Misra, D.S., Seibt, E.W. and Selvam, P. "High resolution Auger electron spectroscopy studies on (100) and (111) facets of chemical vapor deposited diamond", J. Vac. Sci. Technol. A, Vol. 16, pp. 413-418, 1998.

166. Sharma, N., Kumar, N., Dhara, S., Dash, S., Bahuguna, A., Kamruddin, M., Tyagi, A.K. and Raj, B. "Tribological properties of ultra nanocrystalline diamond film-effect of sliding counterbodies", Tribol. Int., Vol. 53, pp. 167-178, 2012.

167. Singer, I.L. "A thermomechanical model for analyzing low wear rate materials", Surf. Coat. Technol., Vol. 49, pp. 474-481, 1991.

168. Sneddon, I.N. "The relation between load and penetration in the axisymmetric Boussinesq problem for a punch of arbitrary profile", Int. J. Eng. Sci. Vol. 3, pp. 47-56, 1965.

169. Soboyejo, W.O. and Mercer, C. "On the implications of deformation-induced crack-tip deformation in gamma-based titanium aluminide intermetallic", J. Scripta Metall. Mater., Vol. 30, pp. 1515-1520, 1994.

170. Sopunna, K., Thongtem, T., McNallan, M. and Thongtem, S. "Formation of titanium nitride on γ TiAl alloys by direct metal-gas reaction", J. Mater. Sci., Vol. 41, pp. 4654-4662, 2006.

171. Spengler, W., Kaiser, R., Christensen, A.N. and Miiller-Vogt, G. "Raman scattering, superconductivity and phonon density of states of stoichiometric and nonstoichiometric TiN", Phys. Rev. B, Vol. 17, pp. 1095-1101, 1978.

172. Stillwell, N.A. and Tabor, D. "Elastic recovery of conical indentation", Proc. Phys. Soc. Lond., Vol. 78, pp. 169-179, 1961.

173. Sumant, A.V., Auciello, O., Carpick, R.W., Srinivasan, S. and Butler, J.E. "Ultrananocrystalline and nanocrystalline diamond thin films for MEMS/NEMS applications", MRS Bulletin, Vol. 35, pp. 281-288, 2010.

174. Sumant, A.V., Grierson, D.S., Gerbi, J.E., Carlisle, J.A., Auciello, O. and Carpick, R.W. "Surface chemistry and bonding configuration of ultrananocrystalline diamond surfaces and their effects on nanotribological properties", Phys. Rev. B, Vol. 76, pp. 235429-235439, 2007.

175. Sumant, A.V., Grierson, D.S., Gerbi, J.E., Birrell, J., Lanke, U.D. and Caprik, R.W. "Towards the ultimate tribological interface: Surface chemistry and nanotribology of ultrananocrystalline diamond", Adv. Mater., Vol. 17, pp.1039-1045, 2005.

176. Suresha, S.J., Bhide, R., Jayaram, V. and Biswas, S.K. "Processing, microstructure and hardness of TiN/(Ti, Al)N multilayer coatings", Mater. Sci. Eng., A Vol. 429, pp. pp.252-260, 2006.

177. Tabor, D. The hardness of metals, Oxford: Oxford University Press, 1951.

178. Tang, C.J., Abe, I., Vieira, L.G., Soares, M.J., Grácio, J. and Pinto, L.J. "Investigation of nitrogen addition on hydrogen incorporation in CVD diamond films from polycrystalline to nanocrystalline", Diamond Relat. Mater., Vol. 19, pp. 404-408, 2010.

179. Tetsui, T. and Ono, S. "Endurance and composition and microstructure effects on endurance of TiAl used in turbochargers", Intermetallics, Vol. 7, pp. 689-697, 1999.

180. Tillmann, W., Vogli, E. and Momeni, S. "Mechanical and tribological properties of Ti/TiAlN duplex coatings on high and low alloy tool steels", Vacuum, Vol. 84, pp. 387-392, 2010.

181. Tomlinson, M., Lyon, S.B., Hovsepian, P. and Munz, W.D. "Corrosion performance of CrN/NbN superlattice coatings deposited by the combined cathodic arc/unbalanced magnetron technique", Vacuum, Vol. 53, pp. 117-121, 1999.

182. Torres, R.D., Soares, P.C., Schmitz, C. and Siqueira, C.J.M. "Influence of the nitriding and TiAlN/TiN coating thickness on the sliding wear behavior of duplex treated AISI H13 steel", Surf. Coat. Technol., Vol. 205, pp. 1381-1385, 2010.

183. Tsai, H-C. and Bogy, D.B. "Characterization of diamondlike carbon films and their application as overcoats on thinfilm media for magnetic recording", J. Vac. Sci. Technol., A Vol. 5, pp. 3287-3313, 1987.

184. Tuck, J.R., Korsunsky, A.M., Bull, S.J. and Davidson R.I. "On the application of the work-of-indentation approach to depth-sensing indentation experiments in coated systems", Surf. Coat. Technol., Vol. 137, pp. 217-224, 2001.

185. Varlese, F.A., Tului, M., Sabbadini, S., Pellissero, F., Sebastiani, M. and Bemporad, E. "Optimized coating procedure for the protection of TiAl intermetallic alloy against high temperature oxidation", Intermetallics, Vol. 37, pp. 76-82, 2013.

186. Vashishta, P., Kalia, R.K., Nakano, A. and Rino, J.P. "Collaboratory for Advanced Computing and Simulations, Interaction potential for aluminum nitride: A molecular dynamics study of mechanical and thermal properties of crystalline and amorphous aluminum nitride", J. Appl. Phys., Vol. 109, pp. 33514-33521, 2011.

187. Venkatesh, T.A., Van Vliet, K.J., Giannakopoulos, A.E. and Suresh, S. "Determination of elasto- plastic properties by instrumented sharp indentation: guidelines for property extraction", Scr. Mater., 42, pp. 833-839, 2000.

188. Vlasov, I.I., Lebedev, O.I., Ralchenko, V.G., Goovaerts, E., Bertoni, G., Van Tendeloo, G., and Kono, V.I. "Hybrid diamond-graphite nanowires produced by microwave plasma chemical vapor deposition", Adv. Mater., Vol. 19 pp. 4058-4062, 2007.

189. Voevodin, A.A. and Zabinsk, J.S. "Superhard, functionally gradient, nanolayered and nanocomposite diamond-like carbon coatings for wear protection", Diamond Relat. Mater., Vol. 7, pp. 463–467, 1998.

190. Vyas, A., Shen, Y.G., Zhou, Z.F. and Li, K.Y. "Nano-structured CrN/CNx multilayer films deposited by magnetron sputtering", Comp. Sci. Technol., Vol. 68, pp. 2922-2929, 2008.

191. Wang, Y., Qian, Z., Li, X.Y. and Tandon, K.N. "Sliding wear properties of TiAl alloys with/without TiN coatings", Surf Coat Technol., Vol. 91, pp. 37-42, 1997.

192. Wang, Q., Zhou, F., Chen, K., Wang, M. and Qian, T. "Friction and wear properties of TiCN coatings sliding against SiC and steel balls in air and water", Thin Solid Films, Vol. 519, pp. 4830-4841, 2011.

193. Wei, F.I. and Stott, F.H. "The Development of Cr_2O_3 scales on iron-chromium alloys containing reactive elements", Corr. Sci., Vol. 29, pp. 839-861, 1989.

194. Wooster, W.A. "Physical properties and atomic arrangements in crystals", Rep. Prog. Phys., 16, pp. 62-82, 1953.

195. Wright, A.F. and Nelson, J.S. "First-principles calculations for zinc-blende AlInN alloys", Appl. Phys. Lett., Vol. 66, pp. 3465-3467, 1995.

196. Xiang, Z., Fenghui, W., Jianye, H. and Tiejun, L. "Determining the mechanical properties of solid oxide fuel cell by an improved work of indentation approach", J. Power Sour., Vol. 29, pp. 231-235, 2011.

197. Xinhua, Wu., Huang, A., Hu, D. and Loretto, M.H. "Oxidation-induced embrittlement of TiAl alloys", Intermetallics, Vol. 17, pp. 540-552, 2009.

198. Yue, Z.R., Jiang, W., Wang, L., Gardner, S.D. and Pittman, Jr. C.U. "Surface characterization of electrochemically oxidized carbon fibers", Carbon, Vol. 37, pp. 1785-1796, 1999.

199. Yamaguchi, M., Inui, H. and Ito, K. "High temperature structural intermetallics" Acta Mater., Vol. 48, pp. 307-322, 1999.

200. Zhang, X., Ma, J., Yang, J., Bi, Q. and Liu, W. "Dry-sliding tribological behavior of Fe-28Al-5Cr/TiC composites", Wear, Vol. 271, pp. 881-888, 2011.

201. Zhang, G., Yan, P., Wang, P., Chen, Y., Zhang, J., Wang, L. and Zhang, J. "The effect of applied substrate negative bias voltage on the structure and properties of Al-containing a-C:H thin films", Surf. Coat. Technol., Vol. 202, pp. 2684-2689, 2008.

202. Zhang, P., Wang, L. and Nie, X. "Tribological properties of a-C/Cr(N) coatings in micro-and nano-scales", Surf. Coat. Technol., Vol. 201, pp. 5176-5181, 2007.

203. Zhang, Y., Yang-Tse, C. and Grummon, D.S. "The influence of superelastic NiTi interlayers on tribological properties of CrN hard coatings", Mater. Sci. Eng., A Vol. 438-440, pp.710-713, 2006.

204. Zhou, Z., Rainforth, W.M., Luo, Q., Hovsepian, P.Eh., Ojeda, J.J. and Romero-Gonzalez, M.E. "Wear and friction of TiAlN/VN coatings against Al_2O_3 in air at room and elevated temperatures", Acta Mater., Vol. 58, pp. 2912-2925, 2010.

205. Zhou, L. and Yao, Y. "Single crystal bulk material micro/nano indentation hardness testing by nanoindentation instrument and AFM", Mater. Lett. Eng. A, Vol. 460-461, pp. 95-100, 2007.

206. Zhou, Z., Rainforth, W.M.,, Lewisb, D.B., Creasy, S., Forsyth, J.J., Clegg, F., Ehiasarian, A.P., Hovespian, P.E. and Munz, W.D. "Oxidation behavior of nanoscale TiAlN/VN multilayer coatings", Surf. Coat. Technol., Vol. 177, pp. 198-203, 2004.

207. Zilibotti, G., Righi, M.C. and Ferrario, M. "Ab initio study on the surface chemistry and nanotribological properties of passivated diamond surfaces", Phys. Rev. B Vol. 79, pp. 75420-75430, 2009.

LIST OF PUBLICATIONS

1. **Radhika, R.,** Kumar, N., Pandian, R., Dash, S., Ravindran, T.R., Arivuoli, D. and Tyagi A.K. "Tribological properties and deformation mechanism of TiAlN coating sliding with various counterbodies", Tribology International, Vol. 66, pp.143-148, 2013.

2. Sankaran, K.J., Kumar, N., Kurian, J., **Radhika, R.,** Chen, H.C., Dash, S. Tyagi, A.K., Lee, C.Y., Tai, N.H. and Lin, I.N. "Improvement in tribological properties by modification of grain boundary and microstructure of ultrananocrystalline diamond films", ACS Applied Materials & Interfaces, Vol. 5, pp. 3614-3624, 2013.

3. Kumar, N., **Radhika, R.,** Kozakov, A.T., Sankaran, K.J., Dash, S., Tyagi, A.K., Tai, N.H. and Lin, I.N. "Humidity dependent friction mechanism in ultrananocrystalline diamond film", Journal of Physics D: Applied Physics, Vol. 46, pp. 275501-275509, 2013.

4. **Radhika, R.,** Kumar, N., Dash, S., Arivuoli, D. and Tyagi A.K. "Wear mechanism of CrN/NbN superlattice coating sliding against various counterbodies", International Journal of Refractory Metals and Hard Materials, Vol. 41, pp. 547-552, 2013.

5. **Radhika**, R., Kumar, N., Sankaran, K.J., Dumpala, R., Dash, S., Rao, M.S.R., Arivuoli, D., Tyagi, A.K., Tai, N.H. and Lin, I.N. "Extremely high wear resistance and ultra-low friction behavior of oxygen plasma treated nanocrystalline diamond nanowire films", Journal of Physics D: Applied Physics, Vol. 46, pp. 425304-425313, 2013.

6. **Radhika, R.** and Arivuoli, D. "Studies on mechanical properties of titanium aluminium nitride coatings", Indian Journal of Physics, Vol. 87, pp. 1199-1206, 2013.

Paper accepted in the International/ National conferences

1. **Radhika, R**., Geetha, D., and Arivuoli, D. "Nanomechanical studies of epitaxial GaN/InGaN hetero-structures", 7th International conference on advanced materials ROCAM, p. 156, 28th – 31st August, Brasov, Romania, 2012.

2. **Radhika, R**. and Arivuoli, D. "Nanoindentation analysis of DLC/Si hard coatings", 7th International conference on advanced materials ROCAM, p. 159, 28th – 31st August, Brasov, Romania, 2012.

3. **Radhika, R.**, Kumar, N., Dash, S., Arivuoli, D. and Tyagi A.K**.** "Surface chemistry and friction behavior of ultra- nanocrystalline diamond film", Confernce on friction and energy dissipation in man- made and biological systems, November 4th –8th, Trieste, Italy, 2013.

CURRICULUM VITAE

R. RADHIKA was born on 15th April 1979 in the town Egmore, Chennai, India. She had her schooling at Christ King Girls Higher Secondary School, Tambaram. She received her Bachelor degree in Physics from Madras University through S.D.N.B. Vaishnav College for Women, Chennai and Masters Degree in Materials Science from Anna University, Chennai respectively. She had her Master of Philosophy in Physics from Madras University, through Madras Christian College, Chennai. She worked as a lecturer in Department of Physics, Hindustan college of Engineering from 2003-2005.

She joined Ph.D at Anna University, Chennai in January 2006. She had carried out extensive studies on tribological properties and wear mechanism of hard coatings. She had working experience in various indentation techniques and tribology measurements. National Doctoral Fellow by the All India Council for Technical Education was awarded to her from 2006-2010. She was awarded the prestigious European Union fellowship "Erasmus Mundus" at DISAT, Politecnico di Torino, Italy during June 2010 to June 2012.

She has published five papers in International journals and one in National journal. She has presented three papers in International conferences.